SUBMITTED TO THE ASTROPHYSICAL JOURNAL.
Preprint typeset using LaTeX style emulateapj v. 5/2/11

arXiv:1406.2526v3 [astro-ph.GA] 11 Sep 2014

FARADAY ROTATION FROM MAGNESIUM II ABSORBERS TOWARDS POLARIZED BACKGROUND RADIO SOURCES

J. S. FARNES[1,2], S. P. O'SULLIVAN[1,2], M. E. CORRIGAN[1], B. M. GAENSLER[1,2]

Submitted to The Astrophysical Journal.

ABSTRACT

Strong singly-ionized magnesium (MgII) absorption lines in quasar spectra typically serve as a proxy for intervening galaxies along the line of sight. Previous studies have found a correlation between the number of these MgII absorbers and the Faraday rotation measure (RM) at ≈ 5 GHz. We cross-match a sample of 35,752 optically-identified non-intrinsic MgII absorption systems with 25,649 polarized background radio sources for which we have measurements of both the spectral index and RM at 1.4 GHz. We use the spectral index to split the resulting sample of 599 sources into flat-spectrum and steep-spectrum subsamples. We find that our flat-spectrum sample shows significant ($\sim 3.5\sigma$) evidence for a correlation between MgII absorption and RM at 1.4 GHz, while our steep-spectrum sample shows no such correlation. We argue that such an effect cannot be explained by either luminosity or other observational effects, by evolution in another confounding variable, by wavelength-dependent polarization structure in an active galactic nucleus, by the Galactic foreground, by cosmological expansion, or by partial coverage models. We conclude that our data are most consistent with intervenors directly contributing to the Faraday rotation along the line of sight, and that the intervening systems must therefore have coherent magnetic fields of substantial strength ($\bar{B} = 1.8 \pm 0.4$ μG). Nevertheless, the weak nature of the correlation will require future high-resolution and broadband radio observations in order to place it on a much firmer statistical footing.

Subject headings: galaxies: magnetic fields — magnetic fields — polarization — quasars: absorption lines — radio continuum: galaxies

1. INTRODUCTION

Metal enriched gaseous structures, such as normal star-forming galaxies, can lie along the line of sight between us and a quasar (e.g. Churchill & Charlton 1999). These intervening galaxies are believed to give rise to absorption lines in an observed quasar spectrum, with the magnesium II (MgII) doublet appearing at $\lambda\lambda$2796, 2803 Å, in the rest-frame of the absorber. This lies in the optical from $z = 0.3$ to 2.4 and serves as a probe of low-ionization gas (e.g. Churchill & Charlton 1999; Jones et al. 2010). Detections of MgII absorption lines have therefore been used to infer the presence of an intervening system along the line of sight. In some cases these absorbers are associated with the quasar itself. However, in cases where the absorber is at a lower redshift than that of the quasar, the absorption is most likely taking place in an intervening galaxy between us and the quasar (i.e. a non-intrinsic system or an 'intervenor').

Faraday rotation is a powerful tool for measuring the magnetic field strength along the line of sight towards astrophysical objects. The combination of cosmic magnetic fields and charged particles causes rotation of the polarization angle of linearly polarized synchrotron emission from background radio sources (e.g. Longair 2011). Along a line of sight, the observed polarization angle is altered by an amount equal to

$$\Phi = \Phi_0 + \mathrm{RM}\lambda^2 , \quad (1)$$

where λ is the observing wavelength, Φ and Φ_0 are the measured and intrinsic polarization angles respectively, and the constant of proportionality RM, the 'rotation measure', is generally related to the integrated product of the electron number density, n_e, and the strength of the component of the magnetic field parallel to the line of sight, $B_\parallel$. The observed RM is also related to the redshift at which the Faraday rotating medium is located, but in practice this is typically a non-simple relationship, as there are actually multiple rotating media and it is not known where all of these media are distributed along the line of sight. Nevertheless, measurements of the RM can be used to infer the presence of magnetic fields and ionised gas somewhere along the line of sight between an observer and a source.

It has previously been suggested that there is a correlation between metal-line absorption and the RM of distant polarized sources (Kronberg & Perry 1982; Welter et al. 1984; Kronberg et al. 1990; Watson & Perry 1991; Oren & Wolfe 1995; Kronberg et al. 2008). More recent studies have extended these previous works by finding a correlation between the magnitude of the RM and the number of strong MgII absorbing systems along the line of sight (Bernet et al. 2008). This has been used to suggest that these intervening systems are magnetized, and that the magnetic fields in these intervening normal galaxies are of much higher strength than is typically expected in this earlier epoch of the Universe. This adds an extra challenge to our understanding of cosmic magnetism, as it implies the Faraday rotation towards a background quasar consists of a Galactic, intrinsic[3], and also an additional *intervening* contribution.

Bernet et al. (2008) inferred a population of intervening magnetized sources from RMs measured at relatively high radio frequencies, i.e. at $\approx$5 GHz, using a sample of 71 optical

jamie.farnes@sydney.edu.au
[1] Sydney Institute for Astronomy, School of Physics, The University of Sydney, NSW 2006, Australia.
[2] ARC Centre of Excellence for All-sky Astrophysics (CAASTRO).

[3] By intrinsic Faraday rotation, we refer to an additional component to the RM that occurs directly within a radio source or within the source's immediate environment, such that the Faraday rotation is directly related to the background quasar itself in some manner.

quasar spectra. The correlation claimed between the presence of MgII absorption lines and increased magnitude of RM is relatively weak, with a signal equivalent to a $\approx 1.7\sigma$ detection when comparing $N_{\rm MgII}$=0 and $N_{\rm MgII}$>0, where $N_{\rm MgII}$ is the number of MgII absorbers along a line of sight, and a $\approx 3.3\sigma$ detection between $N_{\rm MgII}$=0 and $N_{\rm MgII}$=2, albeit with only five sources with $N_{\rm MgII}$=2. This has been suggested as evidence that the intervening systems must increase the RM along the line of sight. Conversely, when using RMs measured at lower frequencies, i.e. at 1.4 GHz, the correlation between RM and the presence of MgII absorbers is consistent with no signal (Bernet et al. 2012), or with a weakly positive result at the 1.7σ level (Joshi & Chand 2013). This observed dichotomy between results at 1.4 GHz and 5 GHz has been used to suggest that the intervenors provide 'partial coverage', and obscure only a fraction of the background radio source (e.g. Bernet et al. 2012, 2013). Under such circumstances, Bernet et al. (2012) suggests that MgII absorbers provide partial coverage of the background source with an inhomogeneous Faraday screen, which could perhaps depolarize the high RM component at low radio frequencies – thereby giving rise to an observed 'Faraday complexity', i.e. a system with a non-linear relationship between polarization angle and squared wavelength so that RM$\rightarrow$RM(λ). As the sight lines with intervening systems that exhibit Faraday complexity appear associated with low fractional polarization at low frequency (Bernet et al. 2012), this has been interpreted as evidence of depolarization due to partial coverage. In addition, the suggested presence of partial coverage has also been inferred from polarized spectral energy distributions (SEDs) (e.g. Rossetti et al. 2008; Mantovani et al. 2009).

However, the apparent frequency-dependence of the effect could alternatively be a result of observational selection effects: at high and low radio frequencies we select different source populations, with different morphology and position in relation to the optical counterparts. Such relationships could also be caused by a number of confounding variables that require interpretation of their effect on the data. One possible proxy for overcoming these selection effects is the total intensity spectral index, α, defined such that $S \propto \nu^{+\alpha}$. In this paper, we attempt to take these selection effects and confounding variables into account. We re-examine the relationship between MgII absorption and RM from first principles, to determine whether this relationship extends to low observational frequencies. The consequences of such a relationship are important, as the emergence of magnetic fields in normal galaxies plays a strong role in star-formation in galaxy discs, drives the structure of the interstellar medium, influences other astrophysical processes that drive galaxy evolution, has implications for the cosmological growth of magnetic fields, and constrains dynamo mechanisms (e.g. Kulsrud & Zweibel 2008). Investigating such relationships may also provide the first conclusive empirical discriminant between theories of magnetic field amplification and structure. The standard α–Ω dynamo predicts that a small seed field is amplified by the combined action of differential rotation and turbulence on a large-scale in a galactic disk. These seed fields could be either primordial or have been generated by supernovae and amplified by dynamo action. Primordial fields could also be amplified in the process of the collapse of protogalaxies, or by dynamo action in oblique shocks as a protogalaxy collapses. Observational constraints on these competing models are currently lacking (e.g. Perry et al. 1993).

This paper is structured as follows: we present our observational data in Section 2, where we detail and justify how we created our sample and its properties. We detail the quantitative analysis of our main sample in Section 3, with the analysis of our subsamples being presented in Section 4. We discuss our results and the effect of confounding variables in Section 5, while a summary of the physical implications of our findings are presented in Section 6. In Appendix A, we argue that current mathematical models of partial coverage are incompatible with observational evidence. We refer to 'polarization' on multiple occasions, in all cases we are referring to linear radio polarization – both circular and optical polarization are beyond the scope of this work. All derived uncertainties are calculated using standard error propagation. Unless otherwise specified, all quantities are as measured in the observed-frame.

2. OBSERVATIONAL DATA

2.1. *Cross-Matching*

We use the broadband radio polarization catalog of Farnes et al. (2014) as our primary data source. This catalog accumulates and cross-matches data from throughout the literature over the last 50 years, taking resolution effects into account through the cross-matching criteria, and incorporating a significant number of major radio surveys including the NRAO VLA Sky Survey (NVSS), AT20G, B3-VLA, WENSS, NORTH6CM, GB6, and Texas (e.g. Simard-Normandin et al. 1980; Tabara & Inoue 1980; Simard-Normandin et al. 1981, 1982; Becker et al. 1991; Douglas et al. 1996; Gregory et al. 1996; Rengelink et al. 1997; Condon et al. 1998; Zukowski et al. 1999; Klein et al. 2003; Tingay et al. 2003; Taylor et al. 2009; Murphy et al. 2010).

The Farnes et al. (2014) catalog expands upon the NVSS RM catalog at 1.4 GHz (Taylor et al. 2009), providing total intensity spectral indices, α, for 25,649 sources, and polarization spectral indices, β, for 1,171 sources.[4] Furthermore, the catalog contains 951 polarized SEDs that are defined between 0.4 GHz to 100 GHz, with up to 56 independent polarization measurements per source. Farnes et al. (2014) use model fitting and an automated classification algorithm based on the Bayesian Information Criterion to distinguish between different models for Faraday depolarization and to constrain total intensity radio spectral indices and curvature. In attempting to fit physical models of depolarization to the data, the assumption is made that the polarization fraction, Π, is intrinsically a meaningful quantity that is related to the degree of magnetic field ordering in the source. Farnes et al. (2014) fit to the polarization angle as a function of wavelength, obtaining broadband RM measurements, and also include spectroscopic redshifts for 4,003 linearly polarized radio sources that were identified by Hammond et al. (2012) using various resources including the Sloan Digital Sky Survey (SDSS) (e.g. Abazajian et al. 2009).

In this paper, we cross-match the data from Farnes et al. (2014) with the catalog of Zhu & Ménard (2013), which presents a sample of 84,534 quasars with a total of 35,752 non-intrinsic MgII absorption systems along their lines of sight, as derived from SDSS spectra. Since the catalog of

[4] The polarized spectral index, β, is defined such that $\Pi \propto \lambda^{\beta}$, where Π is the polarized fraction and λ is the observing wavelength. Note that β is defined in the opposite sense to the total intensity spectral index, α, which is defined as $S \propto \nu^{+\alpha}$ and is the exponent of observing frequency rather than wavelength.

RM versus redshift (Hammond et al. 2012) and the catalog of MgII absorption (Zhu & Ménard 2013) are both based on data from the SDSS, one way to combine the catalogs would be to use an arbitrarily small cross-matching radius. However, Hammond et al. (2012) do not necessarily nominate the nearest SDSS source, as seen in projection on the sky, as the most likely matched candidate. The catalog instead provides a 'selected redshift' which is determined from the inclusion of other redshift catalogs and which takes into account the morphology of, for example, double-lobed radio sources. To combine the Zhu & Ménard (2013) data with the Farnes et al. (2014) catalog, we therefore use the redshift of the background quasar, z, in the cross-matching criteria. Cross-matching was carried out relative to the radio source positions provided by Taylor et al. (2009), each of which has an associated RM measurement at 1.4 GHz. For a match to be accepted, it must have been listed in the Hammond et al. (2012) catalog, be within an astrometric radius of $90''$ of the NVSS source position, and have a maximum redshift difference between the catalogs of Hammond et al. (2012) and Zhu & Ménard (2013) of $\Delta z \leq 0.05$. This additional criterion helps to eliminate false cross-matches by ensuring consistent redshifts throughout both datasets. Note that the $90''$ astrometric radius is only used to find associated radio emission, and it is the quasar redshift that is used to minimize the number of false matches. The cross-matching of optical and radio data, including complex morphological effects, has already been done rigorously by Hammond et al. (2012).

2.2. *Combining Radio and Optical Lines of Sight*

A typical model of an extragalactic radio source includes at least two components: (i) the core-region surrounding the active galactic nucleus (AGN) itself, and (ii) the radio lobes and/or jets. Where an extragalactic radio source is also detected at optical wavelengths, the bright optical counterpart is generally associated with the core. Since MgII absorption systems are optically identified, they only provide information on the presence of intervenors towards the core. The presence of an MgII absorber therefore provides no constraints on the presence of absorption towards the radio lobes or jets. Furthermore, at high frequencies we tend to select the flat-spectrum cores of radio sources, while at low frequencies we tend to select the steep-spectrum lobes and jets. As the lobes are physically offset from the cores, it is therefore possible that such an effect is 'diluting' the measured relationship between RM and the number of MgII absorbers, when measured at low frequencies. Analysing the polarized fraction and RM of an AGN at radio wavelengths within a finite resolution element will therefore potentially include contaminating polarized emission from the radio lobes and/or jets. Previous studies have not had the data available to investigate the extent of these contaminating effects. A sample that attempts to ensure that the core is probed at both radio and optical wavelengths will therefore assist in minimizing observational biases.

Note that we wish to probe the same emitting region[5] within the source at both optical and radio wavelengths, and not just as seen in projection in the plane of the sky. This is important for three reasons: (i) probing the same emitting region ensures that we are probing very similar lines of sight, (ii) this ensures that we make no assumptions with respect to the physical size of an intervening system, and (iii) it is the only way to guarantee we are not affected by projection effects – it is possible we could observe the core region at optical wavelengths, and meanwhile probe a lobe/jet at radio wavelengths as seen in projection on the sky. Point (iii) highlights that the requirement is not just for similar lines of sight, but for similar emitting regions. One cannot easily attempt to confirm that the emitting regions are coincident for an unresolved radio source using positional offsets only, i.e. offsets in the plane of the sky, as very unresolved sources would incorrectly appear to emit from the same region at both optical and radio wavelengths. This is potentially important at the $\approx 45''$ resolution of the NVSS as used here. It is also not possible to explore projection effects using positional offsets of data with mismatched resolution – for example, a steep-spectrum radio lobe can appear to be coaligned with an optical core, despite both physical features not emanating from the same line of sight. We therefore highlight that without the introduction of either multiple simplifying assumptions or very long baseline interferometric data, the same physical line of sight cannot be trivially probed using merely the alignment of radio and optical counterparts.

We therefore suggest an improved measure of the same emitting region, and by extension the same physical line of sight. This can be provided by the total intensity spectral index, α. A prototypical model of an extragalactic radio source is one that consists of at least two emitting regions: (i) a flat-spectrum core ($\alpha \approx 0$), and (ii) steep-spectrum jets/lobes ($\alpha \approx -0.7$). The spectral index therefore serves as a powerful discriminator of the physical emitting region that is largely independent of both resolution and projection effects. Although unresolved radio sources can contain emission from both the core region and the jets/lobes, the spectral index allows us to determine from which physical region the emission dominates. Consequently, flat-spectrum sources can be used as a proxy for the optical and radio counterparts being aligned (i.e. a core-dominated source), and steep-spectrum sources for those not aligned (i.e. a lobe-dominated source). This provides a reliable divider between different physical emitting regions and by extension of different lines of sight, while simultaneously reducing the likelihood of selecting regions that are merely aligned through projection or resolution effects. It is likely that the sources would need to be angularly resolved in order to completely eliminate such projection effects, although we believe this is only a very infrequent effect in our sample.

2.3. *Our Sample*

The cross-matching process provides an initial sample in which each source has a measurement of the number of MgII absorbing systems along the line of sight, the redshifts of the background quasar and of the intervening systems, and also a polarized fraction and an RM measurement at 1.4 GHz (Taylor et al. 2009; Hammond et al. 2012; Zhu & Ménard 2013; Farnes et al. 2014). We also have supplementary data on the equivalent width of each absorbing system. All of the MgII absorption lines are non-intrinsic (aka intervening) (Zhu & Ménard 2013), and are blue-shifted from their background quasar by at least $\Delta z = 0.04$.

To improve the quality of our sample, we exclude sources that are best modeled by a curved spectrum in total intensity

[5] We use the term 'region' to describe the corresponding surrounding area within the source in which there are similar physical conditions, e.g. the core-, jet-, or lobe-regions. The same emitting region, in this case, is unlikely to correspond to emission from the same physical material at both optical and radio wavelengths, although it is likely to be separated by only a very small angle on the sky.

(Farnes et al. 2014), keeping only sources that were best fit by a conventional power law. To avoid poor-quality total intensity spectral indices in our sample, we exclude sources with a reduced-$\chi^2 \geq 4.0$. As the data used to construct the SEDs were taken at different epochs, more variable sources may tend to have an increased reduced-χ^2 – we are therefore likely selecting the least variable sources, in addition to those with low measurement errors. In order to minimize the effects of the Galactic foreground, we discard sources at Galactic latitudes $|b| \leq 25°$. A full discussion of foreground effects is provided in Section 4.5.

We are also primarily concerned with the *strong* absorbing systems. Based upon statistical arguments, it historically had been suggested that very small rest-frame equivalent width MgII absorption did not exist (e.g. Steidel & Sargent 1992). However, due to high signal–to–noise and high-resolution spectroscopy, the detection thresholds eventually dropped below the previous sensitivity levels of 0.3 so that this could be tested through observation (e.g. Tripp et al. 1997; Churchill & Charlton 1999). The conventional divider between strong and weak MgII absorption is therefore assumed throughout the literature, by definition, to be at a rest-frame equivalent width of 0.3 (e.g. Rigby et al. 1998; Barton & Cooke 2009). We therefore, in this paper, consider the strong absorbers to be those with an equivalent width $W_\mathrm{r} \geq 0.3$ Å. Most contemporary studies have found that both strong and weak MgII absorbers are associated with different clouds of material: strong absorbers are typically associated with outflows from star-forming normal galaxies (e.g. Bordoloi et al. 2014), whereas weak absorbers may be related to the outskirts of normal galaxies, dwarf galaxies, material stripped through tidal interactions, and low surface-brightness galaxies (e.g. Churchill et al. 1999). Our initial sample contained both strong and weak absorbers, although it was dominated by strong absorbers. We calculate the mean rest-equivalent width, $\overline{W_\mathrm{r}} = (W_{2796} + W_{2803})/2$, using the data of Zhu & Ménard (2013). Absorbing systems with $\overline{W_\mathrm{r}} < 0.3$ Å ($n = 31$) were excluded from the rest of our analysis. This final sample contains 599 sources. We shall refer to this as the 'main sample'. From Farnes et al. (2014), we also have a measurement of the total intensity spectral index, α, for 548 of these sources. The main sample contains 398 sources without MgII absorption and 201 sources with strong non-intrinsic MgII absorption. Of the absorbing lines of sight, 152 contain a single MgII absorber, 38 contain two absorbers, 10 contain three absorbers, 0 contain four absorbers, and 1 contains five absorbers.

The size of our sample is an improvement of almost an order of magnitude upon that of Bernet et al. (2008), which contained measurements of MgII absorption and RM for 71 quasar spectra, and is also 10% larger than the sample of Joshi & Chand (2013), which contained 539 measurements of quasar spectra and RM but did not have spectral index information available. Our sample is further assisted by the high-reliability of the MgII data, which have both a purity and a completeness of $> 95\%$ (Zhu & Ménard 2013).

Using the spectral indices, we further split the sources into two subsamples: 'flat-spectrum' ($\alpha \geq -0.3$) and 'steep-spectrum' ($\alpha \leq -0.7$). The gap in spectral index from $-0.7 < \alpha < -0.3$ serves to avoid cross-contamination between the two samples. Our flat-spectrum subsample contains 87 sources with no absorber, 39 with one absorber, and 16 with more than one absorber. Our steep-spectrum subsample contains 154 sources with no absorber, 62 with one absorber, and 16 with more than one absorber.

Table 1
The total sample size and the number of lines of sight with a given number of strong MgII absorbing systems ($W_\mathrm{r} \geq 0.3$ Å). The sample size is listed for both the main sample and the defined subsamples.

		N_MgII						
Sample Name	N_total	0	1	2	3	4	5	>0
Main (All sources)	599	398	152	38	10	0	1	201
Flat-spectrum[a]	142	87	39	12	4	0	0	55
Steep-spectrum[b]	232	154	62	11	4	0	1	78

[a] $\alpha \geq -0.3$
[b] $\alpha \leq -0.7$

Estimates of many other parameters are available in the catalog of Farnes et al. (2014), but are in a regime of small sample statistics after cross-matching with the MgII catalog. We therefore exclude these other variables from our analysis, and consider only the RMs and polarized fractions at 1.4 GHz, and the depolarization spectral indices. There is insufficient sample size for an analysis of the broadband RMs or weak MgII absorbers.

The main, flat-spectrum, and steep-spectrum samples, are all summarized in Table 1. The source coordinates and other properties of our main sample are listed in Appendix B.

3. MAIN SAMPLE ANALYSIS

We first perform an analysis similar to that of Joshi & Chand (2013), and use our main sample to look for differences between the RMs and polarized fractions at 1.4 GHz of sources with N_MgII =0, 1, and ≥ 2 MgII absorbers (irrespective of whether each source has a spectral index measurement). In order to test whether any differences are statistically significant, we calculate the empirical cumulative-distribution functions (ECDFs) and statistical measures for various aspects of our main sample, both with and without non-intrinsic MgII absorption systems along the line of the sight. Our flat- and steep-spectrum subsamples will be presented in Section 4. For all of our analyses, we take a frequentist approach and use the two-sample Kolmogorov–Smirnov test (KS-test) for which the null hypothesis is that the ECDFs are calculated from independent samples drawn from the same underlying population. The p-values we obtain therefore indicate the probability of getting a result as extreme as or greater than the one obtained, if the null hypothesis is true. Note that the p-value only provides the probability with which one would reject the null-hypothesis, if it *were* correct – it provides no information on the probability that the null hypothesis *is* correct, i.e. we have calculated $p(\geq D|H_0)$ and not $p(H_0|D)$. This test is non-parametric, i.e. it does not assume that the data are sampled from any particular distribution. We will on occasion refer to the 'p-value' and the 'probability' interchangeably – unless otherwise specified, we refer to $p(\geq D|H_0)$, the probability of the two samples being as different as observed, or more so, if drawn from the same distribution.

3.1. *Rotation Measure at 1.4 GHz*

The ECDFs of the NVSS RMs from the main sample for N_MgII =0, 1, and ≥ 2 are shown in Fig. 1. The KS-test provides a p-value of 17% for sources with $N_\mathrm{MgII} = 0$ and > 0. We also obtain a p-value of 77% between sources with $N_\mathrm{MgII} = 0$ and 1.

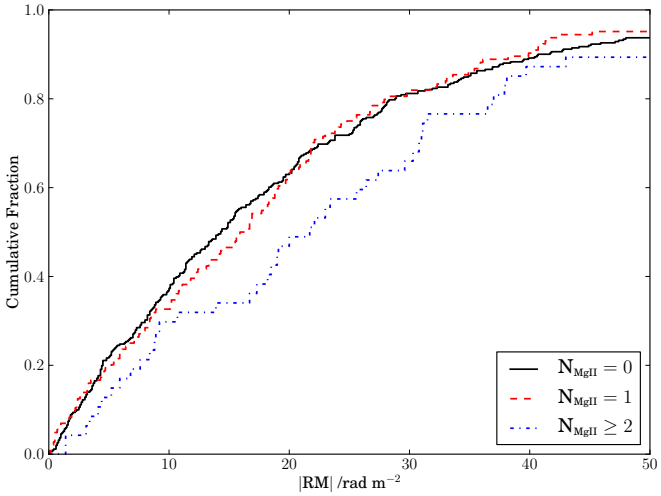

Figure 1. ECDFs of the absolute value of the NVSS RMs for all 599 sources in the main sample. The black solid line shows the 398 sources without MgII absorption along the line of sight, the red dashed line shows the 152 sources with 1 absorbing system, and the blue dotted line shows the 49 sources with $\geq$ 2 absorbing systems. There is no statistically significant difference between the three samples.

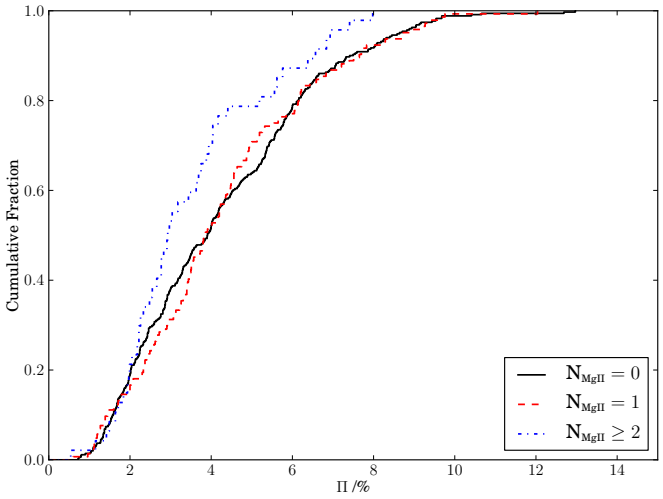

Figure 2. ECDFs of the NVSS polarized fractions for all 599 sources in the main sample. The black solid line shows the 398 sources without MgII absorption along the line of sight, the red dashed line shows the 152 sources with 1 absorbing system, and the blue dotted line shows the 49 sources with $\geq$ 2 absorbing systems. There is no statistically significant difference between the three samples.

For sources with $N_{\rm MgII} = 0$ and 2, the p-value is 2.9%. There is no significant difference between any of the ECDFs. This is consistent with the results of Bernet et al. (2012) and Joshi & Chand (2013).

3.2. *Polarized Fraction*

The ECDFs of the NVSS polarized fractions from the main sample are shown in Fig. 2. The KS-test provides a p-value of 25% for sources with $N_{\rm MgII} = 0$ and > 0. We also obtain a p-value of 60% between sources with $N_{\rm MgII} = 0$ and 1, and a p-value of 3.5% between sources with $N_{\rm MgII} = 0$ and 2. There is no significant difference between any two of the ECDFs. This indicates that MgII absorption has no significant effect on the polarized fraction of sources at 1.4 GHz. This is consistent with the results of Bernet et al. (2012).

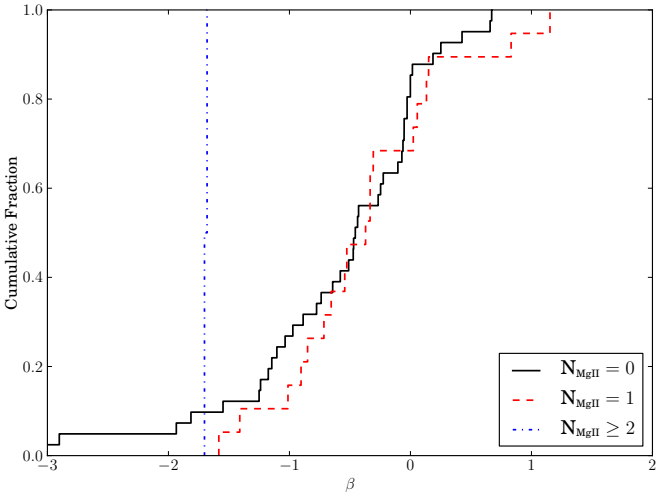

Figure 3. ECDFs of the Farnes et al. (2014) polarization spectral indices for all 62 sources in the main sample with complementary depolarization information. The black solid line shows the 41 sources without MgII absorption along the line of sight, the red dashed line shows the 19 sources with 1 absorbing system, and the blue dotted line shows the 2 sources with $\geq$ 2 absorbing systems. There is no statistically significant difference between the three samples.

3.3. *Polarization Spectral Indices*

The ECDFs of the Farnes et al. (2014) polarization spectral indices, β defined such that $\Pi \propto \lambda^{\beta}$, are shown in Fig. 3. Of the sources in the main sample, there is complementary depolarization information for 41 sources without an absorber, 19 sources with one absorber, and 2 sources with two or more absorbers. The KS-test provides a p-value of 82% for sources with $N_{\rm MgII} = 0$ and > 0. We also obtain a p-value of 66% between sources with $N_{\rm MgII} = 0$ and 1, and a p-value of 3.4% between sources with $N_{\rm MgII} = 0$ and 2. There is no significant difference between any two of the ECDFs. This suggests that MgII absorption has no significant effect on the depolarization of sources.

4. FLAT- AND STEEP-SPECTRUM SUBSAMPLE ANALYSIS

We now extend our analysis to the flat- and steep-spectrum subsamples as defined in Section 2. As a frequentist 'significance' tends to be subjective, we shall provide a summary of our results, and individually consider both the significance and the effects of confounding variables in Section 5. While we consider the redshift distribution of our sample in Section 4.4, we are unable to trivially separate our sample based on luminosity, which has been calculated assuming an optically-thin synchrotron emitting region (Farnes et al. 2014). The physical meaning of such a calculation is unclear due to beaming and in the presence of self-absorption due to an optically-thick emitting region, as might be occurring if flat-spectrum sources are core-dominated AGN. As shall be shown, the flat-spectrum subsample is the most important in which to check for luminosity effects.

4.1. *Rotation Measure at 1.4 GHz*

Our sample is displayed in histograms of the number of MgII absorbers with different RMs at 1.4 GHz in Fig. 4. For the flat-spectrum subsample, the sources with $N_{\rm MgII} > 0$

appear to have a greater dispersion in the absolute value[6] of RM relative to the steep-spectrum sources. We now test this statistically.

The ECDFs of the RMs of the flat- and steep-spectrum sources are shown in Fig. 5. From the top panel, the difference between the flat-spectrum sources with versus without MgII absorption has a p-value of 0.044% of being this large or larger if drawn from the same underlying distribution. Meanwhile, the steep-spectrum sources have a p-value of 90%. This difference between the flat- and steep-sources is also identified from the ECDFs displayed in the middle and bottom panels; flat-spectrum sources with 0 and 1 (0 and 2) absorbers have a p-value of 0.37% (0.24%), while steep-spectrum sources with 0 and 1 (0 and 2) absorbers have a p-value of 65% (54%). For only sources with no absorption, the difference between the flat- and steep-sources has a p-value of 29%.

4.2. *Polarized Fraction*

The ECDFs of the polarized fractions, Π, for flat- and steep-spectrum sources are shown in Fig. 6, for sources that are both with and without an absorber. The flat-spectrum sources with/without MgII absorption have a p-value of 56%. Meanwhile, the steep-spectrum sources have a p-value of 11%.

4.3. *Polarization Spectral Indices*

The ECDFs of the Farnes et al. (2014) polarization spectral indices, β, are shown in Fig. 7 (By flat- and steep-spectrum, we still refer to the total intensity spectral index, α). For the flat-spectrum subsample, there are complementary β measurements for 9 sources without an absorber, 5 sources with one absorber, and 1 source with two absorbers. For the steep-spectrum subsample, there are complementary β measurements for 15 sources without an absorber, 7 sources with one absorber, 0 sources with two absorbers, and 1 source with three absorbers. The KS-test provides a p-value of 58% between flat-α sources with $N_{\rm MgII} = 0$ and > 0, and a p-value of 78% between steep-sources with $N_{\rm MgII} = 0$ and > 0. There is a known difference between the depolarization of flat- and steep-α sources, as discussed by Farnes et al. (2014). Nevertheless, there is no significant difference detected between sources with and without absorbers, regardless of whether the source has flat- or steep-α. Our data are consistent with the presence of intervening MgII absorbers having no effect on the depolarization of sources, although we note that the sample size is very small.

4.4. *Redshift*

The ECDFs of the redshifts, z, for flat- and steep-spectrum sources are shown in Fig. 8, for sources with varying numbers of MgII absorbers. The flat-spectrum sources with versus without MgII absorption have a p-value of 1.0%. Meanwhile, the steep-spectrum sources have a p-value of 0.00003%. In our sample, the radio sources with intervening absorbers clearly tend to be located at higher redshifts. However, all flat- and all steep-spectrum sources have a p-value of 80.5% – there is no statistically significant difference between the flat- and steep-spectrum distributions.

[6] Note that the sign of the RM tells us only about the direction of the magnetic field along the line of sight. Here we are interested only in the field strength, which is best traced by |RM|. For consideration of the Galactic foreground, see Section 4.5.

4.5. *The Galactic Foreground*

One possibility to explain the apparent difference between flat-spectrum sources both with and without MgII absorption, as detailed in Section 4.1, is that it is the consequence of contributions to the Faraday rotation from the Galactic foreground. It is typically assumed that the observed RM = GRM + RRM, where RRM contains contributions from both the background source environment and also the extragalactic line of sight, and GRM is the contribution from the Galaxy (e.g. Hammond et al. 2012). Nevertheless, it has been suggested that while the Galactic foreground *can* be estimated using surveys such as the NVSS, it *cannot* be reliably subtracted to obtain an RRM without knowing the relative uncertainties (Oppermann et al. 2014). Regardless, we expect the effect of the Galactic foreground to be low, as we have removed sources at low Galactic latitudes from our sample (see Section 2) and we would expect sources with high RMs to be preferentially located in the Galactic plane (e.g. Taylor et al. 2009). For the foreground to be influencing our main results, our sample would have to be anisotropically distributed on the sky such that there was either a difference in the RM of flat- and steep-spectrum sources, or of sources with differing numbers of MgII absorbers. Therefore if the Galactic foreground was causing our result, we could expect a different estimation of GRM between these different samples.

To investigate the possibility of the Galactic foreground affecting our result, we plot the ECDFs of the GRM. As various foreground estimation methods have been previously proposed (e.g. Taylor et al. 2009; Hammond et al. 2012; Oppermann et al. 2014; Xu & Han 2014b), we use two independent techniques to ensure there is no dependence on the method used for foreground correction. In both cases, we use the NVSS RMs (Taylor et al. 2009) as the input to the reconstruction algorithm.

i For the first algorithm, for each point source we find the mean RM of all sources within an 8° radius of the central source while excluding the central source itself (e.g. Oren & Wolfe 1995). We refer to this as the 'mean RM' algorithm.

ii For the second algorithm, we use the reconstruction of Oppermann et al. (2014) which uses the extended critical filter formalism that is derived within the framework of information field theory (see e.g. Oppermann et al. 2012, 2014, for further details).

The ECDFs of the GRM as calculated using the 'mean RM' algorithm, for flat- and steep-sources with $N_{\rm MgII} = 0$, 1, and 2 respectively, are shown in Fig. 9. The difference in GRM of flat-spectrum sources with $N_{\rm MgII} = 0$ versus 1, and also $N_{\rm MgII} = 0$ versus 2 absorbers, gives p-values of 19% and 69% respectively. The difference in GRM of steep-spectrum sources with $N_{\rm MgII} = 0$ versus 1, and also $N_{\rm MgII} = 0$ versus 2 absorbers, gives p-values of 68% and 11% respectively. The difference in GRM of flat- and steep-spectrum sources gives a p-value of 79%.

The ECDFs of the GRM as calculated using the Oppermann et al. (2014) algorithm, for flat- and steep-sources with $N_{\rm MgII} = 0$, 1, and 2 respectively, are also shown in Fig. 9. The difference in GRM of flat-spectrum sources with $N_{\rm MgII} = 0$ versus 1, and also $N_{\rm MgII} = 0$ versus 2 absorbers, gives p-values of 60% and 41% respectively. The difference in GRM of steep-spectrum sources with $N_{\rm MgII} = 0$ versus 1, and also $N_{\rm MgII} = 0$ versus 2 absorbers, gives p-values of 74% and 23% respectively. The difference in GRM of flat- and steep-

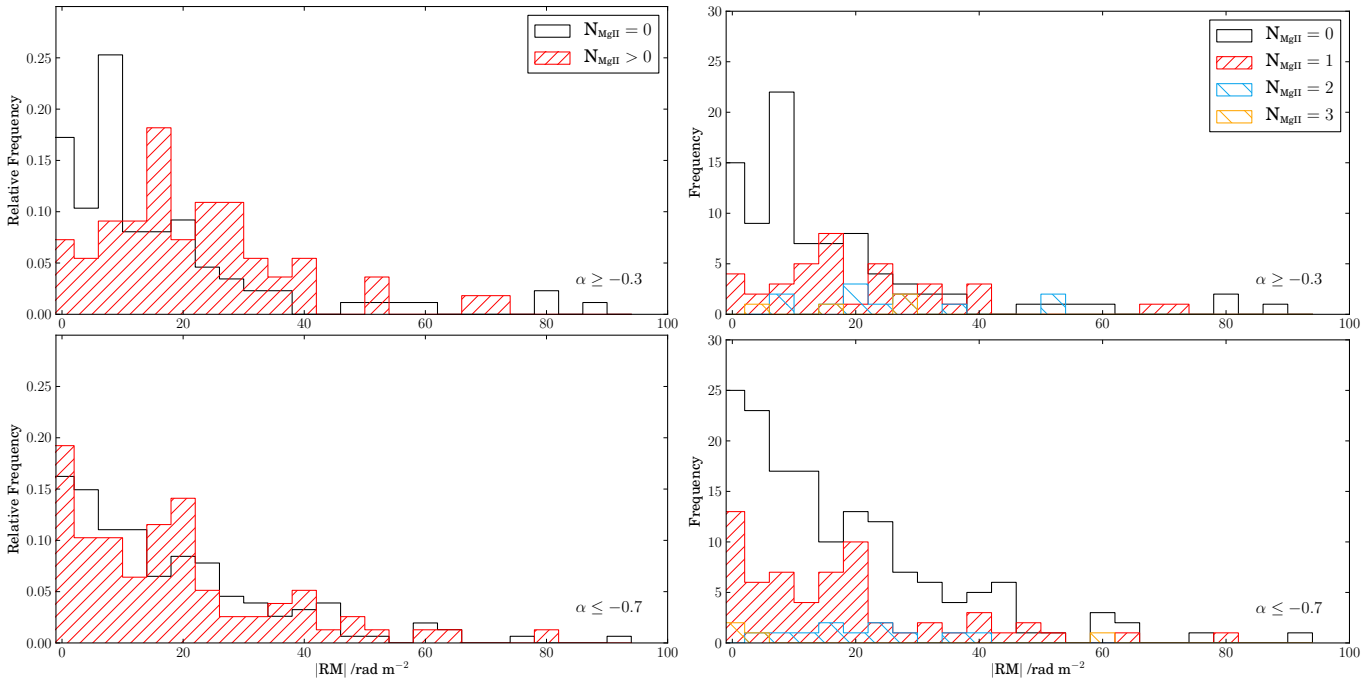

Figure 4. Histograms showing the number of lines of sight with a given number of MgII absorbing systems, as a function of |RM|. Both the flat-spectrum (top row) and steep-spectrum (bottom row) subsamples are displayed. Histograms are shown for the cases where the number of MgII absorption systems along the line of sight, $N_{\rm MgII}$, is either equal to zero or greater than zero (left column) and for each individual number of MgII absorbers (right column). Values of $N_{\rm MgII}$ are displayed in the legend to the top-right of the upper plots. Note that the histograms in the left column are normalized; those in the right column are not.

spectrum sources gives a p-value of 53%.

There is no detectable difference for the GRM of different sources in our sample. This is also independent of the reconstruction algorithm used to calculate the Galactic foreground. Any difference due to the GRM is therefore unable to recreate our result presented in Section 4.1. This is consistent with the Galactic foreground not being responsible for flat-spectrum sources with intervening absorbers having increased RM.

5. DISCUSSION

5.1. *Magnetic Fields in Intervening Galaxies*

There are several apparent correlations between variables in Section 3 and 4 with p-values at the $\approx 5\%$ to 10% level. While these correlations may be real, one should remain suspicious. As we use p-values, any significance is subjective. Such effects, if they exist at all, must be very weak, and we believe such a low significance level to be most consistent with the null hypothesis being true, i.e. there is no connection between the two variables (e.g. Johnson 2013). On this basis, we have only two statistically significant results, (i) the flat-spectrum sources are consistent with intervening MgII absorption systems increasing the measured RM at 1.4 GHz towards background quasars, while the same correlation is not seen for steep-spectrum sources (as discussed in Section 4.1), and (ii) both the redshifts of flat- and steep-spectrum sources are consistent with lines of sight with higher numbers of MgII absorbers tending to be located at significantly higher redshift (as discussed in Section 4.4).

One could argue that such results are caused by the Galactic foreground, but we note that this is inconsistent with our observational findings (see Section 4.5). One could also argue that such results are contrary to previously suggested partial coverage models (which imply no connection between RM and MgII absorption at 1.4 GHz; see Section 1), but we note that although such models are useful for parameterizing the run of polarized fraction with wavelength, they do not describe a physical depolarization model (see Appendix A). We hypothesize that such partial coverage models are actually the result of probing different emitting regions within the source at different observational frequencies, rather than the effects of any foreground Faraday screen. Importantly, this suggests that in many cases the polarized fraction, which is typically used to estimate the degree of order of magnetic fields, is not a physically meaningful quantity for an *unresolved* source (see Appendix A).

Nevertheless, as discussed in Section 2.2, flat-spectrum sources ($\alpha \approx 0$) can be used as a proxy for a source from which the emission is dominated by the core-region, while steep-spectrum sources ($\alpha \approx -0.7$) are dominated by emission from the region of the lobes and jets. By applying this interpretation, let us therefore consider the correlation between MgII absorption and RM in flat-spectrum, aka core-dominated, sources. In the event that no correlation exists, we would expect to have detected a signal at least this strong for just $\approx$1 in 2,250 experiments – making the result equivalent to a 3.5σ event from a normally distributed process. We have therefore either observed a low probability event, or it must be true that there is a connection between RM and MgII absorption in core-dominated sources, while not in jet/lobe-dominated sources. Such evidence suggests that the spectral index is important for discriminating between core- and lobe-dominated sources, and is a reasonable proxy for matching lines of sight at different wavelengths.

As the intervening MgII absorbers are identified towards quasar cores at optical wavelengths, the intervenors can only be said to be obscuring the core at radio wavelengths. An optically selected MgII absorber does not provide an indication of the presence of intervenors along the line of sight towards the lobes/jets. We therefore form three conclusions

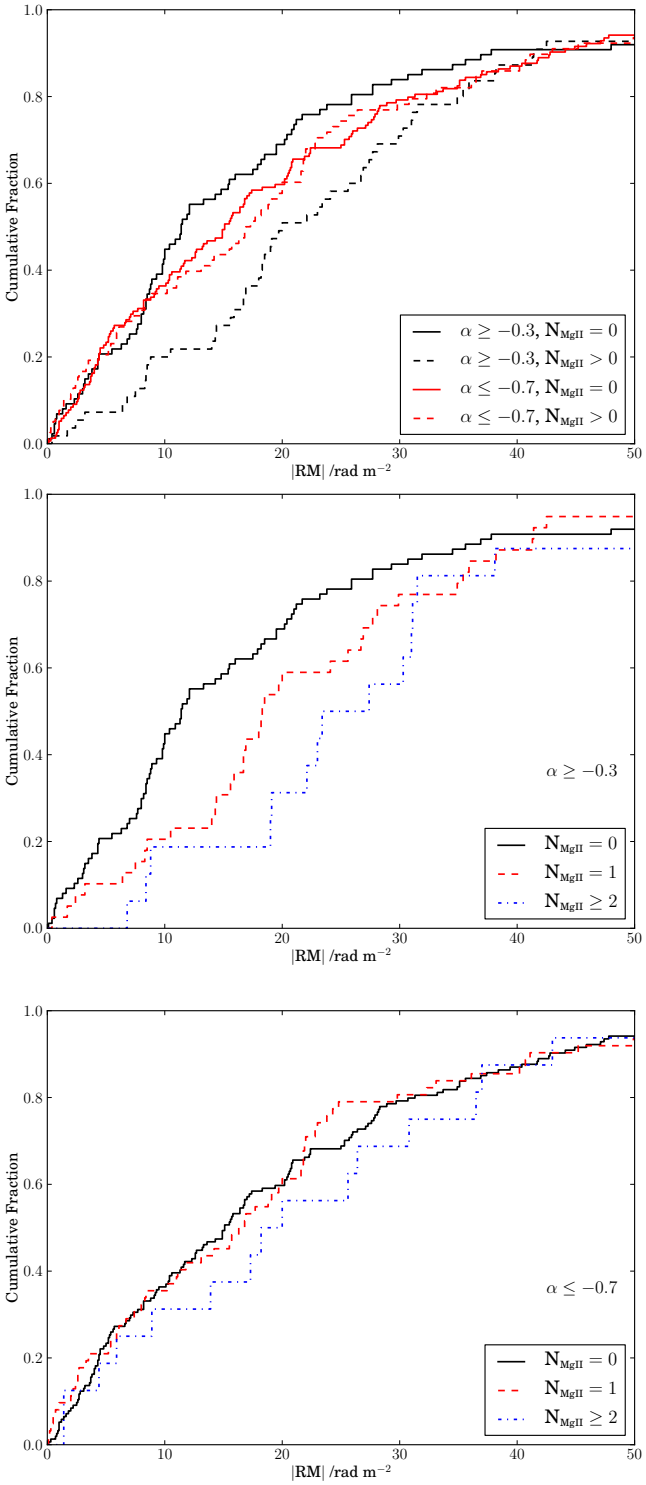
Cumulative Fraction
|RM| /rad m^{-2}
$\alpha \geq -0.3$, $N_{MgII} = 0$
$\alpha \geq -0.3$, $N_{MgII} > 0$
$\alpha \leq -0.7$, $N_{MgII} = 0$
$\alpha \leq -0.7$, $N_{MgII} > 0$
$\alpha \geq -0.3$
$N_{MgII} = 0$
$N_{MgII} = 1$
$N_{MgII} \geq 2$
$\alpha \leq -0.7$

Figure 5. ECDFs of the absolute value of the NVSS RMs for (i) Top panel: flat- (black), and steep- (red) spectrum sources. The solid lines show the sources without MgII absorption, while the dashed lines show the sources with ≥ 1 absorbing system along the line of sight, (ii) Middle panel: flat-spectrum sources only, (iii) Bottom panel: steep-spectrum sources only. In (ii) and (iii), the black solid lines show the sources without MgII absorption along the line of sight, the red dashed lines show the sources with 1 absorbing system, and the blue dotted lines show the sources with ≥ 2 absorbing systems.

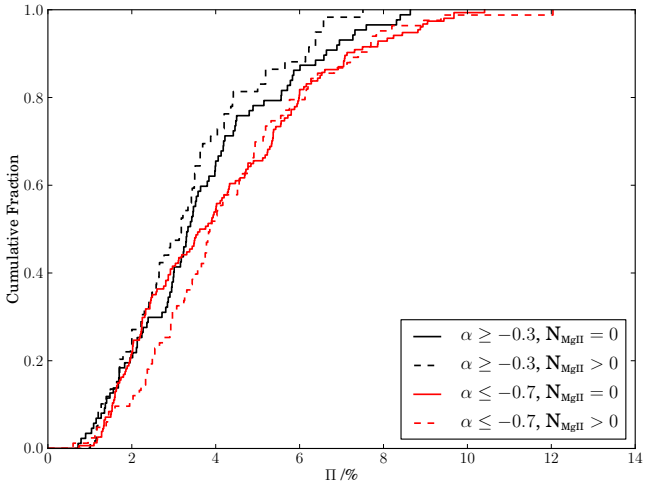

Figure 6. ECDFs of the NVSS polarized fraction, Π, for flat- (black), and steep- (red) spectrum sources. The solid lines show the sources without MgII absorption, while the dashed lines show the sources with ≥ 1 absorbing system along the line of sight.

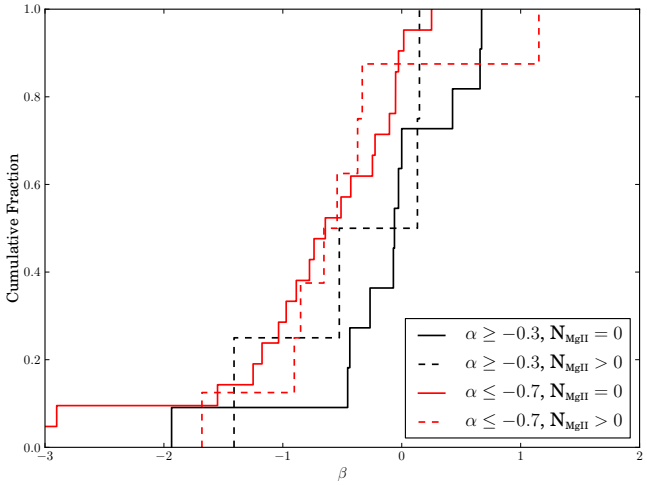

Figure 7. ECDFs of the Farnes et al. (2014) polarization spectral indices, β, for flat- (black), and steep- (red) spectrum sources. The solid lines show the sources without MgII absorption, while the dashed lines show the sources with ≥ 1 absorbing system along the line of sight.

from Fig. 5:

i The observed difference in RM between flat-spectrum sources with and without absorption arises due to intervening magnetized plasma in the absorbing systems – the flat-spectrum of the source ensures that we probe the same line of sight towards the background quasar independently of projection and resolution effects,

ii There is no difference in RM between steep-spectrum sources with and without absorption as we are usually probing different lines of sight at optical and radio wavelengths – this effect is particularly important at longer radio wavelengths where the steep-spectrum lobes/jets tend to dominate the radio emission,

iii Any difference detected between the flat- and steep-spectrum sources without absorbers could be due to two effects. Firstly, the steep-spectrum sources are only nominally identified as having no absorption. In reality, we likely have not accurately identified the same optical and radio sight line for the steep-spectrum sources. Secondly, the very high RM components of the core may

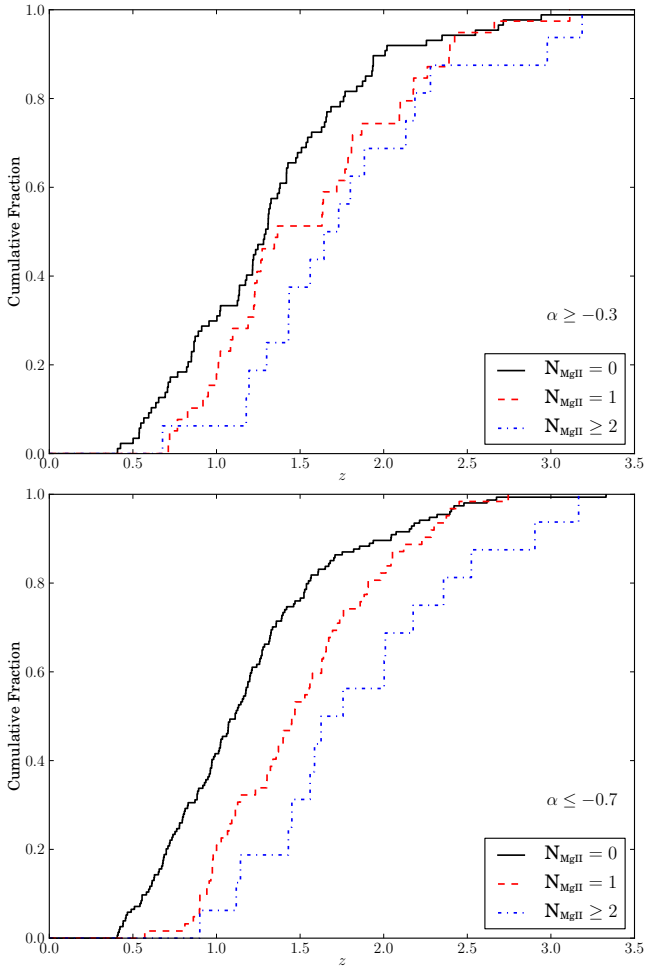

Figure 8. ECDFs of the background quasar redshifts for flat- (top), and steep- (bottom) spectrum sources. The black solid line shows the sources without MgII absorption along the line of sight, the red dashed line shows the sources with 1 absorbing system, and the blue dotted line shows the sources with ≥ 2 absorbing systems. In our sample, the quasars with intervening absorbers tend to be located at higher redshifts. However, there is no statistically significant difference between the flat- and steep-spectrum distributions.

have depolarized at 1.4 GHz, so that only lower RM components are still observable.

To provide a quantitative estimate of the excess RM associated with intervening galaxies, we assume that the correlation between MgII absorption and RM for flat-spectrum sources has an entirely physical origin. We calculate the median RMs in order to ensure robustness, and as a simplifying assumption use Gaussian statistics to calculate the 1σ uncertainties. Using the difference observed in flat-spectrum sources (as shown in Fig. 5), we therefore obtain RM[N_{MgII}=0] = 11.4 ± 2.2 rad m^{-2}, RM[N_{MgII}=1] = 18.3 ± 2.6 rad m^{-2}, and RM[$N_{MgII} \geq 2$] = 25.4 ± 3.3 rad m^{-2} for lines of sight with 0, 1, and $\geq$2 absorption lines respectively. The simplest estimate of the intervening contribution is given by RM[N_{MgII}=1]–RM[N_{MgII}=0], so that our data suggests the excess RM associated with a typical intervening system is 6.9 ± 1.7 rad m^{-2} in the observing frame. This is consistent with previous estimates of excess extragalactic contributions to the RM (Hammond et al. 2012).

For lines of sight with just one absorbing system, the median redshift of the intervening galaxies is 0.87 ± 0.06. Therefore assuming that the Faraday rotation is a linear function with λ^2, this implies an RM contribution of the order 24 ± 6 rad m^{-2} in the source rest-frame for a typical intervening cloud of magnetized plasma. This is generally lower than previous estimates obtained at higher radio frequencies, that have estimated rest-frame contributions from 115^{+45}_{-30} rad m^{-2} (Kronberg et al. 2008) to 140^{+80}_{-50} rad m^{-2} (Bernet et al. 2008). Our estimate improves upon these earlier works as we have both higher statistical significance and have also been able to separate the source contributions based on the total intensity spectral index, although it may also imply some Faraday complexity (see Section 1).

Following the model presented in Bernet et al. (2008), and assuming that MgII absorbing systems with rest-frame equivalent widths between 0.3 to 0.6 are associated with galaxies with a neutral-hydrogen column density of 10^{19} cm^{-2} and a hydrogen ionization fraction of 0.90, we estimate that the typical magnetic field strength associated with each of the intervening systems is $\bar{B} = 1.8 \pm 0.4$ μG. Consequently our data are consistent with, and provide the strongest statistical indication to date for, the idea that magnetic fields of substantial strength and coherence were present in normal galaxies in the distant Universe (e.g. Kronberg & Perry 1982; Welter et al. 1984; Kronberg et al. 1990; Watson & Perry 1991; Oren & Wolfe 1995; Bernet et al. 2008; Kronberg et al. 2008; Bernet et al. 2012, 2013; Joshi & Chand 2013).

We cannot currently calculate any physical quantities from the steep-spectrum sources, as we argue that we do not have reliable measurements of whether these sources are truly covered with an absorber. However, as $\approx 50\%$ of sources are believed to have an intervening absorber (Zhu & Ménard 2013), one would expect both of the steep-spectrum distributions to sit between the flat-spectrum distributions, which is entirely consistent with the observations (see Fig. 5).

Our result suggests that different source-components, and consequently different lines of sight, result in the MgII absorption versus RM signal being diluted at 1.4 GHz unless core- and lobe-type sources are considered separately. This divide suggests that either the typical intervenor must be small in angular size relative to the size of the background galaxy, that there is a sharp boundary to the magnetoionic medium in the intervenor, or that the MgII absorbing gas is highly localised within a host galaxy. However, even when separating the sample based on total intensity spectral index, we find no difference in the depolarization of either flat- or steep-sources that have intervening absorption (see Section 4.3). If any depolarization is present due to intervenors, the contribution must be weak. This suggests the magnetic field in the typical intervening galaxy is regular and ordered, at least within the region that is illuminated by background emission.

5.2. *Correlation versus Causation*

It is possible to conflate correlation and causation, and so we also examine the possibility that our results could be obtained through systematic effects or confounding variables within our data. There are a number of possible ways in which spurious correlations could be detected in our data, given the presence of some confounding variable. We now explore alternate hypotheses that may explain our finding that our data are consistent with flat-spectrum sources with intervening absorbers having increased RM.

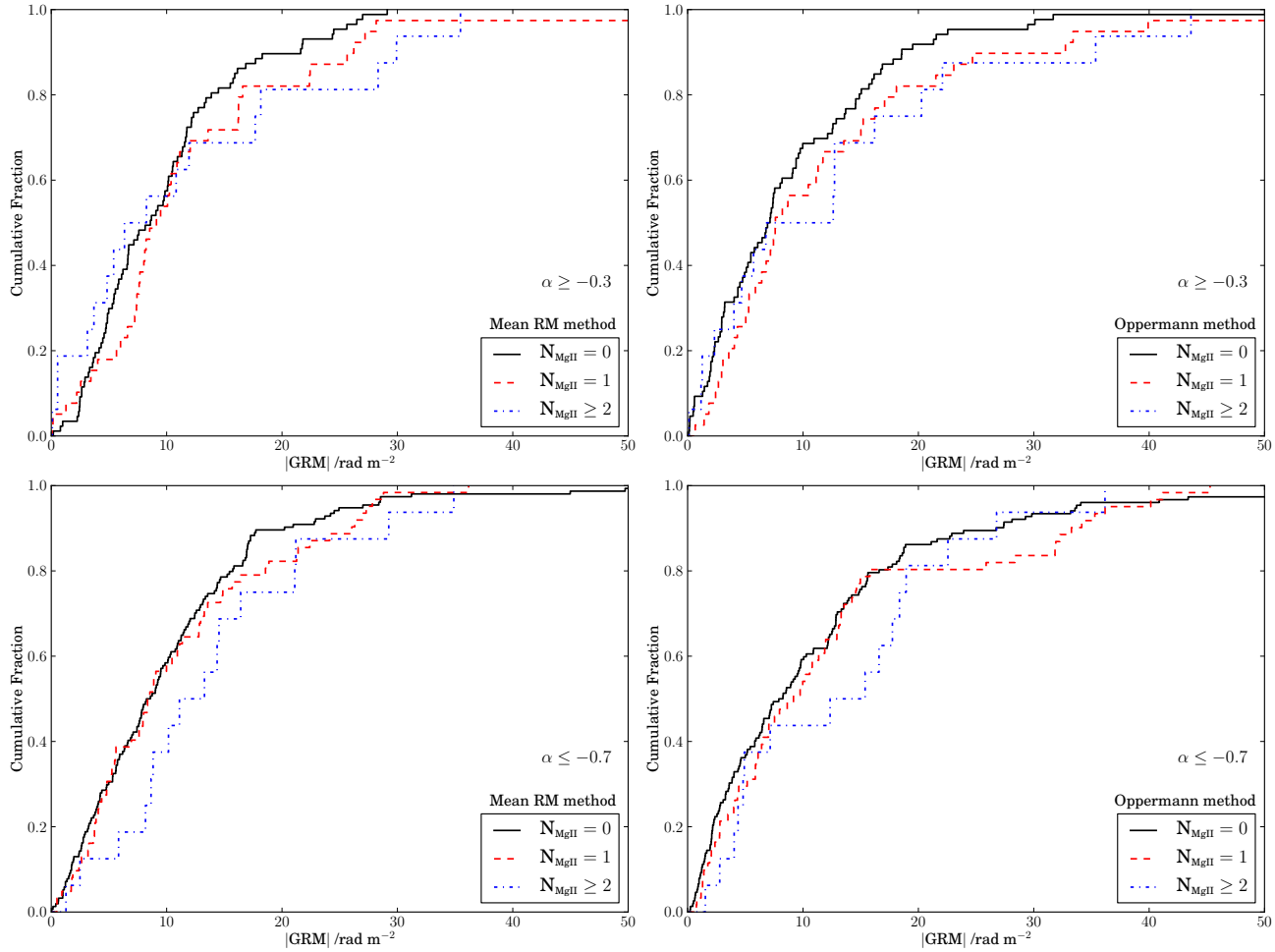

Figure 9. ECDFs of the absolute value of the Galactic foreground RMs as calculated using two different algorithms: (i) Left column: the 'mean RM' method, (ii) Right column: the Oppermann et al. (2014) method. The top panels show the flat-spectrum sources only, while the bottom panels show the steep-spectrum sources only. The black solid lines show the sources without MgII absorption along the line of sight, the red dashed lines show the sources with 1 absorbing system, and the blue dotted lines show the sources with ≥ 2 absorbing systems. There is no significant difference between any of the data.

5.2.1. *Evolution of Faraday Rotation with Redshift*

The most obvious alternate cause for our observed main result would be that the probability that a quasar line of sight intersects an MgII absorber increases as a function of z, and that some effect unrelated to the intervenors causes $|\mathrm{RM}| \propto z$. The former is observed in our data as shown in Fig. 8. Consequently any other property that causes the |RM| to scale positively with z will also manifest as a correlation between RM strength and the number of intervenors. This evolution in |RM| may be due to change in either the integrated magnetic field strength, the electron density, or both along the line of sight.[7]

In such cases, the distribution in z of the sample will determine the magnitude of the spurious correlation, i.e. a small range or a uniform distribution in z yields a weak correlation, while conversely a wide range or a highly non-uniform distribution in z yields a strong correlation. To test this, one would ideally resample the data by redshift-binning the flat- and steep-spectrum sources into equal bins, thereby providing a uniform distribution as a function of redshift. We are unable to do this and form firm conclusions as we increasingly fall into the realm of small-sample statistics. However, we are still able to discard such a possibility, and note that a connection between RM and the number of MgII absorbers (as in Fig. 5) is not detected for the steep-spectrum sources, despite both the flat- and steep-spectrum sources showing a similar relation between the number of absorbers as a function of z (as in Fig. 8). A KS-test comparing the distribution of redshifts for flat- versus steep-spectrum sources yields a p-value of 7.6% for zero absorbers, 81% for one absorber, and 99% for two or more absorbers. Such low significance levels are most consistent with the null hypothesis being true, i.e. there is no quantitative difference between the redshift distributions of the flat- and steep-spectrum sources. This suggests a longer line of sight towards a source is not in itself responsible for an increase in RM within our data, and that while sources with more absorbers in our sample are located at higher redshifts, this is equally true for both the flat- and steep-spectrum sources. A spurious correlation that arises due to the sources with absorbers being

[7] Any evolution can in principle be detected, with the exception of special cases where $B_{\parallel}$, n_e, and the $(1+z)^{-2}$ dilution factor evolve in such a way that the observed-frame RM remains approximately constant. The physics of such models and their applicability to our data, particularly when adding additional intervening contributions to the RM that are each located at different redshifts, is beyond the scope of this paper.

located further away is therefore not consistent with the observed difference between flat- and steep-spectrum sources.

To explain the observed difference between flat- and steep-spectrum sources, given the distribution of our sample with redshift, therefore requires another hypothesis. Consider if the flat-spectrum sources were evolving as a function of z, while the steep-spectrum sources were not evolving. In such a scenario, we propose that some mechanism causes flat-spectrum sources to have a higher observed-frame RM at higher redshift. We now discuss the possibilities that could cause the observed-frame RM to appear to be scaling as a function of z in flat-spectrum sources, while not in steep-spectrum sources. These explanations broadly fall into two categories: (i) systematic observational effects, and (ii) astrophysical source evolution. Note that we have already discussed the separate possibility of an increased likelihood of a line of sight intersecting an intervenor at higher redshifts.

First we consider systematic observational effects. Our data contain the typical luminosity–redshift degeneracy that is inherent to a flux-limited survey such as the NVSS, as lower luminosity sources at high z are not detected in a flux-limited survey. This selection-effect is commonly termed Malmquist bias. The observed correlation between the number of MgII absorbers and RM for flat-spectrum sources in our sample, therefore implies a *smaller* RM along the line of sight towards the *fainter* flat-spectrum sources, or conversely a *larger* RM towards the *brighter* flat-spectrum sources. Overall, this requires some mechanism that causes the measured RM at fixed-frequency towards flat-spectrum sources to tend to be smaller for low luminosity sources; these sources then drop below the detection threshold at high z and we perceive a net increasing RM. This would be consistent with relativistic beaming models that state that compact, flat-spectrum radio sources are seen at small viewing angles, with weaker cores being seen at progressively larger viewing angles (e.g. Saikia et al. 1987). This suggests that: (a) those weaker cores at larger angles are poorly sampled at high z within a flux-density limited survey (leading to a luminosity effect), and (b) the line of sight through host galaxies with large viewing angles could possibly be reduced, giving rise to lower values of RM for these cores at larger angles (depending on the distribution of electrons and magnetic field near to the central engine). Note that such a scenario need not affect the RM observed towards steep-spectrum sources. Nevertheless, such an effect would appear to be in contradiction to previous studies which have directly measured the evolution of RM as a function of z, using either independent data or the same data as in our sample – with both analyses finding no significant evolution with either redshift or luminosity (Zavala & Taylor 2004; Hammond et al. 2012). More recently, it has been argued that a correlation may have been found, but no analysis of the statistical significance or of confounding factors is currently available (Pshirkov et al. 2014).

A second possibility is evolution of the sources themselves. If the RM towards quasar cores increased with z, while the RM towards lobes/jets remained approximately constant, this would explain the observed correlation. Note that as the same effect is not seen for lobe-dominated sources, this rules out the additional contribution to the RM being located anywhere along the line of sight, and implies that flat-spectrum sources have a higher RM at high z that originates within the local source environment. This is in direct contradiction to theoretical expectations (Beck et al. 1996), current observational data (e.g. Hammond et al. 2012; Xu & Han 2014a), and the expected strong $(1+z)^{-2}$ cosmological dilution effect which arises due to cosmic expansion (e.g. López 2006) – all of which suggest that observed-frame RMs, as a proxy for magnetic fields, should be smaller at earlier epochs.

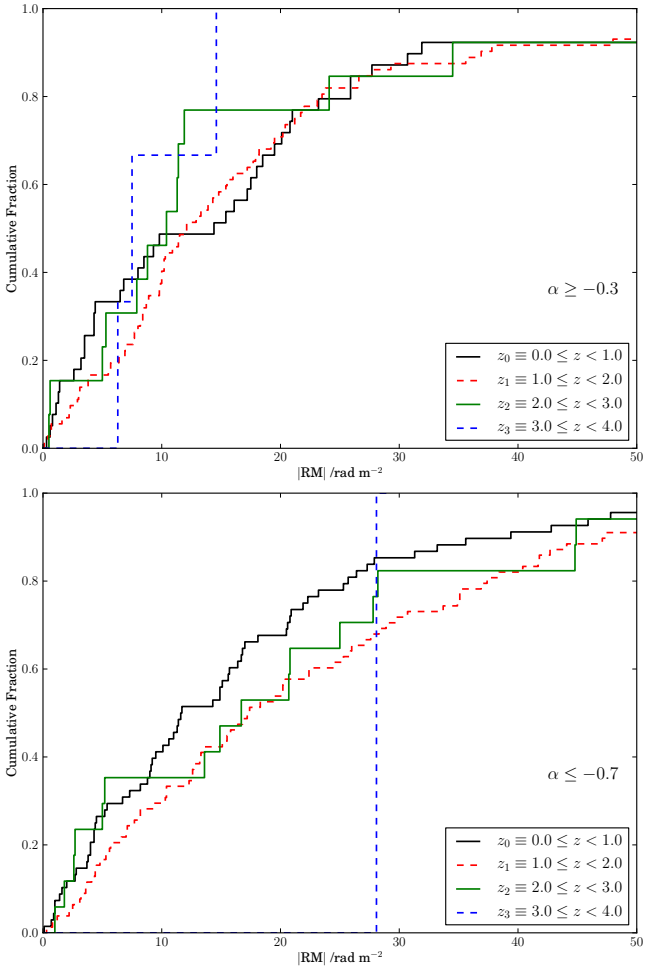
Cumulative Fraction
|RM| /rad m^{-2}
$\alpha \geq -0.3$
$z_0 \equiv 0.0 \leq z < 1.0$
$z_1 \equiv 1.0 \leq z < 2.0$
$z_2 \equiv 2.0 \leq z < 3.0$
$z_3 \equiv 3.0 \leq z < 4.0$
$\alpha \leq -0.7$

Figure 10. ECDFs of the absolute value of the NVSS RMs as a function of the background quasar redshift, z. Only sources that have a 'clean' line of sight are shown, thereby probing the environment of the background quasars, i.e. sources with $N_{\rm MgII} = 0$. Both flat- (top panel) and steep-spectrum (bottom panel) sources are shown. The quasars are separated into four redshift bins: $0.0 \leq z < 1.0$ (black solid line), $1.0 \leq z < 2.0$ (red dashed line), $2.0 \leq z < 3.0$ (green solid line), and $3.0 \leq z < 4.0$ (blue dashed line), that in the main text we refer to as z_0, z_1, z_2, and z_3 respectively. There is no significant difference between any of the data.

To investigate all of these possibilities, we use the data to look for an evolution of RM versus z in both the flat- and steep-spectrum sources of our sample. We split the data into four bins using the background quasar redshifts: $0.0 \leq z < 1.0$, $1.0 \leq z < 2.0$, $2.0 \leq z < 3.0$, and $3.0 \leq z < 4.0$, which we shall here refer to as z_0, z_1, z_2, and z_3 respectively. As it is possible that previous studies of RM versus z have been affected by contributions from intervening sources along the line of sight, we only use sources that have no detected MgII absorber along the line of sight. To date, no study has been able to investigate the evolution of RM versus z for 'clean' lines of sight, allowing us to attempt to probe evolution in the local environment of the background quasars themselves. Note that all of our sample are optically identified

as quasars in the SDSS (see Section 2). Our results are shown in Fig. 10. For flat-spectrum sources, there is a p-value of 38% between z_0 and z_1, of 36% between z_0 and z_2, and of 39% between z_0 and z_3. For steep-spectrum sources, there is a p-value of 14% between z_0 and z_1, of 75% between z_0 and z_2, and of 23% between z_0 and z_3. There is no statistically significant difference between any of the ECDFs and thus there is no detectable evolution of RM as a function of z in our sample. This is consistent with luminosity effects or source evolution not being responsible for flat-spectrum sources with intervening absorbers having increased RM. One could argue that variations in the GRM (see Section 4.5) could mask any RM variation with redshift. While the results presented in Fig. 10 cannot rule this out, this scenario still cannot explain how flat-spectrum sources with absorbers have higher RMs, as it would require selection of different GRMs for sources with different numbers of absorbers. Fig. 9 shows that there is no observable difference in GRM between these same flat-spectrum sources both with and without absorbers, which suggests that the GRM is not affecting our results.

We note that such an analysis cannot be trivially performed for sources with intervening absorbers, as the measured RM then becomes a combination of the RM at the quasar plus then presumably additional components from the multiple absorbers themselves, all of which are located at different redshifts. Our analysis is further complicated by bandwidth depolarization in the NVSS sample for sources with $|\mathrm{RM}| \geq 350$ rad m^{-2} (Taylor et al. 2009), as such high RMs could be entirely located at high or low redshift. Nevertheless, this cannot be a significant effect in the RM ECDFs unless a very large fraction of our sources had such an RM – which is unlikely given our removal of sources at low Galactic latitudes.

5.2.2. *Systematic Observational Effects*

In Section 5.2.1, we discussed systematic observational effects such as Malmquist bias that may have generated the observed correlations in our data. We now discuss another systematic effect that could possibly explain our observation that flat-spectrum sources with intervening absorbers having increased RM. This effect is directly related to the signal–to–noise ratio (s/n) of each measurement.

In this alternative hypothesis, we suggest that the more distant sources tend to be fainter in either total or polarized intensity. As the sources with more absorbers are located more distantly in our sample, this could lead to a systematic error. As the NVSS RMs are calculated using two closely-spaced narrow bands (Taylor et al. 2009), a decrease in the s/n could lead to anomalous RM measurements. In this case, the polarized intensity from which the RM is determined, serves as a proxy for the s/n.

To investigate this possibility, we plotted the ECDFs of the polarized and total intensity for flat- and steep-spectrum sources with different number of MgII absorbers as shown in Fig. 11. There are a number of different data subsets: (i) For the polarized intensity data from flat-spectum sources, there is a p-value of 53% between sources with zero and one absorbers, and a p-value of 69% between sources with zero and two absorbers. For the polarized intensity data from steep-spectum sources, there is a p-value of 35% between sources with zero and one absorbers, and a p-value of 11% between sources with zero and two absorbers. The p-value between the polarized intensity of the flat- and steep-spectrum sources themselves is 91%, (ii) For the total intensity data from flat-spectum sources, there is a p-value of 8.2% between sources with zero and one absorbers, and a p-value of 59% between sources with zero and two absorbers. For the total intensity data from steep-spectum sources, there is a p-value of 80% between sources with zero and one absorbers, and a p-value of 50% between sources with zero and two absorbers. The p-value between the total intensity of the flat- and steep-spectrum sources themselves is 96%. There is therefore no statistically significant difference in either the polarized or total intensity of sources with different numbers of absorbers in our sample – our main results are therefore not caused by the effects of s/n.

5.2.3. *k-corrected Polarized Quantities*

All of the aforementioned possibilities neglect the necessity of k-corrections to observed polarization quantities. It is possible that wavelength-dependent polarization structure in the nucleus can mimic Faraday rotation – particularly through the combined interplay of synchrotron self-absorption and depolarization within a compact emitting region (e.g. O'Dea 1988). Broadband observations may therefore be able to detect Faraday complexity in flat-spectrum sources (i.e. a non-linear relationship between polarization angle and λ^2). There is already some tentative evidence to support this (O'Sullivan et al. 2009, 2012; Farnes et al. 2014). Note that it has been previously suggested that sight lines with intervening systems that exhibit Faraday complexity are also associated with low fractional polarization (Bernet et al. 2012). It could be attempted to explain this as a selection effect, with the high-frequency RMs selecting for the flat-spectrum component of the source, and the 1.4 GHz RMs selecting for the steep-spectrum component – thereby generating a pseudo Faraday complexity that arises from the sampling of different emitting regions. Nevertheless, this does not explain why these same sources have a low fractional polarization. However, flat-spectrum NVSS sources have also been shown to have a lower median fractional polarization than steep-spectrum sources (Mesa et al. 2002; Stil et al. 2014). We therefore suggest the alternative hypothesis that Faraday complex sources may be intrinsically flat-spectrum, and that splitting the NVSS sample by fractional polarization, as done by Bernet et al. (2012), selects these flat-spectrum sources. In such cases, as the NVSS RM is measured at fixed-frequency, we would be sampling different regions of this polarization structure at different redshifts, as seen in the source rest-frame. In such a case, the necessary k-correction would not just be equivalent to a cosmological dilution factor of $(1+z)^2$, but would rather be a consequence of redshifting a curvilinear run of polarization angle versus λ^2, while observing with a fixed narrow bandwidth (Farnes et al. 2014).

We could therefore consider a convoluted toy model that requires k-corrections to the run of polarization angle versus λ^2 in a Faraday complex source. Given the narrow bandwidth used to derive the 1.4 GHz RMs in our sample, the data would have to probe progressively higher rest-frame frequencies at high z, which would correspond to the region closer to the central engine, which could have undergone less depolarization at high frequency. In turn, this region closer to the central engine could correspond to a greater pathlength through the source environment, which could possibly lead to larger Faraday rotation. Such an observational effect would not affect the lobe-dominated (aka steep-spectrum) sources, that have ordered magnetic fields on large scales and

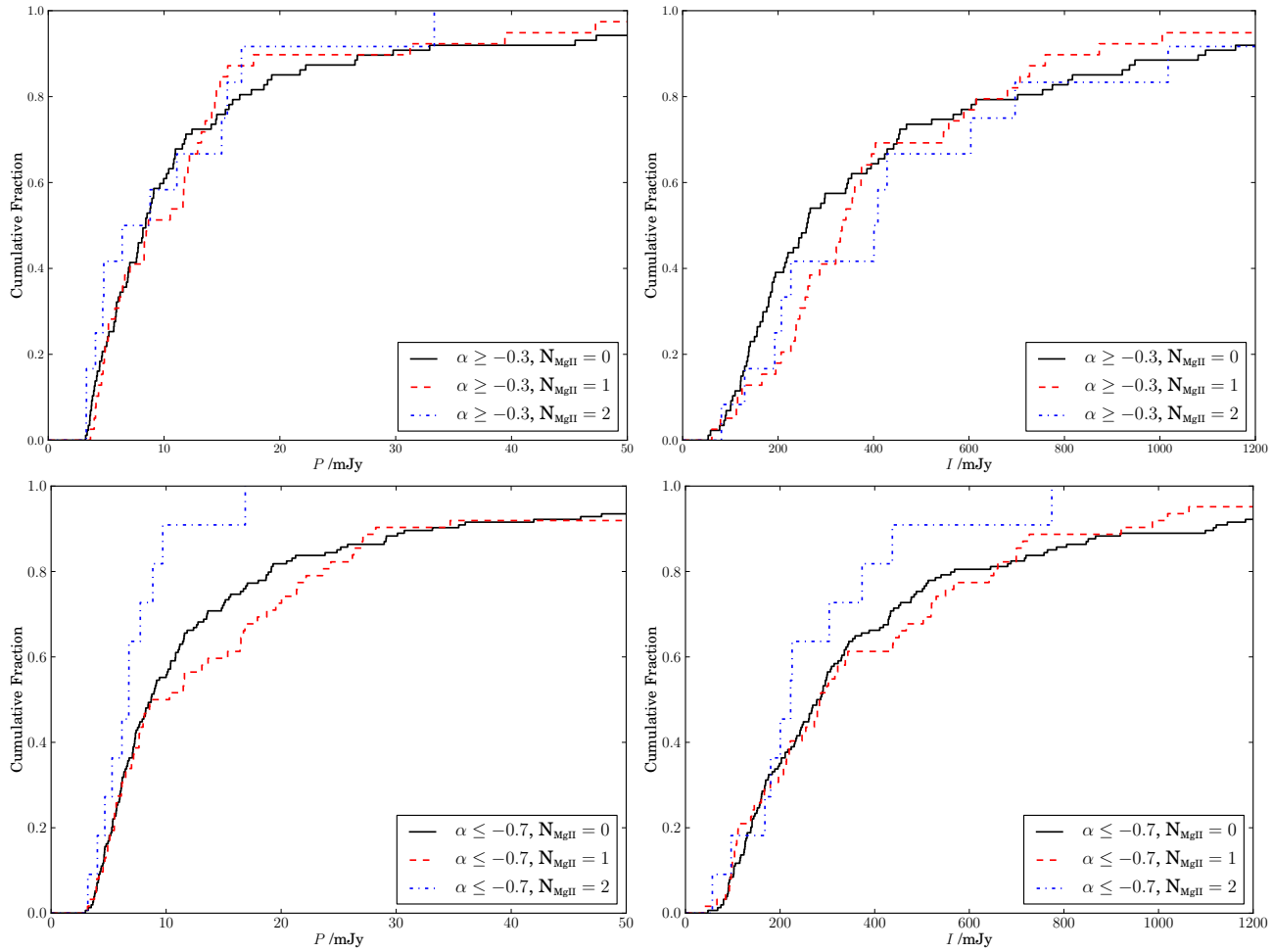

Figure 11. ECDFs of the NVSS polarized intensity (left column) and total intensity (right column) for different numbers of MgII absorbers. Both flat-spectrum ($\alpha \geq -0.3$, top row), and steep-spectrum ($\alpha \leq -0.7$, bottom row) subsamples are shown. Data are shown for sources with $N_{\rm MgII} = 0$ (black solid line), $N_{\rm MgII} = 1$ (red dashed line), and $N_{\rm MgII} = 2$ (blue dot-dashed line). The polarized and total intensity both serve as a proxy for the s/n of each measurement – particularly the polarized intensity, from which the NVSS RMs are derived. There is no significant difference between any of the data.

are optically-thin (leading to simple Faraday rotation, and a linear run of polarization angle with λ^2). While intriguing, our data are inconsistent with this proposed model for a number of reasons. Previous studies have shown that opacity effects are important in the run of polarized fraction SEDs, allowing flat-spectrum sources to repolarize (Farnes et al. 2014). This is hard to reconcile with the requirement of depolarization in this proposed alternative hypothesis. The proposed toy model also contradicts the observation that weak MgII absorbers are not correlated with RM along the line of sight (Bernet et al. 2010), as this further suggests that there cannot be an additional confounding variable, i.e. no evolution of quasar magnetic fields with z. One could counter that the nature of weak MgII absorbing systems is still poorly understood (e.g. Churchill et al. 1999, 2005; Narayanan et al. 2007; Kacprzak et al. 2008), or that previous studies have not separated sources based on the spectral index. Regardless, the proposed toy model would still require a strong evolution of the observed-frame RM as a function of z for flat-spectrum sources. As shown in Fig. 10, there is no observed RM evolution in the flat-spectrum sources of our sample. There is only one remaining possibility: that our data are consistent with intervening systems, as traced by MgII absorption, containing regular magnetic fields that increase Faraday rotation along the lines of sight towards distant background quasars.

6. CONCLUSIONS

We have investigated the current theoretical and observational understanding of Faraday effects originating along the line of sight due to intervening heavy-metal absorbing systems. We have divided a sample of flat- and steep-spectrum radio sources into subsamples both with and without MgII absorption along the line of sight. We have been able to use these samples as a proxy for core- (flat-spectrum) or lobe- (steep-spectrum) dominated sources. This has allowed us to study the same sight line at both optical and radio wavelengths. We find that the core-dominated sample has a larger |RM| when intervening MgII absorbers are present, with a probability of 0.044% of the increase in |RM| being this large or greater if the data were drawn from the same underlying distribution. Conversely to previous studies, which have found no association between MgII absorption and Faraday rotation at 1.4 GHz, we instead find evidence of an association that is stronger than that which has been presented before at any other observing frequency.

We have considered various alternative effects, including

varying luminosity in our essentially flux-limited sample, evolution of magnetic fields with redshift, and other more elaborate possibilities that may cause a spurious correlation. We find that none of them are fully consistent with both our data and our theoretical understanding of cosmic magnetism. The simplest way to explain our observations while remaining consistent with previous observational findings is to require the RM to be increased by additional magnetic fields, or ionised gas, that are associated with intervening MgII absorbing systems along the line of sight. If we assume that the correlation between MgII absorption and RM has an origin entirely due to intervening galaxies, then as a quantitative estimate, our data suggest that a typical absorber provides an additional RM contribution of 6.9 ± 1.7 rad m^{-2} in the observing frame. At the median redshift of our sample, $z = 0.87 \pm 0.06$, this implies an RM contribution of 24 ± 6 rad m^{-2} from a typical intervening cloud of magnetized plasma in the source rest-frame. Consequently our data are consistent with, and provide the strongest statistical indication to date for, the idea that coherent magnetic fields of substantial strength ($\bar{B} = 1.8 \pm 0.4$ μG) are present in what are presumed to be normal galaxies (e.g. Kronberg et al. 2008). The possibility that Faraday rotation along the line of sight to a typical quasar could be enhanced by an otherwise essentially invisible population of intervening normal galaxies is an intriguing one. The physical implications of this have been rigorously explored elsewhere, providing constraints for our understanding of galaxy formation and evolution, magnetic field generation, and dynamo mechanisms (Kronberg & Perry 1982; Welter et al. 1984; Kronberg et al. 1990; Watson & Perry 1991; Oren & Wolfe 1995; Bernet et al. 2008; Kronberg et al. 2008; Bernet et al. 2012, 2013; Joshi & Chand 2013).

Our data complement previous studies by showing that connections between RM and MgII absorption are still detectable at lower radio frequencies, and that the contribution from intervening systems to the overall Faraday rotation along the line of sight must be weak relative to that from the background quasars. It is also indicates the importance of probing similar lines of sight at optical and radio wavelengths, suggesting that projection effects between cores and lobes have been important contributors to previous studies. However, while our method of using the total intensity spectral index to identify the same line of sight at different wavelengths is a significant primary step, we do not currently have the data available to definitively confirm that the polarized emission is coincident with the total intensity emission. Investigating such potential systematics would likely require full reprocessing of surveys such as the NVSS, or the arrival of next generation surveys such as the Polarization Sky Survey of the Universe's Magnetism (POSSUM) that will be carried out with the Australian Square Kilometre Array Pathfinder (ASKAP) (Gaensler et al. 2010).

The significance of the correlation between intervening absorption lines and RM is currently only at a level equivalent to a 3.5σ event from a normally distributed process, although we note that we have been unable to calculate either a confidence interval, or the probability of the hypothesis. In future studies, a full Bayesian framework would be useful to further analyse our statistical detection. Our data show that connections between intervening systems and Faraday rotation are difficult to detect, due to the multiple effects that may alter the RM at cosmological distances. Placing the interaction on an even firmer statistical footing will require multiple quantities: larger samples of strong MgII absorbers, higher angular resolution radio data, unambiguous RMs, broadband spectral indices, and improved estimates of the Galactic foreground. Future observations with facilities such as the Square Kilometre Array (SKA) will therefore be important in confirming these results with much greater statistical significance, and for determining the physical properties of the intervening systems themselves, such as improved estimates of the typical magnetic field strength, the physical size, and any redshift dependence of the magnetic field properties. The combination of existing radio morphology classifications (Hammond et al. 2012), other radio surveys such as FIRST (White et al. 1997), and measurements of the spectral index (see Section 2.2), will also form the foundation of a useful future study. The intervenors themselves could also have implications for an SKA 'RM-grid' (e.g. Gaensler et al. 2004), as RM measurements from core-dominated sources may have a more complex relation to the magnetic field of the Galactic foreground. This would impede attempts to calculate a residual rotation measure (see Section 4.5) using multiple lines of sight within some defined region of sky (e.g. Taylor et al. 2009; Hammond et al. 2012; Oppermann et al. 2014). Broadband measurements of core-dominated sources, combined with reconstructions of the Galactic foreground using simulated data, will be required to investigate such possibilities.

Overall, the new evidence presented here rules out models of partial coverage by inhomogeneous Faraday screens (see Section 1); the justification for such models has been based on the lack of connection between the number of MgII absorbers and the RM at 1.4 GHz. Taken together with the connection between radio depolarization and total intensity spectral index (Farnes et al. 2014), our results serve as a reminder of the importance of opacity effects on radio polarization measurements. In combination, these results suggest that depolarization is predominantly occurring in the local environment of the background AGN, while the RM is significantly contributed to by the intervening normal galaxy population. The consequences are important for all future and upcoming radio polarimetric studies.

ACKNOWLEDGEMENTS

We are grateful to the anonymous referee for helpful comments on the original version of the manuscript. J.S.F., S.P.O'S., & B.M.G. acknowledge the support of the Australian Research Council through grants DP0986386, FS100100033, & FL100100114 respectively. Parts of this research were conducted within the Australian Research Council Centre of Excellence for All-sky Astrophysics (CAASTRO), through project number CE110001020. The National Radio Astronomy Observatory is a facility of the National Science Foundation operated under cooperative agreement by Associated Universities, Inc. This research has made use of: the SIMBAD database, operated at Centre de Données astronomiques de Strasbourg, France; the NASA/IPAC Extragalactic Database (NED) which is operated by the Jet Propulsion Laboratory, California Institute of Technology, under contract with NASA; NASA's Astrophysics Data System Abstract Service; the SDSS, for which funding has been provided by the Alfred P. Sloan Foundation, the Participating Institutions, the National Science Foundation, and the U.S. Department of Energy Office of Science.

REFERENCES

Abazajian, K. N., Adelman–McCarthy, J. K., Agüeros, M. A., et al., 2009, ApJS, 182, 543.
Arshakian, T. G., Beck, R., 2011, MNRAS, 418, 2336.
Barton, E. J., Cooke, J., 2009, AJ, 138, 1817.
Beck, R., Brandenburg, A., Moss, D., Shukurov, A., Sokoloff, D., 1996, ARA&A, 34, 155.
Becker, R. H., White, R. L., & Edwards, A. L. 1991, ApJS, 75, 1.
Bernet, M. L., Miniati, F., Lilly, S. J., Kronberg, P. P., & Dessauges-Zavadsky, M. 2008, Nature, 454, 302.
Bernet, M. L., Miniati, F., & Lilly, S. J. 2010, ApJ, 711, 380.
Bernet, M. L., Miniati, F., & Lilly, S. J. 2012, ApJ, 761, 144.
Bernet, M. L., Miniati, F., & Lilly, S. J. 2013, ApJ, 772, 28.
Bordoloi, R., Lilly, S. J., Kacprzak, G. G., Churchill, C. W., 2014, ApJ, 784, 108.
Burn, B. J. 1966, MNRAS, 133, 67.
Churchill, C., & Charlton, J., 1999, BAAS, 31, 1451.
Churchill, C. W., Rigby, J. R., Charlton, J. C., Vogt, S. S., 1999, ApJS, 120, 51.
Churchill, C. W., Kacprzak, G. G., & Steidel, C. C., 2005, in IAU Colloq. 199, 'Probing Galaxies through Quasar Absorption Lines, ed. P. R. Williams, C. G. Shu, & B. Menard (Cambridge: Cambridge Univ. Press), 24.
Condon, J. J., Cotton, W. D., Greisen, E. W., et al. 1998, AJ, 115, 1693.
Douglas, J. N., Bash, F. N., Bozyan, F. A., Torrence, G. W., & Wolfe, C. 1996, AJ, 111, 1945.
Farnes, J. S., Gaensler, B. M., Carretti, E., 2014, ApJS, 212, 15.
Gaensler, B. M., Beck, R., & Feretti, L. 2004, New A Rev., 48, 1003.
Gaensler, B. M., Landecker, T. L., Taylor, A. R., & POSSUM Collaboration, 2010, BAAS, 42, 515.
Gregory, P. C., Scott, W. K., Douglas, K., & Condon, J. J. 1996, ApJS, 103, 427.
Hammond, A. M., Robishaw, T., & Gaensler, B. M. 2012, preprint (arXiv:1209.1438v3).
Johnson, V. E., 2013, Proc. Nat. Acad. Sci. 110, 19313.
Jones, T. M., Misawa, T., Charlton, J. C., Mshar, A. C., & Ferland, G. J. 2010, ApJ, 715, 1497.
Joshi, R., & Chand, H., 2013, MNRAS, 434, 3566.
Kacprzak, G. G., Churchill, C. W., Steidel, C. C., & Murphy, M. T., 2008, AJ, 135, 922.
Klein, U., Mack, K.-H., Gregorini, L., & Vigotti, M. 2003, A&A, 406, 579.
Kronberg, P. P., Perry, J. J., 1982, ApJ, 263, 518.
Kronberg, P. P., Perry, J. J., Zukowski, E. L. H., 1990, ApJ, 355, 31.
Kronberg, P. P., Bernet, M. L., Miniati, F., Lilly, S. J., Short, M. B., Higdon, D. M., 2008, ApJ, 676, 70.
Kulsrud, R. M., Zweibel, E. G., 2008, Rep. Prog. Phys., 71, 046901.
Longair, M. S. 2011, High Energy Astrophysics, Cambridge, UK: Cambridge University Press, 2011.
López, E. D., 2006, ApJ, 641, 710.
Mantovani, F., Mack, K.-H., Montenegro-Montes, F. M., Rossetti, A., & Kraus, A. 2009, A&A, 502, 61.
Massardi, M., Burke-Spolaor, S. G., Murphy, T., et al., 2013, MNRAS, 436, 2915.
Mesa, D., Baccigalupi, C., De Zotti, G., et al., 2002, A&A, 396, 463.
Murphy, T., Sadler, E. M., Ekers, R. D., et al. 2010, MNRAS, 402, 2403.
Narayanan, A., Misawa, T., Charlton, J. C., & Kim, T. S., 2007, ApJ, 660, 1093.
O'Dea, C. P., 1988, BAAS, 20, 971.
O'Sullivan, S. P., Gabuzda, D. C., 2009, MNRAS, 393, 429.
O'Sullivan, S. P., Brown, S., Robishaw, T., et al. 2012, MNRAS, 421, 3300.
Oppermann, N., Junklewitz, H., Robbers, G., et al. 2012, A&A, 542, 93.
Oppermann, N., Junklewitz, H., Greiner, M., et al. 2014, A&A, submitted (arXiv:1404.3701).
Oren, A. L., Wolfe, A. M., 1995, ApJ, 445, 624.
Pacholczyk, A. G., & Swihart, T. L., 1967, ApJ, 150, 647.
Pacholczyk, A. G., 1970, 'Radio astrophysics. Nonthermal processes in galactic and extragalactic sources', San Francisco: Freeman, 1970.
Pacholczyk, A. G., & Gregory, S. A., 1973, MNRAS, 161, 31.
Perry, J. J., Watson, A. M., Kronberg, P. P., 1993, ApJ, 406, 407.
Pshirkov, M. S., Tinyakov, P. G., Urban, F. R., 2014, preprint (arXiv:1407.3909).
Rengelink, R. B., Tang, Y., de Bruyn, A. G., et al. 1997, A&AS, 124, 259.
Rigby, J. R., Churchill, C. W., Charlton, J. C., 1998, BAAS, 30, 1248.
Rossetti, A., Dallacasa, D., Fanti, C., Fanti, R., & Mack, K.-H. 2008, A&A, 487, 865.
Saikia, D. J., Salter, C. J., Neff, S. G., Gower, A. C., Sinha, R. P., & Swarup, G., 1987, MNRAS, 228, 203.
Simard-Normandin, M., Kronberg, P. P., & Neidhoefer, J. 1980, A&AS, 40, 319.
Simard-Normandin, M., Kronberg, P. P., & Neidhoefer, J. 1981, A&AS, 43, 19.
Simard-Normandin, M., Kronberg, P. P., & Button, S. 1982, A&AS, 48, 137.
Sokoloff, D. D., Bykov, A. A., Shukurov, A., et al. 1998, MNRAS, 299, 189.
Steidel, C. C., Sargent, W. L. W., 1992, ApJS, 80, 1.
Stil, J. M., Keller, B. W., George, S. J., Taylor, A. R., 2014, ApJ, 787, 99.
Tabara, H., & Inoue, M. 1980, A&AS, 39, 379.
Taylor, A. R., Stil, J. M., & Sunstrum, C. 2009, ApJ, 702, 1230.
Tingay, S. J., Jauncey, D. L., King, E. A., et al. 2003, PASJ, 55, 351.
Tribble, P. C. 1991, MNRAS, 250, 726.
Tripp, T. M., Lu, L., Savage, B. D., 1997, ApJS, 112, 1.
Watson, A. M., Perry, J. J., 1991, MNRAS, 248, 58.
Welter, G. L., Perry, J. J., Kronberg, P. P., 1984, ApJ, 279, 19.
White, R. L., Becker, R. H., Helfand, D. J., Gregg, M. D., 1997, ApJ, 475, 479.
Xu, J., & Han, J. L., 2014a, MNRAS, 442, 3329.
Xu, J., & Han, J. L., 2014b, Research in Astronomy and Astrophysics, 14, 942.
Zavala, R. T., Taylor, G. B., 2003, ApJ, 612, 749.
Zhu, G., & Ménard, B. 2013, ApJ, 770, 130.
Zukowski, E. L. H., Kronberg, P. P., Forkert, T., & Wielebinski, R. 1999, A&AS, 135, 571.

APPENDIX

A. THEORY OF PARTIAL COVERAGE

The potential presence of partial coverage has previously been inferred from polarized spectral energy distributions (SEDs). For some sources, the polarized SEDs have been described by an equation of the form

$$\Pi(\lambda) = \Pi_0 \exp\left(-2\sigma_{\rm RM}^2 \lambda^4\right), \tag{A1}$$

where $\sigma_{\rm RM}$ is the RM dispersion of the Faraday screen within a single beam, λ is the observing wavelength, Π is the fractional polarization, and Π_0 is the fractional polarization at infinite frequency. Such external Faraday depolarization was initially proposed by Burn (1966) – a 'Burn law'. However, while in some sources the polarized fraction can behave similarly to equation A1 at progressively shorter wavelengths, it remains unexpectedly constant out to longer wavelengths (e.g. Rossetti et al. 2008; Mantovani et al. 2009). These SEDs that follow a 'Rossetti–Mantovani law' have been explained by assuming that only a fraction of the source is covered by an inhomogeneous Faraday screen (e.g. Rossetti et al. 2008). In an effort to derive $\sigma_{\rm RM}$ for these sources, Rossetti et al. (2008) made an empirical modification to the Burn law so that

$$\Pi(\lambda) = \Pi_0 \left[f_{\rm c} \exp\left(-2\sigma_{\rm RM}^2 \lambda^4\right) + (1 - f_{\rm c}) \right], \tag{A2}$$

where $f_{\rm c}$ is interpreted as the covered (depolarizing) fraction of the source, with the uncovered fraction $(1 - f_{\rm c})$ retaining a constant polarized fraction, $(1 - f_{\rm c})\Pi_0$, out to arbitrarily long wavelengths. This model has been found to be more successful than the Burn law in reproducing the SED of some sources (e.g. Mantovani et al. 2009; Rossetti et al. 2008; Farnes et al. 2014). As the existence of such partial coverage SED models and the MgII absorption line studies (see Section 1) both imply partial coverage, this has been taken together to imply that there must be a link between partial coverage SEDs and MgII absorption lines (e.g. Bernet et al. 2012, 2013) – with the inference that intervening MgII host galaxies may be responsible for the partial coverage. Nevertheless, while some polarized SEDs show a similar run in the polarized fraction as a function of wavelength as

that predicted by equation A2, due to sample limitations there is currently no direct evidence available in the literature to connect these same sources to the presence of MgII absorption lines.

Attempts to justify partial coverage models have previously been made using equation A2, as this explains the functional form of some polarized SEDs (e.g. Rossetti et al. 2008; Mantovani et al. 2009; Farnes et al. 2014). In addition, Bernet et al. (2012) found that Faraday complexity appears to be more commonly observed in weakly polarized sources, which led to the proposal of a toy model that suggests this is related to enhanced depolarization of different source components due to partial coverage. However, flat-spectrum sources are also known to be intrinsically more weakly polarized than their steep-spectrum counterparts (e.g. Mesa et al. 2002; Stil et al. 2014). It is therefore plausible that such effects could be caused by, for example, epoch-dependent variability between observations, or an increased presence of Faraday complexity in the SEDs of flat-spectrum sources. Such possibilities provide a more simple alternative to invoking a partial coverage model.

Irrespective of the presence of an intervenor, the majority of radio sources are known to undergo depolarization at increasing radio wavelengths due to coverage by an inhomogeneous 'Faraday screen', i.e. a magnetoionic region that is devoid of relativistic particles and that exists somewhere along the line of sight between the observer and the source (e.g. Sokoloff et al. 1998). Here we assume that these Faraday screens are always inhomogeneous and contain a turbulent or systematically varying regular magnetic field, such that the screen causes depolarization, and not just Faraday rotation. Although the location of these screens along the line of sight cannot be trivially determined (e.g. Burn 1966; Tribble 1991; Sokoloff et al. 1998), more recent data suggests that the most significant predictor of the depolarization properties is the total intensity spectral index (Farnes et al. 2014) – suggesting that the Faraday screens are located within the local source environment and that radio opacity effects are important for polarization studies.

Following the conventional partial coverage model, consider the case where an intervening galaxy is known to be present and is believed to be partially covering the background quasar. The model of equation A2 makes the critical assumption that while a fraction of the source is partially covered by an inhomogeneous Faraday screen from an intervenor, the other fraction is completely uncovered – with no covering depolarizing screen whatsoever. How this uncovered portion of the source altogether escapes the effects of Faraday screens, and remains depolarization-free, is not explained. As a typical radio source without an associated intervenor is known to be covered by a depolarizing screen (e.g. Farnes et al. 2014), similarly, portions of a source without an intervening object should also have a similar screen. One could argue that the screen across the uncovered portion of the source is a non-turbulent Faraday screen, that does not depolarize and which only adds additional Faraday rotation, although there are no suitable candidates for such a physical mechanism in this subset of sources. Analogously, equation A2 states that when the covering fraction tends to zero, the polarized fraction will remain constant at all wavelengths. Such a theory is incompatible with the observational evidence, which shows that there is no realistic expectation of detectable polarization at arbitrarily long wavelengths (e.g. Arshakian & Beck 2011). We note that all other depolarization models that are typically available in the literature, such as the Burn law, have all been derived from physical principles (e.g. Farnes et al. 2014).

In order to be physically justified, any partial coverage model must also allow for depolarization in the uncovered fraction of the source, or explain how the uncovered fraction can become immune to the effects of the inhomogeneous Faraday screens that surround a typical radio source. We therefore extend the partial coverage model to include the effect of an inhomogeneous Faraday screen across the uncovered fraction of a source, such that

$$\Pi(\lambda) = \Pi_0 \left[f_\mathrm{c} \exp\left(-2\lambda^4 \left[\sigma^2_\mathrm{interv} + \sigma^2_\mathrm{norm}\right]\right) + (1 - f_\mathrm{c}) \exp\left(-2\sigma^2_\mathrm{norm}\lambda^4\right)\right] , \tag{A3}$$

where σ_norm is the RM dispersion in the absence of an intervenor (whether this dispersion originates locally to the source, in the Galaxy, or elsewhere), and σ_interv is the screen provided by the intervenor and which is allowed to partially cover a fraction, f_c, of the background emitting region, i.e. a quasar or radio galaxy. We make the reasonable assumption that the intervening and normal screens are independent and uncorrelated, such that the combined RM dispersion of the two overlapping screens is given by $\sigma^2_\Sigma = \sigma^2_\mathrm{interv} + \sigma^2_\mathrm{norm}$. We also assume that the background emitting region is optically-thin and that opacity effects are negligible. The functional form of the partial coverage model in equation A3 is advantageous to previous partial coverage models in that it is physically consistent, and when either $f_\mathrm{c} = 0$ or $\sigma_\mathrm{interv} = 0$ rad m^{-2} we retrieve a conventional Burn law. The original partial coverage model in equation A2 is now only a special case, albeit a non-physical one, when $\sigma_\mathrm{norm} = 0$ rad m^{-2}.

This extended partial coverage model has significant implications for our understanding of partial coverage. It can only recreate the observed constant portion of a polarized SED as a special case, when the normal depolarizing screen that covers a fraction $1 - f_\mathrm{c}$ of the source is exactly equal to zero, i.e. $\sigma_\mathrm{norm} = 0$ rad m^{-2}. The polarized SEDs that can occur in this depolarization model are shown in Fig. A1. The SEDs show considerable variation depending on the ratio of $\sigma_\mathrm{interv}/\sigma_\mathrm{norm}$, and exceptionally high-quality observational data would be required to distinguish between these various scenarios. Importantly, for $f_\mathrm{c} > 0$ and low ratios of $\sigma_\mathrm{interv}/\sigma_\mathrm{norm}$, the functional form is indistinguishable from the case where $f_\mathrm{c} = 0$, i.e. a Burn law. Furthermore, even for arbitrarily high ratios of $\sigma_\mathrm{interv}/\sigma_\mathrm{norm}$, the polarized SED will not exhibit the constant polarized tail that is the crucial foundation for a 'partial coverage' model. Consequently, while derivation of σ_RM using equation A2 may suitably mathematically parameterize the rate of decay of polarization as a function of λ, it is unlikely that σ_RM describes the RM dispersion of a physical Faraday screen. There is therefore little reason to think that the equivalent to the RM dispersion that is derived from equation A2 bears any physical relation to the properties of the depolarizing screen across the source.

Although we have shown that SEDs in the form of equation A2 cannot be related to partial coverage, they are still observed (Rossetti et al. 2008; Mantovani et al. 2009). We therefore also propose an alternative model to explain their origin. It has previously been found that flat-spectrum radio sources typically maintain a relatively constant polarized fraction as a function of λ, which has been explained as a consequence of multiple optically-thick emission regions in the quasar core (Farnes et al. 2014) – such sources can maintain an approximately constant polarized fraction as a function of wavelength (e.g. Pacholczyk & Swihart 1967; Pacholczyk & Gregory 1973). As an extension of this, the polarized SED of an unresolved, compact source

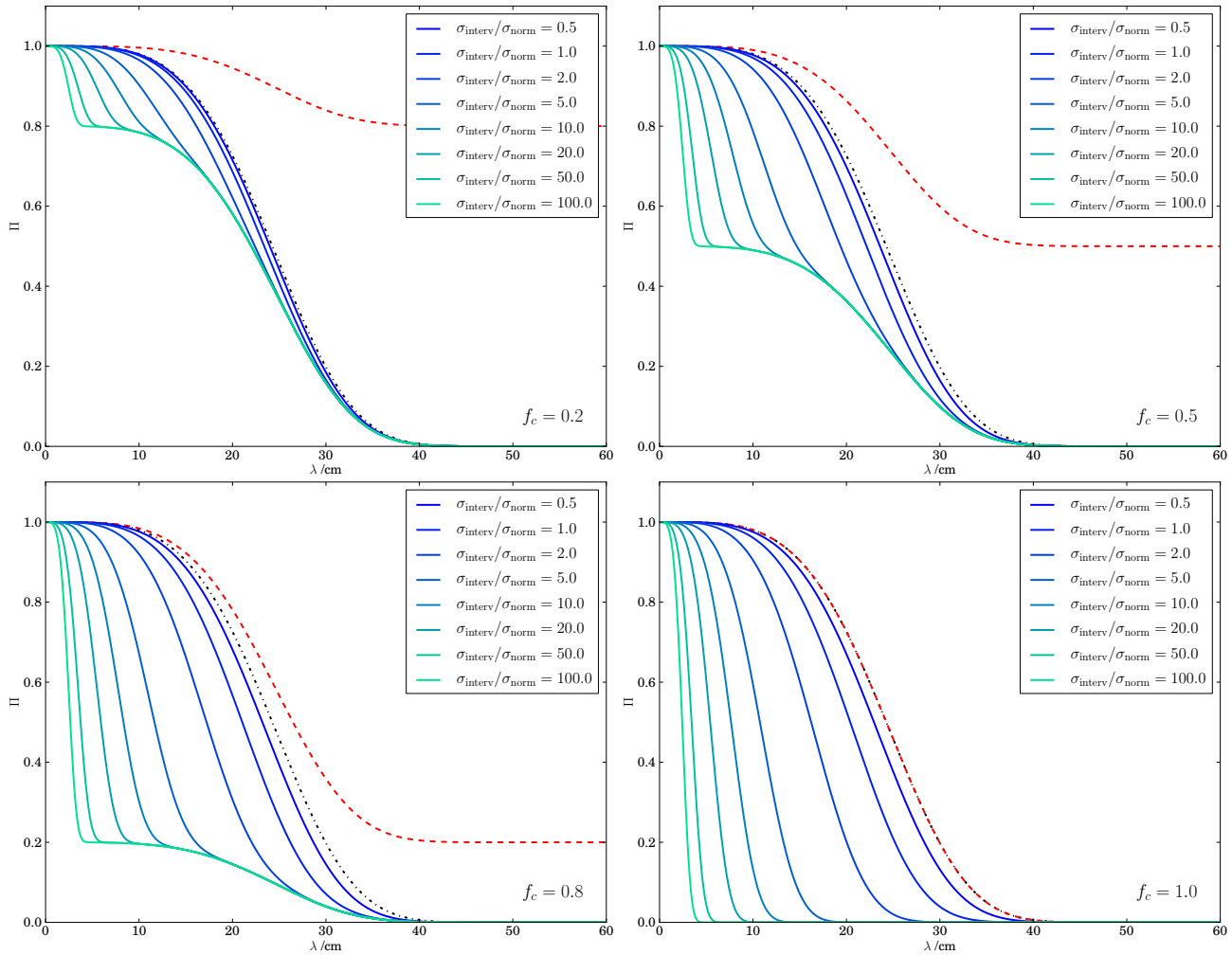

Figure A1. A visualisation of polarized SEDs that can arise from partial coverage models, shown as plots of the degree of polarization as a function of wavelength. Such SEDs may arise whenever there are two independent Faraday screens covering different fractions of a source as detailed by equation A3. Plots are shown for a covering fraction of f_c =0.2 (top left), 0.5 (top right), 0.8 (bottom left), and 1.0 (bottom right). In all plots, the special depolarizing case where there is only an intervening screen across the source, $\sigma_{\rm norm}$ = 0 rad m^{-2} and $\sigma_{\rm interv}$ = 10 rad m^{-2}, is shown as a red dashed line. The case where there is no depolarizing intervening screen, $\sigma_{\rm norm}$ = 10 rad m^{-2} and $\sigma_{\rm interv}$ = 0 rad m^{-2}, is shown as a black dotted line. The depolarization when both a normal and intervening screen are present is shown by the solid coloured lines (dark to light blue), for several differing contributions from the intervening screen across the covered fraction of the source; in all of these cases the normal screen remains constant. The ratio of the intervening and normal screens, $\sigma_{\rm interv}/\sigma_{\rm norm}$, is shown in the legend with darker blue indicating a lower ratio. Even when an infinitesimally small normal screen is present, it is not possible to obtain the constant polarized tail that is typically considered characteristic of 'partial coverage' models.

may be the superposition of two components: (i) a strongly polarized and strongly depolarizing optically-thin jets/lobes (with $\alpha \approx -0.7$), and (ii) a weakly polarized and weakly depolarizing optically-thick core (with $\alpha \approx 0.0$). Such an SED would have a functional form similar to that presented in the original partial coverage model shown in equation A2, as it would be dominated by the depolarizing jets/lobes at high frequencies and the weakly depolarizing core at low frequencies. Note that this is the inverse of the typical situation in total intensity, where the steep-spectrum jets/lobes dominate the emission at low frequencies. Such a model is falsifiable, as in all cases the approximately constant polarized tail that extends to low frequencies must have a polarized fraction $\leq 10\%$, which is the maximum degree of polarization for an optically-thick region (e.g. Pacholczyk 1970). This is consistent with the catalog of Farnes et al. (2014), which finds a maximum value for the polarized tail of 5.1% from their sample of sources that are classified using a partial coverage SED.

However, if correct, this leads to complications for the typical physical understanding of a polarized fraction (which is the ratio of the polarized and total intensity components). In unresolved sources with an SED of 'partial coverage' form, our measurements are biased towards the brightest *polarized* intensity within the resolution element seen in projection on the sky. Meanwhile, the brightest *total* intensity for the same source may not correspond to the same emitting region. As the peak polarized and total intensity both sample different regions of the source, this leads to the possibility that a polarized fraction, Π, may not be at all related to the degree of magnetic field ordering in these unresolved sources. Consequently, at a given frequency a source may be core-dominated in Stokes *I* and lobe-dominated in *P*, or vice-versa. High resolution and broadband observations of lines of sight with known intervening objects will be necessary to test our predictions.

We therefore highlight how the partial coverage model of equation A2 is both incompatible with observational evidence, and is also empirical rather than physical – unlike other depolarization laws (e.g. Farnes et al. 2014). We have adjusted this mathematical

model so that it is physically accurate, thereby including the more realistic case where a Faraday screen other than the one provided by the intervenor is also present. In these cases, depolarization from partial coverage can be indistinguishable from a Burn law (see equation A1) at all wavelengths, and never has a constant polarized tail even for extreme ratios of $\sigma_{\rm interv}/\sigma_{\rm norm}$.

B. MAIN SAMPLE DETAILS

Table B1
Details of the main sample, listed in order of NVSS Right Ascension. Sources that are used in the 'flat' or 'steep' spectrum subsamples are indicated by 'F' or 'S' respectively. All errors are the one sigma uncertainties. The listed redshifts are for the polarized background radio sources.

#	NVSS R.A. J2000 (°)	NVSS Dec. J2000 (°)	α	$\Delta\alpha$	χ^2	Flat/Steep Sub-Sample	$N_{\rm MgII}$	RM (rad m^{-2})	ΔRM (rad m^{-2})	Π (%)	$\Delta\Pi$ (%)	β	$\Delta\beta$	z	Δz
1	00h03m45.18s	-11d08m20.6	-1.08	0.18	—	S	0	-8.2	9.0	2.0	0.15	—	—	1.5666	0.0003
2	00h10m18.25s	+14d33m36.7	-1.0	0.2	0.186	S	2	-25.6	11.0	2.77	0.18	—	—	0.90107	0.00027
3	00h13m40.31s	+14d57m32.8	—	—	—	—	0	-19.3	19.0	8.5	0.8	—	—	0.8241	0.00014
4	00h32m59.23s	-00d13m18.2	—	—	—	—	1	-14.9	13.0	2.2	0.19	—	—	1.5	0.0
5	00h35m52.91s	-09d11m50.4	—	—	—	—	0	4.2	12.0	5.8	0.4	—	—	1.0021	0.0005
6	00h35m55.49s	+15d53m16.7	-0.88	0.18	0.339	S	0	-33.7	9.0	1.51	0.13	—	—	1.16279	0.00019
7	00h37m58.31s	+24d07m11.6	-0.64	0.05	0.198	—	0	33.4	2.5	2.4	0.13	-1.15	0.25	0.0	9e-05
8	00h43m23.62s	-00d15m51.1	-1.12	0.18	—	S	0	16.7	10.0	4.22	0.25	—	—	2.7929	0.0014
9	00h50m26.76s	+00d31m56.6	—	—	—	—	0	-20.6	16.0	5.5	0.5	—	—	1.2108	0.0003
10	00h59m05.53s	+00d06m51.5	-0.49	0.03	0.094	—	0	-10.1	0.8	3.91	0.15	-1.1	0.24	0.0	4e-05
11	01h05m35.99s	+15d12m59.2	-1.0	0.2	0.000	S	0	-35.1	14.0	4.0	0.3	—	—	1.02393	0.00016
12	01h13m54.57s	+13d24m52.8	-0.41	0.08	0.037	—	0	-5.1	5.0	6.43	0.25	—	—	0.0	8e-05
13	01h18m34.61s	-08d54m40.2	—	—	—	—	0	-28.1	13.0	3.6	0.3	—	—	1.3218	0.0005
14	01h25m17.15s	-00d18m31.1	-0.67	0.13	2.621	—	1	18.8	11.0	1.11	0.12	—	—	2.27556	0.00013
15	01h29m55.32s	+14d46m48.3	-0.27	0.05	0.272	F	0	-16.0	2.9	2.87	0.15	—	—	1.6287	0.0004
16	01h48m47.57s	-08d19m37.3	—	—	—	—	1	-20.5	14.0	7.9	0.6	—	—	1.6806	0.0003
17	01h51m32.29s	+12d43m53.7	-0.78	0.16	0.578	S	0	-10.4	9.0	5.37	0.29	—	—	1.4083	0.0015
18	01h58m56.28s	+13d07m02.3	-0.21	0.04	0.087	F	0	-0.6	6.0	5.56	0.24	—	—	1.8917	0.0004
19	02h07m03.34s	-08d54m44.1	-0.83	0.18	—	S	0	-47.1	11.0	2.8	0.2	—	—	1.0699	0.0004
20	02h10m00.18s	-10d03m53.9	—	—	—	—	1	15.8	17.0	1.52	0.16	—	—	1.9741	0.0009
21	02h11m00.01s	+21d10m54.1	-0.65	0.13	0.208	—	0	-37.5	6.0	8.7	0.4	—	—	1.3479	0.0003
22	02h16m16.52s	+05d30m56.7	-0.31	0.06	0.184	—	0	-23.8	8.0	7.3	0.4	—	—	1.36176	0.00016
23	02h25m08.08s	-00d35m31.8	-0.77	0.15	0.225	S	0	10.6	1.0	6.53	0.25	-0.03	0.03	0.7	0.0
24	02h28m07.66s	-01d15m41.7	-0.86	0.18	—	S	0	-1.8	4.0	4.11	0.19	—	—	2.04593	0.00023
25	02h45m34.15s	+01d08m17.2	-1.17	0.23	0.063	S	1	0.3	9.0	3.4	0.21	—	—	1.5284	0.0006
26	02h53m21.07s	+00d06m01.6	—	—	—	—	0	33.6	15.0	3.4	0.26	—	—	1.3	0.0
27	03h03m13.05s	-00d14m59.8	-0.89	0.18	3.043	S	0	11.4	4.0	1.54	0.11	-0.7	0.6	0.0	6e-05
28	03h04m59.24s	+00d02m33.6	—	—	—	—	0	11.6	11.0	5.3	0.3	—	—	0.0	4e-05
29	03h52m32.04s	-07d11m04.4	-1.28	0.06	—	S	0	18.1	0.3	10.9	0.4	-0.02	0.09	0.962	0.00029
30	07h36m31.90s	+45d41m25.8	-0.61	0.17	—	—	0	-15.3	14.0	9.1	0.7	—	—	0.95575	0.00016
31	07h41m55.60s	+42d08m17.6	-0.65	0.13	0.097	—	0	-0.9	8.0	5.02	0.26	—	—	2.2298	0.00028
32	07h49m10.31s	+47d48m04.9	-0.27	0.05	2.231	F	0	-8.9	12.0	7.6	0.5	—	—	1.56997	0.00026
33	07h51m45.18s	+41d15m35.4	-0.35	0.07	0.538	—	0	-3.4	5.0	4.72	0.21	—	—	0.0	8e-05
34	07h51m53.69s	+33d13m19.8	-0.17	0.03	1.560	F	0	35.6	11.0	1.04	0.12	—	—	1.9352	0.0005
35	07h55m03.34s	+42d31m42.7	-0.92	0.18	0.781	S	0	35.1	10.0	3.94	0.26	—	—	1.8561	0.0004
36	07h57m00.68s	+42d48m13.2	-0.86	0.17	—	S	0	4.5	12.0	7.1	0.5	—	—	1.1737	0.0014
37	07h59m28.29s	+30d10m29.1	-0.29	0.06	0.043	F	1	20.0	17.0	2.65	0.23	—	—	0.99992	0.00021
38	08h05m55.73s	+34d41m32.5	-0.82	0.16	0.514	S	1	21.6	12.0	6.1	0.4	—	—	1.7376	0.0004
39	08h06m42.24s	+19d58m12.6	-0.81	0.16	0.191	S	0	41.7	8.0	6.5	0.4	—	—	1.1997	0.0014
40	08h07m00.79s	+51d17m37.1	0.067	0.013	0.039	F	0	-8.4	15.0	1.7	0.17	—	—	1.13781	0.00022
41	08h08m56.69s	+40d52m45.1	0.111	0.022	0.589	F	0	3.8	9.0	1.4	0.12	0.7	0.8	1.41859	0.00019
42	08h09m21.14s	+20d15m38.8	-0.8	0.16	0.029	S	1	-16.3	11.0	7.7	0.5	—	—	1.1279	0.0004
43	08h10m02.08s	+26d03m38.3	-0.5	0.1	0.000	—	0	23.8	15.0	2.86	0.25	—	—	2.2647	0.0016
44	08h11m00.60s	+57d14m11.5	-0.24	0.05	3.358	F	0	-4.3	3.0	7.27	0.27	—	—	0.0	3e-05
45	08h11m00.85s	+21d41m36.9	-0.75	0.15	0.086	S	0	37.4	5.0	5.99	0.25	—	—	1.52379	0.00017
46	08h12m47.75s	+25d22m41.8	0.26	0.05	1.622	F	1	-7.5	17.0	5.2	0.4	—	—	1.8079	0.0004
47	08h13m03.83s	+25d42m11.1	-0.033	0.007	0.307	F	0	60.7	9.0	1.83	0.13	—	—	2.0203	0.0004
48	08h13m19.35s	+50d12m40.9	-0.82	0.16	1.955	S	1	-3.5	5.0	4.64	0.19	—	—	0.571	0.0015
49	08h14m36.30s	+28d33m38.0	-0.64	0.27	—	—	0	28.9	15.0	6.2	0.5	—	—	1.6248	0.0004
50	08h15m34.24s	+33d05m29.3	-0.88	0.18	0.323	S	0	2.6	8.0	2.02	0.14	—	—	2.4207	0.0002
51	08h17m10.64s	+23d52m23.2	-0.22	0.04	0.000	F	2	-23.0	17.0	1.71	0.18	—	—	1.7309	0.0005
52	08h17m35.10s	+22d37m11.9	-0.75	0.15	0.002	S	1	40.7	0.9	6.16	0.24	-0.8	0.4	0.98022	0.00014
53	08h19m16.61s	+26d42m01.3	-0.62	0.12	0.032	—	0	8.6	13.0	1.68	0.15	—	—	0.5258	0.00019
54	08h21m16.61s	+48d45m40.7	-0.58	0.12	1.921	—	0	6.4	14.0	5.6	0.4	—	—	1.5733	0.0003
55	08h22m57.50s	+40d41m49.8	-0.21	0.04	0.238	F	0	0.8	4.0	4.8	0.19	—	—	0.8655	0.00019
56	08h23m25.30s	+44d58m51.6	-0.83	0.17	0.255	S	0	-62.5	13.0	1.31	0.13	—	—	0.0	5e-05
57	08h24m47.27s	+55d52m42.6	-0.16	0.03	0.043	F	0	-27.7	1.3	3.64	0.15	—	—	1.4191	0.0003
58	08h25m17.22s	+44d36m31.6	-0.96	0.03	0.412	S	1	2.4	2.1	3.73	0.17	—	—	0.0	8e-05
59	08h25m21.91s	+45d37m04.8	-0.69	0.14	0.582	—	0	-7.6	15.0	5.2	0.4	—	—	1.9088	0.0005
60	08h27m06.60s	+10d52m22.9	-0.16	0.03	0.282	F	3	19.1	5.0	6.38	0.25	—	—	2.28063	0.00021
61	08h30m03.31s	+19d10m39.1	-0.88	0.18	0.007	S	0	11.7	8.0	1.6	0.13	—	—	0.7	0.0
62	08h31m10.00s	+37d42m09.9	-0.7	0.04	1.806	S	0	8.8	2.9	1.1	0.11	-0.05	0.14	0.0	8e-05
63	08h31m56.54s	+13d52m18.1	—	—	—	—	0	23.1	6.0	3.7	0.2	—	—	0.0	4e-05
64	08h31m59.12s	+13d53m15.4	—	—	—	—	0	26.0	2.3	10.7	0.4	—	—	0.0	4e-05
65	08h32m25.62s	+27d22m56.4	-0.88	0.18	1.604	S	0	20.6	17.0	2.92	0.25	—	—	0.0	5e-05
66	08h32m28.08s	+18d37m44.0	-1.2	0.2	—	S	0	15.8	2.8	10.4	0.4	—	—	1.3915	0.0004
67	08h32m29.70s	+12d52m18.5	-0.6	0.2	—	—	0	27.0	4.0	8.3	0.3	—	—	1.3074	0.0007
68	08h32m49.42s	+15d54m08.9	-0.058	0.012	0.163	F	1	14.3	16.0	1.27	0.14	—	—	2.42471	0.00022
69	08h33m14.43s	+11d23m36.2	-0.26	0.05	0.810	F	2	52.8	10.0	1.49	0.13	—	—	2.9789	0.00014
70	08h33m22.50s	+09d59m41.4	-0.19	0.04	0.263	F	0	6.3	12.0	3.84	0.27	—	—	3.7133	0.0004
71	08h37m40.25s	+24d54m23.0	-0.076	0.015	0.351	F	0	8.0	4.0	2.99	0.14	—	—	1.12531	0.00012
72	08h38m23.12s	+12d29m54.3	-0.96	0.19	1.424	S	2	30.8	9.0	3.75	0.24	—	—	1.6263	0.00028
73	08h39m07.10s	+19d21m57.1	-0.78	0.16	0.803	S	1	13.1	2.5	4.91	0.21	-0.33	0.28	0.0	8e-05
74	08h39m56.52s	+42d27m55.9	-0.43	0.07	2.793	—	0	-5.2	6.0	1.85	0.13	-0.47	0.09	0.6004	0.0002
75	08h40m47.70s	+13d12m23.9	-0.59	0.12	0.007	—	0	25.6	1.2	2.14	0.12	-0.58	0.17	0.0	7e-05
76	08h42m05.09s	+18d35m41.8	-0.26	0.05	0.082	F	1	38.2	1.7	3.13	0.14	—	—	1.27406	0.00018
77	08h43m44.82s	+58d24m13.0	-0.57	0.11	3.160	—	0	-13.9	2.3	9.0	0.3	—	—	1.4829	0.0008
78	08h44m17.00s	+13d40m39.3	-0.31	0.06	1.669	—	2	-10.7	16.0	2.1	0.2	—	—	1.7373	0.0003
79	08h45m38.64s	+58d52m33.1	-0.96	0.19	0.026	S	0	-25.0	12.0	1.66	0.15	—	—	2.15418	0.00029
80	08h45m47.17s	+13d28m58.1	-0.61	0.12	0.132	—	1	10.6	3.0	4.49	0.18	-0.71	0.14	1.88348	0.00011
81	08h47m34.35s	+46d09m27.6	-0.127	0.025	0.402	F	0	-9.8	10.0	4.0	0.23	—	—	1.21647	0.00029

Table B2
Continued from Table B1.

#	NVSS R.A. J2000 (°)	NVSS Dec. J2000 (°)	α	$\Delta\alpha$	χ^2	Flat/Steep Sub-Sample	$N_{\rm MgII}$	RM (rad m^{-2})	ΔRM (rad m^{-2})	Π (%)	$\Delta\Pi$ (%)	β	$\Delta\beta$	z	Δz
82	08h48m56.88s	+08d01m27.1	-0.84	0.17	0.061	S	0	67.0	10.0	2.76	0.18	—	—	0.9577	0.00012
83	08h50m51.82s	+15d22m15.3	-0.74	0.15	0.601	S	1	49.9	1.1	12.0	0.4	—	—	2.0144	0.0003
84	08h51m28.95s	+60d03m20.2	-0.71	0.14	0.410	S	0	-14.3	9.0	5.9	0.3	—	—	0.54264	0.00019
85	08h52m00.25s	+02d29m34.1	-1.2	0.3	—	S	0	-8.2	7.0	5.8	0.29	—	—	1.1767	0.0022
86	08h52m05.20s	+28d33m59.7	0.36	0.07	2.910	F	0	-0.4	6.0	4.48	0.21	—	—	1.2819	0.0006
87	08h53m02.75s	+20d04m21.6	-0.57	0.11	0.608	—	0	23.8	10.0	5.25	0.29	—	—	1.9201	0.0005
88	08h54m11.17s	-00d19m29.9	-0.78	0.18	—	S	0	38.4	4.0	3.11	0.15	—	—	1.3893	0.0006
89	08h54m35.08s	+07d20m24.3	0.68	0.14	0.248	F	0	83.0	8.0	5.71	0.28	—	—	0.65507	0.00019
90	08h56m57.21s	+21d11m44.3	-0.077	0.015	0.240	F	1	34.9	4.0	3.34	0.15	—	—	2.1001	0.0006
91	08h58m52.44s	+16d51m24.5	-0.79	0.16	0.066	S	1	33.1	2.8	3.86	0.16	1.15	0.23	1.4	0.0
92	09h00m14.01s	+02d47m18.0	-0.74	0.15	0.010	S	0	15.5	5.0	8.2	0.3	—	—	1.188	0.0007
93	09h03m32.94s	+27d19m28.2	-0.62	0.12	0.128	—	1	10.1	7.0	4.57	0.23	—	—	1.722	0.003
94	09h05m04.06s	+27d48m17.2	-0.087	0.017	0.069	F	0	9.9	11.0	3.16	0.19	—	—	1.4855	0.0007
95	09h05m27.49s	+48d50m49.0	-0.17	0.03	1.747	F	0	-34.5	5.0	2.02	0.13	—	—	2.68606	0.00019
96	09h06m02.53s	+41d16m29.9	-0.85	0.17	0.759	S	0	20.8	2.4	3.44	0.17	—	—	0.0	6e-05
97	09h06m31.88s	+16d46m13.0	-1.13	0.23	0.222	S	0	22.3	4.0	1.34	0.11	-1.04	0.19	0.4121	0.0003
98	09h09m10.14s	+01d21m35.6	0.17	0.03	0.569	F	1	-18.0	1.3	6.22	0.22	0.15	0.03	1.02321	0.00016
99	09h10m54.91s	+56d43m44.2	-0.41	0.08	0.020	—	0	-23.3	15.0	9.2	0.7	—	—	1.3976	0.0005
100	09h10m55.22s	+25d39m21.8	-0.72	0.14	0.008	S	1	-36.1	9.0	3.66	0.22	—	—	2.746	0.0004
101	09h11m33.51s	+19d58m14.3	-0.129	0.026	0.001	F	1	18.2	5.0	3.5	0.16	—	—	1.636	0.0005
102	09h12m04.64s	+08d37m48.4	-0.08	0.016	0.031	F	0	20.2	13.0	3.3	0.22	—	—	1.53725	0.00016
103	09h13m53.23s	+44d02m56.3	-0.014	0.0028	0.004	F	2	30.3	7.0	3.88	0.19	—	—	1.1781	0.0002
104	09h14m37.96s	+02d45m59.8	0.5	0.1	1.920	F	0	-9.8	4.0	3.46	0.16	—	—	0.0	4e-05
105	09h15m08.78s	+20d56m08.4	-0.4	0.08	0.013	—	2	21.7	8.0	2.26	0.15	—	—	1.7764	0.0004
106	09h16m48.93s	+38d54m28.5	-0.28	0.08	3.559	F	1	3.2	5.0	1.2	0.11	—	—	1.2664	0.0006
107	09h17m08.35s	+61d49m31.6	-0.47	0.09	2.510	—	0	-10.8	4.0	6.82	0.27	—	—	1.4456	0.0004
108	09h17m34.78s	+50d16m37.8	-0.68	0.14	2.313	—	0	-28.1	12.0	3.85	0.27	—	—	0.63244	0.00014
109	09h18m58.75s	+24d52m45.4	-0.81	0.16	1.708	S	0	35.6	14.0	4.2	0.3	—	—	0.79749	0.00017
110	09h19m07.56s	+21d25m54.2	-0.34	0.07	0.058	—	2	-3.1	13.0	1.94	0.17	—	—	1.39253	0.00026
111	09h19m14.82s	+22d05m20.0	-0.45	0.09	0.112	—	0	-1.7	7.0	5.48	0.27	—	—	1.5486	0.0003
112	09h19m21.76s	+50d48m55.5	-0.57	0.11	0.169	—	1	-12.4	17.0	9.6	0.8	—	—	0.0	9e-05
113	09h19m51.11s	+32d55m11.2	-0.86	0.17	1.963	S	0	13.3	16.0	3.9	0.3	—	—	1.1	0.0
114	09h20m35.77s	+00d23m30.3	-0.4	0.08	3.950	—	0	1.1	9.0	4.66	0.29	—	—	2.48562	0.00025
115	09h20m42.36s	+29d16m18.5	-1.12	0.22	0.517	S	0	20.2	12.0	5.4	0.3	—	—	1.916	0.0009
116	09h20m58.48s	+44d41m53.7	0.024	0.005	0.158	F	2	-8.4	4.0	1.64	0.12	—	—	2.18708	0.00017
117	09h21m24.15s	+01d38m34.2	-0.38	0.08	0.006	—	0	-1.3	15.0	2.75	0.22	—	—	1.6596	0.0022
118	09h21m31.35s	+13d50m48.3	-0.119	0.024	0.343	F	1	72.4	15.0	1.16	0.13	—	—	0.0	6e-05
119	09h21m57.74s	+66d04m38.0	-0.23	0.05	0.002	F	2	31.1	15.0	1.97	0.17	—	—	1.64411	0.00023
120	09h23m03.83s	+34d14m53.6	-0.96	0.19	0.510	S	0	-7.0	9.0	3.49	0.19	—	—	1.1128	0.0004
121	09h23m07.36s	+30d59m26.3	-1.0	0.2	2.057	S	0	1.0	8.0	2.45	0.16	-1.2	2.7	0.0	2.5e-05
122	09h26m07.98s	+07d45m26.8	-1.0	0.2	0.117	S	0	45.9	14.0	2.25	0.19	—	—	0.0	1.7e-05
123	09h29m15.52s	+25d36m58.0	-0.3	0.06	1.159	F	0	20.8	5.0	5.83	0.25	—	—	0.0	3e-05
124	09h30m33.45s	+36d01m23.6	-0.96	0.19	2.012	S	0	42.7	1.8	1.89	0.12	-5.7	1.1	1.1561	0.00017
125	09h30m35.14s	+46d44m08.8	-0.47	0.09	0.137	—	1	4.6	2.5	5.85	0.21	—	—	2.0341	0.0004
126	09h30m52.24s	+00d34m58.6	0.16	0.03	1.080	F	0	7.7	7.0	3.24	0.17	—	—	1.7696	0.0004
127	09h31m12.08s	+36d47m49.9	—	—	—	—	0	19.3	4.0	8.8	0.4	—	—	1.395	0.0005
128	09h31m14.78s	+36d47m43.3	—	—	—	—	0	13.1	9.0	6.8	0.4	—	—	1.395	0.0005
129	09h31m32.05s	+47d51m42.0	-0.59	0.12	0.162	—	0	-36.3	10.0	1.46	0.13	—	—	1.1831	0.0005
130	09h39m13.65s	+16d56m25.7	-0.26	0.05	1.456	F	0	8.5	9.0	6.6	0.3	—	—	0.0	9e-05
131	09h39m49.66s	+41d41m53.9	-0.0071	0.0014	0.156	F	1	-16.7	13.0	2.0	0.17	—	—	1.2229	0.0004
132	09h41m04.18s	+38d53m49.8	-0.92	0.04	2.428	S	0	5.4	1.4	8.8	0.3	-0.22	0.06	0.0	5e-05
133	09h44m42.33s	+25d54m43.6	-0.74	0.15	0.005	S	2	-13.9	4.0	2.18	0.13	—	—	2.90439	0.00026
134	09h45m44.52s	+44d54m22.1	-0.49	0.27	—	—	0	13.9	18.0	6.1	0.6	—	—	1.1767	0.0011
135	09h45m49.86s	+12d05m31.4	-0.59	0.12	0.532	—	0	-3.6	2.3	5.26	0.22	—	—	0.96521	0.00017
136	09h45m55.96s	+60d12m37.0	-0.33	0.07	2.155	—	0	7.2	13.0	4.03	0.28	—	—	2.5202	0.00018
137	09h46m35.06s	+10d17m06.6	-0.23	0.05	0.370	F	0	-13.3	8.0	1.69	0.13	—	—	1.0034	0.0003
138	09h47m35.40s	+58d30m48.7	-0.63	0.13	3.725	—	1	0.5	11.0	3.4	0.21	—	—	0.93538	0.00018
139	09h48m55.36s	+40d39m44.8	-0.08	0.11	2.869	F	0	3.0	0.8	6.01	0.21	0.66	0.13	1.24837	0.00018
140	09h48m55.37s	+07d28m03.8	—	—	—	—	0	34.7	10.0	2.21	0.17	—	—	1.1669	0.0006
141	09h48m58.51s	+07d27m28.0	—	—	—	—	0	4.4	7.0	10.3	0.5	—	—	1.1669	0.0006
142	09h49m39.78s	+17d52m48.7	-0.23	0.05	0.033	F	0	-4.4	14.0	7.3	0.5	—	—	0.6935	0.0003
143	09h52m26.53s	+36d06m07.2	-0.5	0.1	0.942	—	2	37.9	16.0	2.83	0.24	—	—	2.0602	0.0004
144	09h52m46.17s	+00d00m19.4	—	—	—	—	0	-16.8	5.0	2.18	0.13	—	—	1.06269	0.00026
145	09h53m59.22s	+17d20m57.0	0.45	0.09	1.166	F	0	18.5	13.0	3.29	0.25	—	—	0.7123	0.0001
146	09h54m14.80s	+61d04m53.8	-0.76	0.15	0.500	S	0	-20.8	10.0	7.9	0.4	—	—	2.6185	0.0004
147	09h54m56.81s	+17d43m31.5	-0.24	0.05	0.020	F	0	-5.5	1.0	4.42	0.17	-1.9	0.4	1.47551	0.00021
148	09h55m55.50s	+06d16m44.1	-0.76	0.15	1.015	S	0	12.6	4.0	8.5	0.3	—	—	1.27919	0.00021
149	09h56m49.88s	+25d15m15.9	0.05	0.13	0.986	F	0	52.1	6.0	0.79	0.11	-0.45	0.21	0.0	9e-05
150	09h57m38.18s	+55d22m57.4	-0.31	0.06	0.390	—	0	13.5	1.3	1.9	0.12	-0.47	0.16	0.90077	0.00019
151	09h58m00.89s	+26d40m11.7	-0.3	0.06	0.938	—	0	15.4	12.0	3.26	0.23	—	—	0.7038	0.0001
152	09h58m02.09s	+44d06m07.3	-0.94	0.19	0.687	S	0	20.7	2.4	9.7	0.4	—	—	2.2	0.0
153	09h58m10.41s	+26d49m30.7	-0.87	0.17	0.109	S	0	44.1	13.0	4.01	0.29	—	—	1.5018	0.0005
154	09h58m19.70s	+47d25m07.0	0.35	0.07	1.627	F	2	22.1	4.0	2.48	0.13	—	—	1.88489	0.00022
155	09h59m43.92s	+41d09m00.6	-0.55	0.11	0.526	—	0	-96.3	12.0	9.5	0.6	—	—	1.1159	0.0023
156	10h00m07.49s	+27d52m48.7	-0.65	0.13	0.060	—	0	9.1	11.0	5.0	0.3	—	—	0.55385	0.00015
157	10h00m21.95s	+22d33m18.2	-0.9	0.18	0.109	S	0	25.3	2.3	2.97	0.14	—	—	0.41873	0.00014
158	10h03m50.81s	+52d53m50.3	-0.81	0.16	0.294	S	0	3.6	8.0	7.1	0.4	—	—	1.3353	0.0015
159	10h03m57.63s	+32d44m03.7	-0.29	0.06	3.545	F	0	17.9	2.2	6.95	0.27	—	—	1.6858	0.0004
160	10h04m45.63s	+22d24m54.3	—	—	—	—	0	14.2	6.0	3.49	0.18	—	—	0.98011	0.00012
161	10h04m45.82s	+22d25m52.5	—	—	—	—	0	26.0	11.0	1.9	0.15	—	—	0.98011	0.00012
162	10h06m07.69s	+32d36m27.7	-0.57	0.11	0.058	—	0	-15.5	5.0	6.57	0.29	—	—	1.02578	0.00013

Table B3
Continued from Table B1.

#	NVSS R.A. J2000 (°)	NVSS Dec. J2000 (°)	α	$\Delta\alpha$	χ^2	Flat/Steep Sub-Sample	$N_{\rm MgII}$	RM (rad m^{-2})	ΔRM (rad m^{-2})	Π (%)	$\Delta\Pi$ (%)	β	$\Delta\beta$	z	Δz
163	10h07m18.06s	+22d51m27.5	-0.64	0.13	0.002	—	1	12.2	10.0	9.8	0.6	—	—	2.3061	0.0005
164	10h07m41.51s	+13d56m29.3	-0.085	0.017	0.001	F	0	11.9	2.3	2.85	0.14	—	—	2.71533	0.00018
165	10h08m41.56s	+36d23m22.7	-0.61	0.12	1.204	—	1	26.9	11.0	8.7	0.5	—	—	3.1255	0.0008
166	10h09m43.05s	+05d29m48.5	-0.92	0.18	2.508	S	1	-18.8	14.0	4.5	0.3	—	—	0.94257	0.00014
167	10h10m27.29s	+41d32m21.7	—	—	—	—	0	-2.3	0.7	5.61	0.24	—	—	0.0	2.8e-05
168	10h10m27.63s	+41d32m36.6	—	—	—	—	0	0.7	0.9	4.85	0.19	—	—	0.0	2.8e-05
169	10h11m00.31s	+32d57m18.4	-0.9	0.18	1.187	S	1	-7.4	17.0	3.8	0.3	—	—	0.90034	0.00018
170	10h11m35.26s	+00d57m47.1	-0.97	0.19	2.139	S	0	-1.2	13.0	3.12	0.24	—	—	1.0717	0.0009
171	10h12m54.58s	+61d36m36.5	-0.73	0.15	0.411	S	1	-24.3	8.0	4.93	0.28	—	—	2.0534	0.0015
172	10h13m29.97s	+49d18m40.8	-0.33	0.07	1.193	—	0	7.0	15.0	1.37	0.14	—	—	2.1973	0.00025
173	10h14m35.86s	+27d49m03.2	-0.8	0.16	0.736	S	1	24.8	3.0	3.57	0.17	—	—	0.9	0.0
174	10h14m45.47s	+31d34m30.7	-0.66	0.13	0.736	—	2	39.7	13.0	6.9	0.5	—	—	1.3619	0.0004
175	10h14m47.05s	+23d01m12.7	0.0083	0.0017	0.042	F	0	25.9	3.0	1.7	0.12	0.0	0.9	0.0	2.7e-05
176	10h15m28.14s	+19d44m47.3	—	—	—	—	1	-1.2	14.0	8.5	0.6	—	—	1.7924	0.0004
177	10h16m44.40s	+20d37m46.5	0.24	0.05	0.042	F	1	-24.1	10.0	1.19	0.12	—	—	3.11406	0.00014
178	10h17m49.77s	+27d32m07.7	-0.78	0.16	0.116	S	0	31.3	0.9	5.23	0.19	—	—	0.4678	0.0013
179	10h18m11.01s	+35d42m40.7	0.073	0.015	1.439	F	1	6.4	3.0	2.88	0.14	—	—	1.22803	0.00011
180	10h20m07.76s	+10d40m03.5	-0.88	0.18	1.550	S	3	1.4	4.0	2.97	0.14	—	—	3.1672	0.0008
181	10h21m12.84s	+44d35m00.9	-0.81	0.16	—	S	2	17.3	15.0	5.6	0.4	—	—	1.7579	0.0005
182	10h23m10.56s	+47d51m46.2	-0.82	0.16	0.142	S	0	-0.7	6.0	1.93	0.13	—	—	0.0	3e-05
183	10h24m44.82s	+19d12m20.7	0.083	0.017	0.047	F	1	25.6	6.0	1.71	0.12	0.13	0.24	0.0	7e-05
184	10h26m31.96s	+06d27m32.7	-0.86	0.17	1.024	S	0	29.7	4.0	1.6	0.12	-0.05	0.25	1.7093	0.0023
185	10h28m21.29s	+24d01m22.0	0.035	0.007	0.330	F	0	23.8	14.0	1.27	0.14	—	—	1.87418	0.00027
186	10h28m37.04s	-01d00m27.5	-0.33	0.08	—	—	2	-3.4	13.0	3.04	0.23	—	—	1.5305	0.0004
187	10h29m39.82s	+22d51m37.1	-0.84	0.17	0.006	S	0	50.5	16.0	1.34	0.14	—	—	2.0752	0.0004
188	10h30m38.36s	+08d53m24.7	-0.47	0.09	0.117	—	1	3.2	8.0	4.17	0.23	—	—	1.74862	0.00026
189	10h31m44.69s	+41d54m24.6	-0.89	0.18	0.242	S	0	42.8	12.0	2.43	0.18	—	—	0.6802	0.0011
190	10h31m44.81s	+60d20m30.3	-0.21	0.04	0.099	F	1	1.7	7.0	4.4	0.21	—	—	1.2299	0.00025
191	10h34m17.49s	+08d36m28.3	-0.68	0.14	1.225	—	0	7.3	15.0	2.42	0.21	—	—	0.0	3e-05
192	10h35m16.57s	+26d15m17.0	-0.83	0.17	0.451	S	0	17.2	7.0	2.24	0.14	—	—	1.6076	0.0008
193	10h36m33.03s	+22d03m12.3	0.17	0.03	0.000	F	0	6.8	7.0	3.23	0.18	—	—	0.0	5e-05
194	10h36m42.00s	+25d02m33.3	-0.95	0.19	2.881	S	2	-4.4	11.0	2.33	0.17	—	—	2.004	0.0004
195	10h39m41.16s	+11d46m17.2	-0.4	0.3	—	—	0	21.4	14.0	8.0	0.6	—	—	1.8793	0.0006
196	10h39m41.97s	+24d22m39.5	-0.141	0.028	0.390	F	0	14.8	13.0	3.31	0.25	—	—	1.17386	0.00017
197	10h41m10.76s	+35d19m15.7	-0.77	0.15	1.152	S	0	40.4	8.0	5.6	0.3	—	—	1.01345	0.00024
198	10h41m47.28s	+52d33m32.6	-0.122	0.024	3.439	F	2	27.4	5.0	2.22	0.14	—	—	0.0	7e-05
199	10h42m44.54s	+12d03m31.8	-0.5	0.1	0.003	—	1	25.5	0.3	6.88	0.23	-1.58	0.24	1.0286	0.00011
200	10h44m10.55s	+35d09m11.0	-0.88	0.18	0.258	S	0	1.0	8.0	4.9	0.26	—	—	2.21475	0.00029
201	10h45m31.76s	+32d58m07.7	-0.5	0.1	1.335	—	0	27.4	9.0	12.7	0.7	—	—	1.43282	0.00027
202	10h45m42.49s	+52d51m11.2	-0.68	0.14	1.365	—	0	25.4	6.0	4.51	0.22	—	—	1.0574	0.0001
203	10h45m45.97s	+41d09m09.3	-0.85	0.17	0.397	S	0	22.4	4.0	5.96	0.23	—	—	1.75296	0.00027
204	10h47m14.83s	+41d30m11.3	-0.5	0.1	3.691	—	0	40.6	19.0	7.6	0.7	—	—	1.3312	0.0005
205	10h47m32.64s	+47d25m32.3	-0.53	0.11	0.008	—	0	1.8	5.0	1.4	0.11	—	—	0.0	9e-05
206	10h49m32.03s	+05d05m31.7	-0.82	0.16	0.034	S	1	16.9	14.0	7.7	0.5	—	—	1.1136	0.0025
207	10h49m41.69s	+37d56m27.9	-0.62	0.12	0.211	—	0	21.6	11.0	5.1	0.3	—	—	1.9807	0.0006
208	10h50m10.06s	+04d32m51.3	-0.0056	0.0011	0.044	F	0	12.1	14.0	6.4	0.5	—	—	1.2158	0.0002
209	10h50m44.59s	+07d18m30.6	-0.5	0.4	—	—	0	20.7	12.0	6.5	0.4	—	—	1.2243	0.0006
210	10h51m29.30s	+23d47m57.9	-1.09	0.22	0.370	S	0	-5.3	3.0	3.82	0.18	—	—	1.27277	0.00011
211	10h51m41.22s	+59d13m05.6	-0.7	0.14	0.283	—	0	-11.2	6.0	4.64	0.22	—	—	0.4354	0.0015
212	10h51m44.89s	+12d58m29.2	-0.119	0.024	0.254	F	0	-1.6	11.0	8.4	0.5	—	—	1.31434	0.00027
213	10h51m48.80s	+21d19m52.8	-0.12	0.05	1.116	F	2	8.8	1.9	2.66	0.13	—	—	1.30098	0.00012
214	10h53m09.53s	+58d55m34.1	-0.7	0.14	0.862	—	0	7.2	11.0	6.3	0.4	—	—	1.1757	0.0006
215	10h54m26.59s	+27d03m18.0	-0.4	0.08	0.755	—	1	-5.4	13.0	5.3	0.4	—	—	1.40064	0.00025
216	10h54m31.80s	+38d55m21.6	-0.16	0.03	3.763	F	1	18.5	14.0	7.5	0.6	—	—	1.366	0.002
217	10h54m49.73s	+25d26m50.9	-0.8	0.16	0.422	S	0	2.7	8.0	7.1	0.4	—	—	0.8133	0.0004
218	10h55m47.63s	+26d23m37.0	-0.9	0.18	0.145	S	0	4.3	8.0	5.6	0.3	—	—	0.8882	0.0013
219	10h55m50.45s	+16d30m41.1	-0.5	0.1	2.073	—	0	-8.4	16.0	2.86	0.25	—	—	0.0	8e-05
220	10h56m12.02s	+05d31m11.9	-0.59	0.12	0.611	—	0	18.1	5.0	6.1	0.25	—	—	1.7287	0.0003
221	10h56m54.48s	+05d17m06.4	-0.5	0.1	0.642	—	0	39.5	10.0	5.9	0.3	—	—	0.0	6e-05
222	10h57m12.80s	+16d22m19.6	-0.37	0.07	2.263	—	0	-23.4	9.0	6.2	0.3	—	—	0.7918	0.00011
223	10h58m13.02s	+49d39m36.2	-0.72	0.14	0.010	S	1	5.9	5.0	5.32	0.22	—	—	2.3916	0.0006
224	10h58m17.46s	+19d52m09.5	—	—	—	—	0	-7.8	1.0	2.57	0.14	—	—	0.0	7e-05
225	10h58m17.86s	+19d51m39.9	—	—	—	—	0	-0.1	2.0	2.13	0.12	—	—	0.0	7e-05
226	10h58m40.86s	+53d35m44.1	-0.64	0.16	—	—	1	12.3	7.0	8.3	0.3	—	—	1.5374	0.0004
227	10h59m51.93s	+40d51m16.9	-0.62	0.12	3.522	—	1	-4.4	19.0	1.23	0.15	—	—	1.74611	0.00015
228	11h00m21.07s	+16d29m14.2	-0.23	0.05	0.022	F	1	-0.4	4.0	5.65	0.22	—	—	0.92	0.0004
229	11h00m47.73s	+10d46m13.1	-0.8	0.16	0.239	S	0	15.6	1.5	7.5	0.28	-0.64	0.13	0.0	4e-05
230	11h02m14.25s	+27d57m09.3	0.42	0.08	0.000	F	1	26.9	8.0	3.51	0.18	—	—	1.86848	0.00029
231	11h03m03.55s	+11d58m16.6	0.038	0.008	2.775	F	0	1.3	6.0	4.18	0.19	—	—	0.9122	0.0003
232	11h04m37.43s	+50d47m51.8	-0.82	0.16	0.537	S	0	28.2	17.0	3.31	0.29	—	—	2.1668	0.0007
233	11h04m53.65s	+60d38m55.7	0.17	0.03	0.239	F	0	-29.3	15.0	2.39	0.22	—	—	1.365	0.0004
234	11h07m15.02s	+16d28m01.5	-0.31	0.06	0.670	—	0	-13.9	4.0	1.96	0.12	-1.24	0.25	0.0	4e-05
235	11h07m15.77s	+05d33m08.4	-0.87	0.17	0.135	S	0	11.6	10.0	1.28	0.12	—	—	0.0	8e-05
236	11h07m18.92s	+10d04m18.7	-0.65	0.13	0.289	—	0	2.5	17.0	2.9	0.26	—	—	0.0	6e-05
237	11h07m57.37s	+66d32m56.2	-0.79	0.16	0.439	S	1	3.3	12.0	2.7	0.2	—	—	0.9566	0.00016
238	11h10m22.70s	+03d21m32.3	—	—	—	—	0	-6.3	8.0	7.5	0.4	—	—	0.966	0.001
239	11h15m47.19s	+43d04m29.0	-0.77	0.17	—	S	0	41.8	17.0	7.9	0.7	—	—	1.0358	0.0004
240	11h17m53.20s	+41d20m17.0	-0.36	0.07	3.529	—	0	22.1	13.0	1.67	0.14	—	—	2.21872	0.00018
241	11h18m11.85s	+53d19m44.7	-0.85	0.17	0.292	S	0	10.3	1.0	8.1	0.3	—	—	1.24145	0.00023
242	11h19m02.68s	+38d58m14.5	-0.71	0.14	3.562	S	0	16.7	11.0	6.6	0.4	—	—	0.7	0.0
243	11h20m04.97s	+46d07m46.5	-0.58	0.12	0.563	—	0	13.0	12.0	9.5	0.6	—	—	1.0035	0.0002

Table B4
Continued from Table B1.

#	NVSS R.A. J2000 (°)	NVSS Dec. J2000 (°)	α	$\Delta\alpha$	χ^2	Flat/Steep Sub-Sample	$N_{\rm MgII}$	RM (rad m^{-2})	ΔRM (rad m^{-2})	Π (%)	$\Delta\Pi$ (%)	β	$\Delta\beta$	z	Δz
244	11h20m23.16s	+54d04m27.5	-0.37	0.07	3.835	—	0	18.7	5.0	3.9	0.18	—	—	0.92216	0.00018
245	11h21m29.82s	+12d36m20.0	-0.77	0.15	0.846	S	0	25.7	9.0	1.84	0.15	—	—	0.6836	0.0013
246	11h23m38.15s	+05d20m39.0	-0.4	0.08	0.702	—	0	4.3	8.0	6.2	0.3	—	—	2.17932	0.00026
247	11h25m53.70s	+26d10m20.1	0.2	0.04	0.017	F	0	-11.4	2.6	2.36	0.13	—	—	2.349	0.00014
248	11h26m28.23s	+39d18m43.0	-0.77	0.15	0.994	S	0	25.9	13.0	2.87	0.23	—	—	1.5	0.0
249	11h26m56.73s	+28d46m13.9	-0.87	0.17	0.985	S	0	-12.7	5.0	4.5	0.2	—	—	1.3978	0.0009
250	11h26m57.66s	+45d16m07.3	-0.0092	0.0018	2.733	F	1	8.3	14.0	1.01	0.12	—	—	1.81384	0.00026
251	11h27m02.46s	+02d31m08.9	-0.42	0.08	0.774	—	1	8.9	4.0	6.59	0.26	—	—	1.65366	0.00022
252	11h27m53.52s	+00d05m19.0	-0.9	0.18	0.286	S	0	3.7	5.0	7.1	0.3	—	—	0.0	9e-05
253	11h29m29.17s	+45d20m25.8	-0.74	0.15	0.780	S	2	43.0	15.0	4.2	0.3	—	—	1.1194	0.0002
254	11h30m36.99s	+10d54m01.0	-0.36	0.07	0.110	—	1	4.3	15.0	3.08	0.26	—	—	1.3223	0.0004
255	11h30m53.27s	+38d15m19.1	0.1	0.1	1.199	F	0	-37.8	13.0	0.72	0.11	-0.07	0.014	1.7404	0.0004
256	11h32m45.65s	+00d34m28.0	-0.25	0.05	0.061	F	0	21.2	4.0	3.0	0.15	—	—	1.223	0.005
257	11h34m54.61s	+30d05m25.2	-0.93	0.19	0.554	S	0	20.5	5.0	1.18	0.11	-0.5	0.1	0.0	2.4e-05
258	11h35m11.71s	+35d14m52.8	-0.85	0.17	0.281	S	0	-1.6	12.0	1.71	0.16	—	—	0.992	0.001
259	11h38m02.34s	+25d24m24.6	-0.19	0.04	0.001	F	0	14.3	9.0	3.4	0.18	—	—	1.6601	0.0003
260	11h40m16.66s	+00d53m51.4	-0.27	0.05	0.698	F	0	-8.4	13.0	3.43	0.26	—	—	1.13641	0.00018
261	11h40m54.55s	+26d43m35.4	-0.93	0.19	0.156	S	1	-17.7	17.0	1.12	0.14	—	—	2.12	0.0013
262	11h41m20.65s	+10d05m24.8	-0.4	0.3	—	—	0	26.1	15.0	6.3	0.5	—	—	1.0499	0.0005
263	11h41m24.07s	+42d17m50.2	-0.82	0.16	0.290	S	0	2.7	12.0	4.28	0.27	—	—	2.0442	0.0009
264	11h42m57.23s	+21d29m12.5	-1.08	0.22	0.321	S	1	19.1	1.2	6.2	0.24	—	—	1.37104	0.00019
265	11h43m12.10s	+46d23m26.7	-0.17	0.03	0.380	F	0	2.3	15.0	2.95	0.25	—	—	1.3214	0.0006
266	11h43m27.47s	+30d05m54.7	-1.07	0.21	0.593	S	0	-5.0	8.0	1.5	0.12	—	—	2.27414	0.00018
267	11h45m33.90s	+38d56m55.5	-0.87	0.17	2.330	S	1	23.8	12.0	2.49	0.19	—	—	2.3	0.0
268	11h46m36.77s	+32d00m03.9	-0.64	0.13	0.282	—	0	-4.8	9.0	5.43	0.28	—	—	1.75746	0.00025
269	11h47m59.74s	+26d35m42.7	0.127	0.025	0.632	F	0	21.0	17.0	1.09	0.13	—	—	0.866	0.0001
270	11h49m30.92s	+25d14m32.7	-0.81	0.16	0.021	S	0	15.1	2.1	5.36	0.19	—	—	0.59535	0.00011
271	11h49m54.43s	+27d11m29.4	-0.5	0.3	—	—	2	-4.1	14.0	7.4	0.5	—	—	1.7421	0.0006
272	11h51m09.27s	+47d28m57.2	-1.14	0.23	3.870	S	1	-22.8	6.0	2.41	0.15	—	—	0.86211	0.00019
273	11h51m29.32s	+38d25m52.6	-0.75	0.06	2.737	S	1	8.4	4.0	4.02	0.17	-0.65	0.16	1.3016	0.00013
274	11h52m01.07s	+10d23m23.1	-0.58	0.12	0.301	—	1	20.9	8.0	3.92	0.21	—	—	2.0844	0.0007
275	11h52m58.75s	+29d30m15.0	-0.29	0.06	0.405	F	0	7.6	16.0	2.96	0.24	—	—	1.2348	0.0004
276	11h53m12.54s	+09d14m02.5	-0.45	0.09	1.090	—	0	52.2	4.0	2.1	0.12	—	—	0.0	4e-05
277	11h55m42.70s	+02d14m11.4	0.0114	0.0023	0.100	F	0	30.7	16.0	3.5	0.3	—	—	0.87288	0.00015
278	11h59m10.35s	+03d02m10.7	-0.5	0.1	0.000	—	2	29.6	9.0	6.8	0.3	—	—	1.00885	0.00022
279	11h59m17.83s	+44d12m17.3	-0.78	0.16	0.048	S	0	-0.3	2.9	6.0	0.22	—	—	1.2107	0.0005
280	11h59m31.80s	+29d14m44.3	-0.24	0.08	2.461	F	0	-31.9	1.4	2.91	0.15	-0.44	0.17	0.7247	0.0001
281	12h00m03.94s	+41d08m45.2	-0.75	0.15	1.528	S	1	8.0	10.0	3.81	0.23	—	—	1.8594	0.0002
282	12h01m15.08s	+18d09m34.4	-0.71	0.14	0.629	S	1	-41.1	8.0	5.6	0.3	—	—	1.09234	0.00025
283	12h03m01.03s	+06d34m41.2	-0.07	0.19	—	F	1	16.7	4.0	4.36	0.18	—	—	2.1778	0.0004
284	12h04m35.61s	+19d10m26.3	-0.0107	0.0021	0.024	F	0	11.5	17.0	3.5	0.3	—	—	1.6558	0.0003
285	12h07m12.62s	+12d11m45.8	0.066	0.013	0.317	F	0	-23.2	8.0	4.06	0.22	—	—	0.89182	0.00022
286	12h07m27.83s	+27d54m59.3	-0.19	0.04	0.075	F	1	15.9	5.0	2.3	0.13	—	—	2.18043	0.00015
287	12h09m13.52s	+43d39m18.7	-1.01	0.03	1.222	S	1	-0.1	0.4	8.2	0.27	-0.4	0.1	1.3991	0.0002
288	12h09m45.11s	+25d47m03.3	-0.104	0.021	0.231	F	2	19.0	6.0	2.77	0.16	—	—	1.43582	0.00024
289	12h10m51.98s	+52d30m51.0	-0.76	0.15	0.587	S	0	28.9	5.0	2.58	0.14	—	—	1.6507	0.0022
290	12h11m18.51s	+42d34m26.0	-0.59	0.12	0.940	—	2	-18.5	2.4	7.98	0.27	—	—	2.0183	0.0006
291	12h12m01.68s	+60d50m25.5	-0.8	0.16	0.060	S	2	20.0	9.0	4.03	0.23	—	—	1.14377	0.00029
292	12h12m05.86s	+20d43m20.5	-0.88	0.18	0.303	S	0	-14.9	2.9	5.55	0.21	—	—	2.3193	0.00016
293	12h12m55.83s	+24d53m32.7	-0.22	0.04	0.274	F	1	14.4	11.0	3.49	0.22	—	—	2.3912	0.0007
294	12h12m56.07s	+19d25m47.4	-0.071	0.014	0.003	F	1	-19.7	5.0	2.23	0.14	—	—	1.24206	0.00015
295	12h13m32.13s	+13d07m20.4	-0.34	0.07	0.372	—	1	-11.6	5.0	1.45	0.11	0.0	0.5	1.13862	0.00027
296	12h14m59.79s	-02d24m58.6	—	—	—	—	0	-8.3	7.0	10.6	0.5	—	—	1.6906	0.0009
297	12h15m03.97s	+16d54m38.1	0.036	0.007	0.255	F	0	-15.5	6.0	3.34	0.17	—	—	1.1	0.0
298	12h15m29.80s	+53d35m54.1	-0.9	0.18	0.099	S	0	30.7	1.2	2.33	0.13	—	—	1.0692	0.0017
299	12h15m41.27s	+05d19m36.0	-0.69	0.14	0.049	—	0	10.9	9.0	4.18	0.24	—	—	0.0	8e-05
300	12h15m48.96s	+31d51m34.6	-0.17	0.03	0.821	F	0	-0.6	6.0	4.13	0.19	—	—	2.2559	0.0004
301	12h16m04.76s	+58d43m33.3	-0.75	0.15	0.010	S	2	37.0	7.0	2.22	0.13	—	—	1.45172	0.00025
302	12h16m19.86s	+23d34m54.8	-0.83	0.17	0.240	S	0	-4.1	7.0	3.62	0.19	—	—	1.3191	0.0003
303	12h17m01.41s	+10d19m49.6	-0.8	0.2	—	S	1	15.5	18.0	3.07	0.29	—	—	1.8833	0.0024
304	12h17m10.92s	+58d35m26.2	-0.25	0.05	1.599	F	0	11.3	4.0	3.18	0.15	—	—	2.54964	0.00017
305	12h17m15.30s	+47d12m14.5	-0.85	0.17	1.179	S	0	-7.7	18.0	4.8	0.4	—	—	1.13332	0.00028
306	12h17m41.40s	+64d07m08.7	-0.73	0.15	0.078	S	0	6.6	6.0	1.33	0.11	—	—	1.3	0.0
307	12h17m56.90s	+25d29m27.2	-0.93	0.19	0.268	S	0	4.0	5.0	1.53	0.12	—	—	0.0	7e-05
308	12h19m43.87s	+67d25m00.4	-0.88	0.18	1.132	S	1	83.2	12.0	4.8	0.3	—	—	1.55959	0.00025
309	12h20m28.08s	+09d28m26.9	-1.11	0.22	0.025	S	1	-11.8	2.3	3.26	0.16	—	—	1.0822	0.0014
310	12h20m39.33s	+17d18m21.4	-0.56	0.11	0.267	—	0	1.5	11.0	5.8	0.4	—	—	0.0	6e-05
311	12h21m06.05s	+45d48m45.5	-0.55	0.11	0.563	—	1	2.3	12.0	4.4	0.3	—	—	0.0	7e-05
312	12h21m27.03s	+44d11m29.8	0.024	0.005	3.058	F	1	-16.9	4.0	2.58	0.13	—	—	1.34653	0.00018
313	12h21m52.92s	+31d30m56.7	-1.12	0.22	2.268	S	0	-1.0	1.5	5.94	0.22	—	—	0.0	6e-05
314	12h21m54.10s	+30d51m46.1	-0.63	0.13	0.119	—	0	-8.9	8.0	2.54	0.15	—	—	0.0	8e-05
315	12h23m11.05s	+37d07m03.2	-0.85	0.17	2.851	S	0	-6.7	2.5	6.1	0.23	—	—	0.0	3e-05
316	12h23m15.70s	+16d42m49.1	-0.9	0.4	—	S	0	-15.1	19.0	5.3	0.4	—	—	1.4194	0.0005
317	12h23m39.25s	+46d11m19.7	-0.087	0.017	0.065	F	1	2.4	5.0	2.92	0.15	—	—	1.01158	0.00015
318	12h23m45.99s	+18d21m07.1	-0.88	0.18	0.000	S	1	0.7	2.0	6.43	0.25	-0.54	0.11	1.40154	0.00022
319	12h24m52.44s	+03d30m50.1	-0.098	0.017	0.166	F	0	19.5	4.0	1.37	0.11	-0.03	0.04	0.95626	0.00013
320	12h25m16.82s	+31d45m33.3	-0.81	0.16	1.796	S	0	-36.9	17.0	3.6	0.3	—	—	1.273	0.0007
321	12h26m57.94s	+43d40m58.6	-0.119	0.024	0.033	F	0	8.8	9.0	3.8	0.23	—	—	2.0085	0.0006
322	12h28m00.82s	+07d25m32.3	-0.8	0.16	1.606	S	0	27.9	15.0	1.63	0.16	—	—	0.67289	0.00013
323	12h28m11.77s	+20d23m19.1	-0.85	0.17	0.032	S	0	14.9	1.0	4.58	0.19	-0.1	0.5	0.7	0.0
324	12h28m36.80s	+10d18m41.8	-0.8	0.16	1.563	S	1	2.6	5.0	3.24	0.15	—	—	2.30257	0.00023

Table B5
Continued from Table B1.

#	NVSS R.A. J2000 (°)	NVSS Dec. J2000 (°)	α	$\Delta\alpha$	χ^2	Flat/Steep Sub-Sample	$N_{\rm MgII}$	RM (rad m^{-2})	ΔRM (rad m^{-2})	Π (%)	$\Delta\Pi$ (%)	β	$\Delta\beta$	z	Δz
325	12h30m53.90s	+39d30m15.4	-0.78	0.17	—	S	1	5.4	4.0	7.7	0.3	—	—	2.2	0.0
326	12h32m12.68s	+33d55m41.0	-0.88	0.18	0.410	S	0	-5.2	4.0	6.0	0.26	—	—	2.4808	0.0004
327	12h32m34.35s	+51d41m09.5	-0.24	0.05	0.849	F	0	20.4	12.0	8.3	0.6	—	—	1.938	0.001
328	12h32m56.56s	+57d22m14.0	-0.68	0.14	0.180	—	1	-15.3	11.0	4.34	0.29	—	—	2.1171	0.0003
329	12h33m54.40s	+48d20m52.1	-0.53	0.11	3.825	—	0	-4.1	14.0	8.0	0.6	—	—	1.0	0.0
330	12h34m25.67s	+24d31m44.1	-0.75	0.15	0.075	S	1	-10.2	7.0	1.45	0.12	—	—	1.33867	0.00013
331	12h34m31.69s	+64d55m55.0	-0.44	0.09	3.772	—	1	33.6	14.0	4.5	0.3	—	—	3.0321	0.00014
332	12h34m53.79s	+67d45m50.1	-0.34	0.07	3.811	—	0	74.2	17.0	2.64	0.24	—	—	1.36713	0.00022
333	12h36m03.91s	+24d24m44.7	-0.063	0.013	1.103	F	0	-10.4	10.0	5.8	0.3	—	—	2.9428	0.0005
334	12h36m49.51s	+25d07m34.7	—	—	—	—	0	4.8	7.0	7.3	0.4	—	—	0.0	2.1e-05
335	12h36m53.54s	+25d08m03.8	—	—	—	—	0	21.2	13.0	2.81	0.22	—	—	0.0	2.1e-05
336	12h37m04.05s	+33d14m22.6	-0.076	0.015	0.082	F	0	-18.2	8.0	3.5	0.2	—	—	1.28766	0.00029
337	12h37m04.38s	+66d34m55.6	-0.64	0.13	0.343	—	0	39.9	12.0	2.04	0.16	—	—	0.0	6e-05
338	12h39m32.78s	+04d43m05.3	-0.026	0.005	1.294	F	0	48.0	13.0	1.48	0.14	—	—	1.7606	0.0008
339	12h40m21.23s	+35d02m59.3	-1.0	0.2	0.798	S	0	4.8	13.0	2.33	0.18	—	—	1.1992	0.0013
340	12h40m42.89s	+25d11m15.1	-0.62	0.12	1.375	—	0	-19.7	13.0	5.8	0.4	—	—	0.0	3e-05
341	12h40m44.53s	+33d03m55.0	-0.8	0.16	0.183	S	1	2.2	4.0	7.8	0.3	—	—	0.8114	0.0011
342	12h41m03.21s	+41d30m42.9	-0.35	0.07	0.562	—	0	14.9	17.0	5.3	0.4	—	—	0.86021	0.00028
343	12h43m57.63s	+16d22m52.7	-0.86	0.17	0.150	S	0	-0.9	1.7	1.59	0.12	-0.43	0.11	0.5551	0.0003
344	12h44m08.55s	+21d17m11.2	-0.8	0.3	—	S	0	7.1	11.0	5.3	0.3	—	—	1.8204	0.0011
345	12h44m10.80s	+17d21m04.1	-0.35	0.07	0.165	—	1	-1.0	11.0	1.38	0.13	—	—	1.28223	0.00022
346	12h44m58.90s	+68d21m35.6	-0.81	0.16	0.495	S	0	60.4	11.0	3.48	0.24	—	—	0.92845	0.00017
347	12h45m38.55s	+55d11m34.3	-0.84	0.17	0.642	S	1	15.7	9.0	2.33	0.16	—	—	1.5551	0.0021
348	12h46m18.26s	+32d28m56.8	-0.29	0.06	1.770	F	3	6.8	9.0	6.6	0.3	—	—	1.5614	0.0003
349	12h46m41.81s	+34d52m42.0	-0.91	0.18	0.341	S	0	-16.8	6.0	7.3	0.3	—	—	1.02447	0.00029
350	12h47m16.82s	+12d36m58.1	-0.92	0.18	1.356	S	0	-9.3	10.0	2.03	0.16	—	—	1.3259	0.0004
351	12h47m20.75s	+32d09m00.0	-0.81	0.16	1.161	S	0	4.3	6.0	2.18	0.14	—	—	0.94895	0.00017
352	12h48m06.66s	+18d38m09.8	-0.71	0.14	0.670	S	0	-26.4	12.0	1.53	0.14	—	—	0.72239	0.00011
353	12h48m26.52s	+46d42m05.9	-0.9	0.18	0.015	S	1	-5.2	12.0	3.83	0.27	—	—	1.23364	0.00024
354	12h48m37.38s	+20d22m26.8	0.035	0.007	0.337	F	0	9.3	9.0	4.46	0.26	—	—	0.76802	0.00012
355	12h48m57.24s	+47d03m44.5	-0.66	0.13	0.057	—	0	14.1	6.0	2.6	0.14	—	—	2.044	0.00024
356	12h49m23.00s	+44d44m45.1	-0.92	0.03	1.268	S	0	9.1	1.3	6.16	0.24	-0.25	0.05	0.8	0.0
357	12h49m44.26s	+65d57m53.7	-0.65	0.13	0.666	—	0	33.2	5.0	8.2	0.3	—	—	0.0	3e-05
358	12h50m09.25s	+16d21m21.3	-0.03	0.006	0.170	F	0	-4.3	10.0	2.27	0.16	—	—	0.85004	0.00016
359	12h50m25.31s	+30d16m38.6	-0.94	0.19	0.515	S	0	4.4	4.0	3.9	0.18	—	—	1.1	0.0
360	12h50m55.41s	+58d18m39.9	-0.65	0.13	0.501	—	0	-3.4	11.0	6.5	0.4	—	—	1.2509	0.0008
361	12h51m51.11s	+49d18m53.3	-0.85	0.17	0.008	S	0	-3.1	16.0	2.87	0.24	—	—	1.4616	0.0003
362	12h53m20.52s	+46d33m52.5	-0.82	0.16	0.987	S	1	11.1	14.0	4.6	0.3	—	—	2.5	0.0
363	12h54m24.46s	+40d55m56.4	-0.68	0.14	0.785	—	1	-31.7	14.0	6.2	0.5	—	—	1.01693	0.00024
364	12h54m28.83s	+45d36m04.2	-0.18	0.04	0.259	F	0	0.1	8.0	3.01	0.18	—	—	1.6466	0.0006
365	12h55m04.22s	+48d09m49.6	-0.91	0.18	1.033	S	0	34.9	10.0	2.24	0.17	—	—	1.70258	0.00023
366	12h56m07.49s	+10d08m57.2	-0.68	0.14	3.976	—	0	18.3	4.0	5.74	0.25	—	—	0.0	5e-05
367	12h57m03.35s	+00d24m38.0	-0.79	0.22	—	S	0	-19.4	4.0	6.28	0.26	—	—	1.25994	0.00029
368	12h57m23.83s	+36d44m19.5	-0.86	0.17	0.047	S	0	15.7	4.0	2.25	0.13	—	—	0.0	6e-05
369	12h59m02.33s	+39d00m19.0	-0.91	0.18	0.459	S	1	6.7	4.0	6.83	0.29	—	—	0.9784	0.0002
370	13h00m28.38s	+10d56m33.8	-0.73	0.15	0.016	S	0	-9.5	19.0	5.4	0.4	—	—	0.97186	0.00014
371	13h00m32.87s	+40d09m09.2	-1.13	0.04	2.325	S	0	77.2	10.0	1.74	0.14	-0.97	0.05	1.671	0.002
372	13h00m36.44s	+08d28m00.6	0.31	0.06	0.700	F	1	42.5	15.0	4.2	0.3	—	—	1.0839	0.0004
373	13h02m53.81s	+23d23m19.6	-0.29	0.06	0.554	F	2	38.1	16.0	4.0	0.3	—	—	3.1881	0.0004
374	13h03m47.06s	-02d01m56.3	-0.65	0.18	—	—	0	10.1	7.0	6.26	0.29	—	—	1.9898	0.0003
375	13h07m13.92s	+13d55m19.9	-0.23	0.05	0.069	F	3	31.0	15.0	3.18	0.26	—	—	1.431	0.0004
376	13h07m54.01s	+06d42m15.9	-0.9	0.18	0.094	S	0	17.0	4.0	5.38	0.23	-1.5	0.3	0.6	0.0
377	13h08m56.63s	+27d08m11.2	-0.7	0.14	0.801	—	2	-9.2	5.0	3.94	0.19	—	—	1.53356	0.00011
378	13h09m09.78s	+55d57m38.5	0.36	0.07	0.029	F	1	41.3	8.0	2.41	0.16	—	—	1.63095	0.00022
379	13h10m50.21s	+26d30m01.6	-1.0	0.3	—	S	0	3.2	9.0	9.1	0.5	—	—	1.5386	0.0004
380	13h10m56.69s	+17d59m39.4	-0.82	0.16	0.019	S	0	-5.7	6.0	2.6	0.15	—	—	1.68084	0.00021
381	13h10m59.46s	+32d33m34.9	0.56	0.11	1.478	F	1	-15.6	13.0	1.39	0.14	—	—	1.6391	0.0007
382	13h11m31.67s	+31d15m56.8	-0.69	0.14	0.715	—	0	4.5	16.0	1.76	0.16	—	—	1.8	0.0
383	13h13m19.49s	+15d52m50.3	-0.72	0.14	0.469	S	0	-4.4	10.0	1.95	0.15	—	—	0.0	2.9e-05
384	13h14m58.47s	+56d03m42.6	-0.68	0.14	0.027	—	0	25.4	6.0	2.92	0.15	—	—	1.74992	0.00024
385	13h17m36.52s	+34d25m16.4	-0.42	0.08	0.519	—	0	-13.0	6.0	2.01	0.13	—	—	1.05419	0.00022
386	13h19m09.35s	+20d53m24.4	-1.04	0.21	0.900	S	0	-22.4	10.0	2.22	0.17	—	—	1.2139	0.0004
387	13h21m18.84s	+11d06m49.4	-0.74	0.15	0.498	S	3	5.9	1.3	2.93	0.13	-1.7	0.3	2.17739	0.00029
388	13h21m39.74s	+00d23m56.9	-0.38	0.24	—	—	0	28.8	4.0	10.7	0.4	—	—	1.61945	0.00016
389	13h24m27.45s	+12d30m35.1	-0.8	0.16	0.041	S	0	5.6	8.0	4.72	0.25	—	—	1.1461	0.0008
390	13h25m29.50s	+65d15m13.8	-0.88	0.18	0.524	S	1	40.2	2.7	3.31	0.15	—	—	1.62894	0.00022
391	13h29m03.39s	+25d31m05.5	-0.53	0.11	0.022	—	1	20.8	19.0	8.7	0.8	—	—	0.98739	0.00019
392	13h30m05.07s	+54d14m51.5	-0.57	0.11	0.443	—	0	28.0	12.0	5.6	0.4	—	—	0.83818	0.00014
393	13h31m08.31s	+30d30m32.4	-0.57	0.11	2.844	—	1	8.8	0.1	9.16	0.29	-0.33	0.05	0.84885	0.00011
394	13h31m25.84s	+24d59m54.3	—	—	—	—	0	-1.6	8.0	6.5	0.3	—	—	0.0	7e-05
395	13h31m28.94s	+25d01m18.7	—	—	—	—	0	2.9	13.0	5.0	0.3	—	—	0.0	7e-05
396	13h32m22.42s	+53d28m17.4	-1.0	0.2	2.883	S	0	27.6	10.0	4.69	0.29	—	—	1.2668	0.0015
397	13h33m45.03s	+02d19m12.0	-0.51	0.22	—	—	1	20.1	8.0	4.89	0.27	—	—	1.2	0.0
398	13h33m58.98s	-03d28m45.8	—	—	—	—	0	19.0	12.0	5.0	0.3	—	—	0.0	4e-05
399	13h34m09.53s	-02d50m31.4	—	—	—	—	2	15.9	15.0	9.3	0.7	—	—	1.7061	0.0007
400	13h37m08.90s	+11d40m08.4	-0.7	0.14	0.381	S	1	-8.3	6.0	3.78	0.19	—	—	1.76069	0.00029
401	13h37m49.65s	+55d01m02.8	0.073	0.015	0.200	F	1	26.7	2.0	4.42	0.17	—	—	1.0974	0.0003
402	13h42m08.31s	+27d09m30.4	0.24	0.05	0.143	F	1	-41.4	16.0	3.22	0.29	—	—	1.1895	0.0002
403	13h42m13.13s	+60d21m42.3	-0.99	0.05	0.517	S	0	3.8	6.0	0.7	0.1	-0.89	0.29	0.96313	0.00016
404	13h44m25.11s	+38d41m29.7	-1.0	0.2	0.352	S	0	13.2	7.0	3.5	0.2	—	—	1.5381	0.0019
405	13h45m36.82s	+38d23m13.1	-0.65	0.04	2.328	—	2	16.7	13.0	0.54	0.11	-1.7	0.3	1.8521	0.00027

Table B6
Continued from Table B1.

#	NVSS R.A. J2000 (°)	NVSS Dec. J2000 (°)	α	$\Delta\alpha$	χ^2	Flat/Steep Sub-Sample	$N_{\rm MgII}$	RM (rad m^{-2})	ΔRM (rad m^{-2})	Π (%)	$\Delta\Pi$ (%)	β	$\Delta\beta$	z	Δz
406	13h47m40.96s	+58d12m42.8	-0.85	0.17	0.434	S	1	2.7	6.0	0.96	0.11	—	—	2.04448	0.00022
407	13h47m51.00s	+28d36m24.8	-0.83	0.17	2.853	S	0	-5.2	5.0	5.33	0.24	—	—	0.0	5e-05
408	13h49m34.72s	+53d41m17.2	-0.45	0.09	0.063	—	0	-13.3	7.0	0.8	0.11	—	—	0.97861	0.00015
409	13h50m15.25s	+38d12m06.4	-0.5	0.1	3.802	—	1	-0.5	14.0	2.91	0.23	—	—	1.3927	0.0003
410	13h50m32.38s	+38d59m22.6	-0.5	0.1	0.499	—	0	-9.4	13.0	3.17	0.21	—	—	1.59401	0.00023
411	13h50m52.71s	+30d34m53.6	-0.067	0.013	0.150	F	1	27.7	12.0	1.79	0.14	—	—	0.71195	0.00018
412	13h50m54.16s	+05d21m56.0	-0.8	0.29	—	S	0	8.2	6.0	9.4	0.4	—	—	0.0	2.7e-05
413	13h51m16.10s	+22d11m10.3	-0.92	0.18	0.027	S	1	19.7	13.0	4.2	0.3	—	—	1.5745	0.0004
414	13h51m43.31s	+02d46m20.7	-0.48	0.24	—	—	1	-7.6	7.0	6.1	0.3	—	—	1.2214	0.0004
415	13h53m05.53s	+04d43m37.5	-0.37	0.22	—	—	0	-3.6	8.0	5.6	0.3	—	—	0.0	5e-05
416	13h53m26.21s	+57d25m51.9	-0.66	0.13	1.264	—	0	55.7	18.0	2.68	0.25	—	—	3.47677	0.00019
417	13h53m51.57s	+01d51m54.4	-0.35	0.18	—	—	1	-4.7	3.0	6.05	0.23	0.8	0.4	1.60678	0.00022
418	13h54m05.28s	+31d39m02.6	-0.63	0.13	3.457	—	1	21.4	18.0	1.75	0.18	—	—	1.3213	0.0002
419	13h55m41.08s	+30d24m11.5	-0.075	0.015	2.900	F	0	-7.0	9.0	4.89	0.26	—	—	1.02113	0.00025
420	13h57m04.37s	+19d19m08.1	0.025	0.005	0.090	F	1	28.1	0.6	6.14	0.23	-1.41	0.18	0.0	1.5e-05
421	13h57m06.40s	+25d37m26.1	-1.0	0.2	0.230	S	3	1.4	3.0	5.2	0.2	—	—	2.0102	0.0005
422	13h57m26.47s	+00d15m41.7	-0.33	0.21	—	—	1	-13.3	11.0	2.9	0.2	—	—	0.0	5e-05
423	13h57m40.09s	+37d49m48.0	-0.73	0.15	0.121	S	2	-18.2	10.0	3.44	0.22	—	—	1.561	0.011
424	13h59m27.11s	+01d59m53.5	0.05	0.18	—	F	0	11.4	1.6	5.86	0.23	-0.06	0.27	1.3272	0.0004
425	13h59m39.17s	+50d51m49.3	-1.0	0.2	3.353	S	1	29.8	11.0	5.1	0.4	—	—	1.4504	0.0003
426	14h02m15.29s	+58d17m46.3	-0.5	0.1	0.115	—	1	13.3	4.0	5.69	0.25	—	—	1.2658	0.00025
427	14h04m09.49s	+06d40m09.4	-0.5	0.22	—	—	0	-1.9	16.0	2.76	0.24	—	—	0.90836	0.00016
428	14h04m16.73s	+34d13m16.1	-0.68	0.14	0.064	—	0	-19.1	13.0	7.4	0.6	—	—	0.932	0.002
429	14h06m02.27s	+06d57m16.1	-0.88	0.18	3.563	S	0	4.0	6.0	3.19	0.17	—	—	0.0	6e-05
430	14h06m56.58s	+46d17m13.2	-1.09	0.22	0.083	S	0	-27.1	14.0	2.04	0.18	—	—	1.3142	0.0023
431	14h08m32.29s	+00d31m33.9	—	—	—	—	0	-2.8	16.0	8.8	0.7	—	—	1.6714	0.0006
432	14h09m18.54s	+64d55m20.8	-0.78	0.16	0.126	S	1	45.2	14.0	7.4	0.5	—	—	1.02906	0.00029
433	14h09m28.95s	-01d57m20.3	—	—	—	—	0	-6.5	15.0	5.6	0.4	—	—	0.0	9e-05
434	14h10m28.17s	+46d08m21.2	-0.83	0.17	0.132	S	0	2.2	13.0	2.02	0.16	—	—	1.01781	0.00025
435	14h12m29.50s	+54d55m12.9	-0.91	0.18	1.885	S	0	10.4	12.0	3.38	0.25	—	—	1.52369	0.00022
436	14h14m16.68s	+10d08m23.6	-0.25	0.05	0.061	F	1	-10.5	13.0	4.2	0.29	—	—	1.7867	0.0006
437	14h18m58.81s	+39d46m38.7	-0.66	0.05	1.124	—	0	19.7	14.0	1.78	0.16	0.19	0.04	0.0	2.8e-05
438	14h19m06.88s	+05d55m03.3	-0.41	0.24	—	—	0	-11.4	15.0	4.04	0.29	—	—	2.2841	0.0005
439	14h19m59.25s	+27d06m26.8	0.43	0.09	0.005	F	0	3.5	11.0	4.19	0.25	—	—	0.53814	0.00012
440	14h22m46.08s	+24d42m57.6	-0.65	0.13	0.453	—	1	-35.8	10.0	2.08	0.15	—	—	1.7045	0.0003
441	14h23m30.10s	+11d59m51.3	-0.38	0.12	1.516	—	1	19.0	1.6	3.56	0.15	0.057	0.011	1.61327	0.00013
442	14h24m37.11s	+47d05m56.9	-0.025	0.005	0.780	F	1	-8.5	5.0	5.19	0.21	—	—	1.7199	0.0004
443	14h24m56.93s	+20d00m22.7	-0.97	0.19	0.117	S	0	9.2	1.3	3.04	0.14	0.02	0.22	0.0	8e-05
444	14h25m18.61s	+12d39m27.6	-0.39	0.08	1.123	—	0	17.4	5.0	4.17	0.19	—	—	1.5119	0.0004
445	14h25m50.67s	+24d04m06.7	-0.84	0.17	0.880	S	0	-4.5	2.3	1.97	0.12	-0.78	0.15	0.0	4e-05
446	14h27m46.92s	+00d28m47.4	—	—	—	—	0	25.3	14.0	5.9	0.4	—	—	1.2604	0.0014
447	14h28m43.74s	+29d19m07.2	-0.65	0.13	0.002	—	0	10.4	29.0	2.0	0.2	—	—	1.4291	0.0003
448	14h30m10.88s	+11d49m54.6	-0.79	0.16	0.707	S	0	10.1	14.0	2.2	0.19	—	—	0.971	0.007
449	14h30m27.85s	+25d12m02.0	-0.088	0.018	0.812	F	0	21.7	12.0	2.7	0.2	—	—	1.21818	0.00026
450	14h30m58.75s	+08d23m32.2	-0.91	0.18	0.384	S	0	20.9	9.0	2.43	0.16	—	—	0.0	2.9e-05
451	14h32m44.31s	-00d59m13.8	—	—	—	—	0	10.2	13.0	4.5	0.3	—	—	1.02458	0.00018
452	14h33m04.53s	+31d20m02.7	-0.88	0.18	1.428	S	0	2.5	11.0	4.33	0.27	—	—	1.563	0.0003
453	14h33m33.30s	+48d42m28.7	-1.21	0.25	—	S	1	14.2	17.0	2.37	0.22	—	—	1.35781	0.00025
454	14h35m56.56s	+17d29m32.9	-0.46	0.09	0.076	—	0	11.9	1.4	5.42	0.19	—	—	1.2	0.0
455	14h36m40.98s	+23d21m03.4	-0.042	0.008	0.052	F	0	8.7	1.6	5.57	0.22	—	—	1.5456	0.0005
456	14h37m33.41s	+38d07m45.1	-0.71	0.14	0.948	S	0	0.8	5.0	6.43	0.26	—	—	1.6	0.0
457	14h37m39.33s	+31d19m02.6	-0.33	0.07	2.645	—	0	18.6	9.0	5.3	0.3	—	—	1.35705	0.00017
458	14h37m48.61s	+24d39m07.4	-0.81	0.16	0.175	S	1	1.0	4.0	3.52	0.16	—	—	1.00133	0.00011
459	14h37m56.76s	+01d56m38.3	-0.2	0.28	—	F	0	-36.9	16.0	4.0	0.3	—	—	1.1802	0.0006
460	14h38m01.35s	+17d00m46.2	-0.81	0.16	0.070	S	1	11.0	10.0	3.91	0.23	—	—	1.5	0.0
461	14h38m20.96s	-02d39m52.9	-0.75	0.18	—	S	0	-3.7	6.0	2.81	0.17	—	—	1.5506	0.0014
462	14h39m04.49s	+04d28m29.2	-0.68	0.14	0.977	—	0	-2.8	2.3	4.98	0.21	—	—	1.2	0.0
463	14h41m31.82s	+60d18m51.8	-0.63	0.13	0.205	—	0	34.1	12.0	5.9	0.5	—	—	0.0	4e-05
464	14h42m03.93s	+13d29m17.6	-0.6	0.12	0.029	—	0	1.6	2.7	3.28	0.15	—	—	0.9925	0.0003
465	14h42m07.64s	+42d52m51.0	-0.66	0.13	0.326	—	0	-4.5	9.0	13.0	0.7	—	—	0.9	0.0
466	14h43m17.52s	+31d54m57.0	-0.76	0.17	—	S	1	2.0	10.0	7.1	0.4	—	—	0.9675	0.0004
467	14h43m47.18s	+14d36m06.8	-0.72	0.14	0.159	S	2	-8.9	7.0	2.91	0.16	—	—	1.43103	0.00016
468	14h45m16.48s	+09d58m36.0	-0.7	0.04	1.201	—	0	34.3	3.0	3.29	0.15	-0.0	0.0013	3.5203	0.0007
469	14h45m20.75s	+47d22m26.2	-0.73	0.17	—	S	1	-21.8	17.0	9.4	0.8	—	—	1.323	0.0006
470	14h45m44.74s	+23d02m39.4	-0.88	0.18	0.034	S	1	23.0	11.0	1.6	0.14	—	—	1.14422	0.00026
471	14h45m58.32s	+12d22m28.5	—	—	—	—	1	14.5	6.0	6.6	0.3	—	—	0.0	2.4e-05
472	14h46m02.50s	+12d22m58.9	—	—	—	—	1	11.6	7.0	5.8	0.29	—	—	0.0	2.4e-05
473	14h46m35.32s	+17d21m07.4	-0.085	0.017	0.002	F	0	3.1	6.0	1.56	0.12	—	—	1.0243	0.0004
474	14h46m36.92s	+00d46m53.6	—	—	—	—	0	0.1	18.0	5.8	0.4	—	—	0.7225	0.0003
475	14h46m50.83s	+21d31m50.9	-0.47	0.09	0.005	—	1	7.1	4.0	3.48	0.17	—	—	1.39542	0.00025
476	14h47m16.02s	+19d20m50.1	-0.29	0.06	0.058	F	0	15.4	7.0	8.6	0.3	—	—	1.3112	0.00022
477	14h48m37.54s	+50d14m48.5	-0.77	0.15	0.045	S	0	26.0	2.0	4.2	0.17	—	—	1.0725	0.0002
478	14h50m12.63s	+47d10m47.1	-0.45	0.09	0.718	—	0	-1.5	8.0	8.6	0.4	—	—	0.0	9e-05
479	14h51m38.74s	+08d47m40.6	-0.85	0.17	0.297	S	0	16.4	9.0	1.8	0.13	—	—	1.08058	0.00017
480	14h52m23.38s	+45d22m35.1	-0.54	0.17	—	—	0	-14.4	7.0	2.46	0.15	—	—	0.0	4e-05
481	14h52m29.07s	+45d21m59.7	—	—	—	—	0	12.5	11.0	5.3	0.3	—	—	0.0	4e-05
482	14h53m01.46s	+10d36m18.2	-0.42	0.08	0.154	—	0	57.9	14.0	2.4	0.2	—	—	2.2738	0.0004
483	14h53m44.24s	+10d25m57.9	-0.27	0.05	0.483	F	1	35.9	5.0	3.44	0.17	—	—	1.7687	0.0018
484	14h53m53.85s	+09d34m25.2	-0.5	0.1	0.690	—	0	40.7	4.0	2.46	0.14	-1.8	1.2	0.0	2.2e-05
485	14h59m23.17s	+09d04m07.9	-0.72	0.14	0.006	S	1	-6.1	11.0	1.95	0.14	—	—	1.982	0.0004
486	14h59m27.09s	+32d53m58.7	-0.91	0.18	0.428	S	0	28.1	9.0	4.7	0.27	—	—	3.33086	0.00023

Table B7
Continued from Table B1.

#	NVSS R.A. J2000 (°)	NVSS Dec. J2000 (°)	α	$\Delta\alpha$	χ^2	Flat/Steep Sub-Sample	$N_{\rm MgII}$	RM (rad m^{-2})	ΔRM (rad m^{-2})	Π (%)	$\Delta\Pi$ (%)	β	$\Delta\beta$	z	Δz
487	14h59m45.21s	+33d01m04.5	-0.77	0.15	0.048	S	0	12.3	9.0	4.84	0.27	—	—	1.0	1.0
488	15h00m07.18s	+56d36m03.1	-0.92	0.18	0.379	S	0	-2.0	4.0	5.72	0.22	—	—	0.8849	0.0003
489	15h00m27.08s	+45d09m02.7	-0.92	0.18	0.806	S	0	-20.4	7.0	6.0	0.3	—	—	1.2039	0.0004
490	15h01m24.56s	+56d19m49.4	-0.47	0.09	1.229	—	2	-5.2	5.0	5.56	0.25	—	—	1.466	0.0003
491	15h04m25.03s	+10d29m38.5	0.22	0.04	0.001	F	0	0.7	1.5	3.58	0.15	0.43	0.14	1.8394	0.0006
492	15h04m26.71s	+28d54m30.6	-0.63	0.13	0.083	—	1	-1.9	4.0	2.72	0.14	—	—	2.28243	0.00013
493	15h04m31.13s	+47d41m49.4	-0.87	0.17	0.185	S	1	0.2	5.0	5.02	0.24	—	—	0.8238	0.0008
494	15h05m06.46s	+03d26m30.4	0.68	0.14	1.115	F	0	25.9	8.0	2.24	0.15	—	—	0.0	9e-05
495	15h07m47.06s	+24d34m30.4	-0.94	0.19	0.187	S	0	-13.6	5.0	2.92	0.15	—	—	2.40488	0.00016
496	15h07m57.34s	+62d13m34.7	-0.77	0.15	0.024	S	1	-20.0	8.0	1.39	0.12	—	—	1.4711	0.0007
497	15h08m38.52s	+34d47m47.0	-0.97	0.19	2.036	S	1	22.0	14.0	7.2	0.5	—	—	1.6404	0.0007
498	15h09m38.93s	+26d42m59.3	-0.36	0.07	0.159	—	0	5.9	11.0	5.1	0.3	—	—	1.03476	0.00025
499	15h10m05.55s	+59d58m55.8	-0.7	0.14	0.274	S	1	-16.8	2.0	9.0	0.3	—	—	1.72461	0.00027
500	15h10m38.66s	+16d40m09.3	-0.61	0.12	0.039	—	1	-10.8	9.0	3.8	0.22	—	—	1.8254	0.0004
501	15h11m29.58s	+49d16m37.7	-0.78	0.16	0.134	S	0	27.8	13.0	4.3	0.3	—	—	2.3965	0.0004
502	15h11m42.92s	+44d30m45.2	-0.95	0.19	0.173	S	0	7.3	8.0	1.57	0.13	—	—	0.96401	0.00013
503	15h12m12.07s	+15d40m25.5	-0.65	0.13	0.066	—	0	-14.4	2.3	2.83	0.14	—	—	0.0	6e-05
504	15h13m56.03s	+04d20m56.2	-0.79	0.16	0.680	S	0	14.9	12.0	1.28	0.13	—	—	0.7195	0.0009
505	15h14m16.79s	+58d57m47.9	-0.75	0.15	0.199	S	0	-39.4	17.0	6.9	0.6	—	—	0.9841	0.0002
506	15h14m34.70s	+02d52m49.3	0.1	0.02	1.054	F	0	8.0	7.0	6.6	0.3	—	—	0.0	9e-05
507	15h19m32.71s	+38d44m54.8	-0.5	0.1	0.662	—	2	-7.6	14.0	4.4	0.4	—	—	1.5219	0.0004
508	15h20m07.41s	+06d25m15.1	-1.07	0.21	0.149	S	0	25.3	16.0	2.23	0.21	—	—	1.1276	0.0003
509	15h21m16.57s	+16d54m02.8	0.025	0.005	0.112	F	0	56.9	16.0	2.1	0.2	—	—	1.38081	0.00024
510	15h25m23.55s	+42d01m17.0	-0.3	0.06	3.455	F	2	23.4	11.0	3.69	0.25	—	—	1.19502	0.00015
511	15h26m41.85s	+16d32m45.6	-0.17	0.03	0.751	F	0	2.6	12.0	5.2	0.3	—	—	0.0	8e-05
512	15h26m46.32s	+09d59m08.8	-0.31	0.06	0.291	—	0	17.9	2.6	4.25	0.17	—	—	1.35921	0.00014
513	15h27m18.75s	+31d15m24.3	-0.41	0.08	1.156	—	0	-1.8	7.0	1.03	0.11	—	—	1.3919	0.0005
514	15h28m37.89s	+56d55m36.3	-0.91	0.18	1.089	S	0	-0.1	11.0	3.76	0.24	—	—	0.89375	0.00029
515	15h29m49.73s	+39d45m09.1	-0.65	0.13	1.797	—	1	-1.6	4.0	9.3	0.4	—	—	1.079	0.0003
516	15h31m27.97s	+03d37m59.3	-0.77	0.27	—	S	0	2.8	9.0	8.9	0.5	—	—	0.7529	0.00017
517	15h33m03.55s	+26d08m29.8	-0.71	0.14	0.632	S	0	16.8	5.0	8.9	0.4	—	—	0.76283	0.00014
518	15h34m52.45s	+01d31m03.3	-0.24	0.08	3.037	F	0	105.6	6.0	0.9	0.11	—	—	1.4276	0.0004
519	15h39m05.14s	+05d34m38.2	-0.109	0.022	1.821	F	0	10.0	7.0	6.9	0.3	—	—	1.5086	0.0003
520	15h39m10.54s	+32d56m50.4	-0.67	0.13	2.662	—	0	-52.7	18.0	2.0	0.2	—	—	0.72429	0.00014
521	15h41m11.72s	+00d50m26.2	—	—	—	—	0	19.2	3.0	6.62	0.27	—	—	1.1374	0.0006
522	15h41m14.69s	+00d50m43.2	—	—	—	—	0	14.7	1.2	10.9	0.3	—	—	1.1374	0.0006
523	15h42m19.54s	+17d56m08.2	-0.65	0.13	0.395	—	2	61.5	10.0	1.99	0.14	—	—	1.66376	0.00027
524	15h43m01.87s	+44d42m50.2	-0.86	0.17	0.214	S	5	36.5	9.0	5.8	0.3	—	—	2.4	0.0
525	15h44m44.97s	+37d13m09.4	-1.0	0.2	1.824	S	0	-11.3	5.0	1.98	0.12	—	—	0.97386	0.00027
526	15h44m59.47s	+04d07m46.7	-0.59	0.12	0.213	—	1	22.1	4.0	2.35	0.14	—	—	2.18326	0.00022
527	15h45m02.81s	+51d35m00.7	-0.09	0.018	0.476	F	0	80.2	8.0	1.35	0.12	—	—	1.92994	0.00027
528	15h45m34.35s	+20d06m41.1	-0.25	0.05	0.436	F	3	31.5	15.0	3.63	0.28	—	—	2.1325	0.0004
529	15h50m35.26s	+05d27m10.6	0.24	0.05	1.070	F	0	19.5	4.0	1.15	0.11	-0.27	0.14	1.4204	0.0004
530	15h50m43.51s	+11d20m58.5	—	—	—	—	0	-42.6	14.0	0.89	0.12	—	—	0.0	2e-05
531	15h50m45.03s	+11d20m33.8	—	—	—	—	0	-7.3	12.0	1.8	0.15	—	—	0.0	2e-05
532	15h53m18.09s	+06d32m15.2	—	—	—	—	0	3.7	10.0	10.3	0.6	—	—	2.0754	0.0007
533	15h53m32.77s	+12d56m50.8	-0.2	0.04	0.000	F	0	-10.9	4.0	1.68	0.12	—	—	1.30867	0.00028
534	15h55m38.91s	+11d06m44.2	-0.094	0.019	0.021	F	1	29.9	10.0	5.0	0.3	—	—	2.6625	0.00016
535	15h57m29.75s	+33d04m45.7	-0.53	0.11	0.106	—	0	0.6	12.0	4.0	0.3	—	—	0.94288	0.00025
536	16h00m16.98s	+18d38m29.9	-0.21	0.04	0.282	F	1	18.3	11.0	3.42	0.24	—	—	2.3965	0.00015
537	16h00m31.56s	+25d45m19.3	—	—	—	—	1	7.9	14.0	7.2	0.5	—	—	1.2767	0.0008
538	16h01m54.49s	+13d57m11.2	-0.53	0.11	0.897	—	3	70.4	5.0	1.84	0.12	—	—	2.23655	0.00021
539	16h02m12.60s	+24d10m10.3	-0.94	0.19	3.217	S	2	26.4	11.0	1.42	0.13	—	—	2.52443	0.00017
540	16h02m27.23s	+27d41m28.2	-0.89	0.18	0.120	S	0	27.3	8.0	5.18	0.26	—	—	0.93639	0.00021
541	16h03m14.57s	+02d31m32.1	-0.076	0.015	0.067	F	0	-8.2	8.0	3.98	0.22	—	—	1.3102	0.0005
542	16h04m55.85s	-00d19m07.4	-0.85	0.18	—	S	1	21.9	7.0	1.17	0.11	—	—	1.63107	0.00024
543	16h06m27.60s	+31d26m07.4	-0.95	0.19	—	S	0	18.3	15.0	1.64	0.16	—	—	1.9379	0.0006
544	16h08m14.48s	+49d19m27.5	-0.75	0.15	0.043	S	0	12.6	11.0	4.32	0.29	—	—	1.32751	0.00028
545	16h08m43.37s	+03d29m51.8	-0.57	0.11	1.970	—	1	10.1	6.0	6.7	0.3	—	—	1.2893	0.0002
546	16h11m08.04s	+18d59m40.3	-0.74	0.15	0.124	S	0	47.4	4.0	4.02	0.17	—	—	1.5285	0.0009
547	16h13m42.83s	+39d07m32.5	-1.0	0.2	3.654	S	1	-0.5	4.0	4.87	0.21	—	—	0.9757	0.0021
548	16h13m46.30s	+20d15m51.7	-0.97	0.19	0.000	S	1	51.8	12.0	2.03	0.16	—	—	1.0663	0.0005
549	16h13m51.22s	+37d42m58.1	-1.0	0.2	0.142	S	0	-16.4	15.0	1.37	0.15	—	—	0.0	9e-05
550	16h13m52.96s	+17d48m04.7	-0.43	0.09	0.120	—	0	43.5	8.0	7.9	0.3	—	—	2.0861	0.0005
551	16h16m55.57s	+36d21m34.4	-0.1	0.02	0.132	F	1	14.0	10.0	2.0	0.15	—	—	2.2618	0.00016
552	16h18m36.30s	+00d10m26.9	—	—	—	—	0	2.5	11.0	7.5	0.4	—	—	1.9877	0.0003
553	16h19m03.62s	+06d13m02.3	0.059	0.012	0.287	F	1	35.4	6.0	1.7	0.12	-0.5	0.6	2.0945	0.0004
554	16h20m21.40s	+17d36m29.3	-1.06	0.21	1.912	S	0	47.8	1.3	5.8	0.21	-1.25	0.28	0.0	5e-05
555	16h22m15.93s	+30d01m47.2	-0.78	0.16	0.018	S	0	28.3	5.0	4.0	0.18	—	—	1.3205	0.0006
556	16h22m32.53s	+14d16m53.7	-0.78	0.16	0.121	S	0	33.2	8.0	2.31	0.15	—	—	0.77906	0.00012
557	16h23m30.52s	+35d59m33.1	-0.47	0.09	0.041	—	0	1.7	5.0	4.4	0.2	—	—	0.8663	0.0001
558	16h24m21.95s	+39d24m42.9	-0.57	0.11	0.250	—	1	-5.9	10.0	2.62	0.19	—	—	1.11738	0.00022
559	16h24m39.42s	+23d45m17.5	-0.89	0.18	0.211	S	3	33.0	1.6	1.65	0.12	-0.35	0.08	0.9	0.0
560	16h25m13.75s	+40d58m51.2	-0.95	0.19	0.015	S	0	53.0	13.0	2.5	0.2	—	—	1.2	0.0
561	16h25m14.23s	+26d50m28.2	-0.91	0.18	1.794	S	0	21.9	4.0	2.46	0.14	0.3	0.6	0.7802	0.00013
562	16h25m30.87s	+27d05m44.6	-0.7	0.14	0.885	—	0	-3.0	10.0	1.09	0.12	—	—	0.0	5e-05
563	16h27m18.14s	+49d55m12.7	-0.56	0.11	0.112	—	0	32.3	5.0	5.35	0.22	—	—	0.90352	0.00015
564	16h27m33.40s	+26d06m02.3	-0.76	0.15	0.184	S	1	53.8	6.0	4.6	0.2	—	—	1.65673	0.00023
565	16h28m05.16s	+25d26m36.7	-0.37	0.07	3.134	—	0	34.0	9.0	6.2	0.3	—	—	0.9949	0.0003
566	16h30m39.37s	+63d01m44.9	-1.03	0.21	0.207	S	1	0.2	17.0	4.1	0.4	—	—	2.3753	0.0003
567	16h30m46.30s	+36d13m10.0	-1.07	0.21	2.896	S	0	-65.0	15.0	1.17	0.13	-2.9	3.0	1.25774	0.00012

Table B8
Continued from Table B1.

#	NVSS R.A. J2000 (°)	NVSS Dec. J2000 (°)	α	$\Delta\alpha$	χ^2	Flat/Steep Sub-Sample	$N_{\rm MgII}$	RM (rad m^{-2})	ΔRM (rad m^{-2})	Π (%)	$\Delta\Pi$ (%)	β	$\Delta\beta$	z	Δz
568	16h31m45.29s	+11d56m03.3	-0.5	0.1	0.715	—	1	39.9	2.0	2.37	0.12	-0.3	1.1	1.7875	0.0003
569	16h36m16.64s	+17d35m08.3	-0.76	0.15	0.003	S	1	65.5	6.0	4.77	0.21	—	—	1.9081	0.0004
570	16h36m38.21s	+21d12m55.5	0.041	0.008	0.143	F	2	54.0	13.0	1.15	0.13	—	—	1.80168	0.00029
571	16h39m49.80s	+24d43m34.5	-0.92	0.18	1.028	S	3	61.4	14.0	2.55	0.21	—	—	1.5866	0.00026
572	16h39m56.04s	+47d05m24.0	-0.5	0.1	3.809	—	1	27.9	7.0	4.23	0.21	—	—	0.86048	0.00021
573	16h44m51.10s	+37d30m27.4	—	—	—	—	0	23.3	13.0	4.4	0.3	—	—	0.0	6e-05
574	16h44m55.26s	+37d29m44.2	—	—	—	—	0	11.1	14.0	6.1	0.5	—	—	0.0	6e-05
575	16h48m29.29s	+41d04m05.8	-0.29	0.06	3.184	F	0	3.2	13.0	2.11	0.17	—	—	0.8516	0.0001
576	16h50m05.37s	+41d40m32.2	-0.44	0.09	0.048	—	0	25.2	3.0	8.1	0.3	—	—	0.0	5e-05
577	16h55m35.81s	+18d06m21.7	-0.5	0.1	0.065	—	0	20.0	8.0	5.45	0.25	—	—	1.8139	0.0005
578	16h58m01.36s	+34d43m27.6	-0.0113	0.0023	0.353	F	0	89.3	15.0	1.96	0.16	—	—	1.93767	0.00016
579	17h01m23.78s	+38d51m39.8	-0.87	0.17	3.355	S	0	17.4	7.0	5.24	0.27	—	—	1.1125	0.0019
580	17h03m07.94s	+22d11m40.8	-0.89	0.18	0.000	S	0	61.1	7.0	3.5	0.19	—	—	1.2	0.0
581	17h08m46.00s	+24d35m41.2	-0.72	0.14	0.484	S	0	96.0	1.9	9.7	0.3	—	—	1.35676	0.00025
582	17h22m42.01s	+28d14m59.4	-0.079	0.016	0.359	F	1	69.5	11.0	2.59	0.18	—	—	0.95143	0.00016
583	21h30m04.66s	-01d02m41.4	-0.69	0.18	—	—	0	19.5	3.0	6.65	0.26	—	—	0.7042	0.0001
584	21h35m11.50s	-00d52m33.4	—	—	—	—	0	5.2	14.0	2.86	0.23	—	—	1.6642	0.0003
585	21h35m15.00s	-00d52m55.3	—	—	—	—	0	16.2	3.0	10.7	0.4	—	—	1.6642	0.0003
586	21h45m18.87s	+11d15m23.8	0.008	0.0016	0.889	F	0	-17.5	7.0	2.81	0.16	—	—	0.0	5e-05
587	22h08m59.89s	+13d16m01.6	-0.3	0.06	0.348	F	0	12.1	13.0	4.2	0.3	—	—	1.29491	0.00021
588	22h15m09.32s	+13d22m37.6	-0.97	0.19	3.715	S	1	21.8	4.0	4.9	0.2	—	—	1.9012	0.0005
589	22h28m52.62s	-07d53m46.1	-0.08	0.05	—	F	0	-27.7	15.0	2.13	0.19	—	—	0.0	4e-05
590	22h40m13.89s	+22d14m15.9	-1.2	0.3	—	S	0	-44.9	7.0	7.1	0.4	—	—	2.6755	0.0004
591	22h47m25.00s	+13d19m19.0	-0.78	0.16	0.553	S	1	-32.3	4.0	6.27	0.23	—	—	1.30276	0.00026
592	22h59m00.68s	-08d11m04.2	-0.05	0.05	—	F	0	-10.0	10.0	4.5	0.28	—	—	1.3764	0.0024
593	23h00m11.69s	-10d21m43.8	—	—	—	—	0	-29.8	5.0	6.8	0.3	—	—	2.3084	0.0006
594	23h05m32.73s	+13d36m09.9	-0.41	0.08	0.618	—	0	-11.4	7.0	4.54	0.22	—	—	1.242	0.0004
595	23h12m12.07s	-09d19m31.4	-0.97	0.18	—	S	0	-1.4	13.0	5.1	0.3	—	—	0.0	4e-05
596	23h16m07.22s	+01d00m12.7	-0.57	0.29	—	—	0	-45.1	13.0	4.7	0.3	—	—	2.6293	0.0003
597	23h32m25.59s	-09d57m56.4	-0.96	0.19	1.265	S	1	21.6	8.0	0.6	0.1	-0.9	0.17	1.6716	0.0006
598	23h50m18.73s	-00d06m58.4	-0.86	0.18	—	S	0	20.2	17.0	1.86	0.16	—	—	1.3581	0.0004
599	23h57m18.60s	+14d46m07.5	-0.63	0.13	0.086	—	1	-33.0	1.7	3.41	0.15	-1.01	0.14	1.81659	0.00015